# Modelling waves and currents in Potter Cove, King George Island, Antarctica

Von der Fakultät für Mathematik und Naturwissenschaften
der Carl von Ossietzky Universität Oldenburg
zur Erlangung des Grades und Titels eines

Doktors der Naturwissenschaften (Dr. rer. nat.)

angenommene Dissertation

von
Chai Heng Lim
geboren am 28.09.1979 in Malacca (Malaysia)

Oldenburg, den 27.01.2014

Erstgutachter: Prof. Dr. Jörg-Olaf Wolff
Zweitgutachter: Prof. Dr. Emil V. Stanev

Tag der Disputation: 10.01.2014

# Abstract

Wave and hydrodynamic models are established to study the wave dynamics and circulation in Potter Cove (King George Island, South Shetland Islands, Antarctica) and their interactions with the surrounding physical and benthic environments. Wave generation, propagation and transformation from deep ocean over complex bathymetric terrains to coastal waters around Potter Cove were simulated for an austral summer month using the SWAN wave model. Investigations were performed to examine and understand the wave patterns, energy fluxes and dissipations in Potter Cove. A nesting approach was implemented from an oceanic scale to a high resolution coastal scale around the cove.

The propagation and amplification of tides were studied using a multiscale unstructured grid, finite-volume coastal ocean model FVCOM. Tidal harmonic analysis was performed to obtain the estimates for the amplitudes and phases of tidal constituents. Cotidal and corange charts of the major tidal constituents ($M_2$, $S_2$, $K_1$ and $O_1$) were constructed for the Bransfield Strait and Northern Antarctic Peninsula region. A comprehensive set of FVCOM simulations consisting of current circulations with respect to different physical forcings, i.e. tides, winds and waves, through the study area was implemented to investigate the circulation patterns in Potter Cove and to assess the relative importance of the various forcings on the flow patterns in the cove. Bed shear stresses due to waves and currents were also calculated to provide a general insight on the bed sediment erosion characteristics and to identify the potential bed erosion prone regions in Potter Cove. The estimated local residence times based on an Eulerian approach and flushing times based on an arithmetic mean and a remnant function concept provide an idea of the efficiency of the water mass transport and exchange with the external waters.

The results of the wave simulations were compared with buoy observations obtained from the National Data Buoy Center, the WAVEWATCH III model results and GlobWave altimeter data. Sea level data from tide gauges were used for the assessment of the modelled results. The quality of the model results is assessed using two statistical parameters, namely the Willmott's index of agreement $D$ and the bias index. Under various wave conditions, the significant wave heights at the inner cove were found to be about 40-50% smaller than the ones near the mouth of Potter Cove. The wave power in Potter Cove is generally low. This study also gives some results on global ocean applications of SWAN.

The tidal regime is mixed, predominantly semi-diurnal in Potter Cove and the most dominant tidal constituent is $M_2$. In general, tides propagate from the Weddell

Sea, enter the Bransfield Strait and move further southwestward. While tides have minimal influence on the circulation in Potter Cove, wind plays a significant role in the circulation patterns which are highly dependent on the wind speed and direction. The wave contribution to the flow is also important. In general, a cyclonic circulation pattern where the waters enter the cove through the northern sector and exit through the southern sector can be observed. Wave-induced bed shear stress is a potential major driving force for the bed sediment erosion in Potter Cove, especially in shallow water regions. In contrast, the bed shear stress due to currents was found to be less significant. Both the spatial characteristics of the active energy dissipation and total bed shear stress follow the pattern of seafloor topography. Under the combined action of tides and winds, the flushing time in Potter Cove is estimated to be in the range of 3.2 to 5.2 days.

# Zusammenfassung

Wellen- und hydrodynamische Modelle wurden verwendet, um die Wellendynamik und die Strömungsverhältnisse in der Bucht Potter Cove (King George Island, South Shetland Islands, Antarktis) zu untersuchen. Ein besonderes Augenmerk wurde dabei auf die Interaktionen dieser Bucht mit ihrer Umgebung und auf die Einflüsse von Wellen und Strömungen auf die benthische Bodenschicht gerichtet. Weiterhin wurden für einen Monat im Sommer der Südhalbkugel die Prozesse der Wellenerzeugung, ihre Ausbreitung und Transformation unter dem Einfluss der komplexen Bodentopographie aus Bereichen des tiefen Ozeans hinein in die flacheren Küstengewässer nahe der Potter Cove mit Hilfe des Seegangsmodells SWAN simuliert. Die Untersuchungen dienten dem besseren Verständnis der Wellenstrukturen, der Energieflüsse und der Energiedissipation innerhalb der Bucht. Um ein Downscaling von den großräumigen ozeanischen Skalen auf die kleinräumigen aber hochaufgelösten Skalen der Küstengewässer nahe der Potter Cove zu gewährleisten, wurde ein Nestingansatz umgesetzt.

Die Ausbreitung und Verformung von Gezeitenwellen wurde mit Hilfe eines Multiskalenansatzes basierend auf dem unstrukturierten Finite-Volumen-Modell FVCOM (Finite-Volume Coastal Ocean Model) untersucht. Um die Amplituden und Phasen der Gezeitenkonstituenten zu erhalten, wurde eine harmonische Analyse der Gezeiten durchgeführt. Für die Regionen der Bransfield Strait und der nördlichen Antarktischen Halbinsel wurden Diagramme der Phasen- und Amplituden-Isolinien der dominanten Gezeitenkonstituenten ($M_2$, $S_2$, $K_1$ und $O_1$) erstellt. Mit FVCOM wurde eine umfassende Anzahl an Simulationen durchgeführt, um den Einfluss und die relative Bedeutung verschiedener physikalischer Antriebsmechanismen wie z.B. der Gezeiten, der Winde oder des Seeganges auf die Strömungen und Zirkulationsmuster innerhalb der Potter Cove zu untersuchen. Weiterhin wurde die durch Wellen und/oder Strömungen bedingte Bodenschubspannung berechnet, um einen generellen Eindruck der Sedimenterosionsmuster zu erhalten und potentielle Erosionsgebiete innerhalb der Bucht zu identifizieren. Einen ersten Eindruck von der Effizienz des Wasseraustausches zwischen der Bucht und ihrer großräumigen Umgebung vermitteln die mit Hilfe eines Euler-Ansatzes geschätzten lokalen Aufenthaltszeiten und die Austauschzeiten der gesamten Bucht, die einerseits als arithmetischer Mittelwert der lokalen Aufenthaltszeiten und andererseits mit Hilfe des Remnant-Funktions-Ansatzes bestimmt wurden.

Die Ergebnisse des Wellenmodells wurden mit Hilfe von Bojendaten des *National Data Buoy Center*, mit Hilfe von Modellergebnissen des alternativen Seegangmo-

dells WAVEWATCH III und mit Hilfe von Satelliten-Altimeter-Daten des *GlobWave*-Projektes validiert. Das Zirkulationsmodell FVCOM wurde weiterhin mit Hilfe von Pegeldaten validiert. Die Güte der Modellergebnisse wurde bestimmt auf der Grundlage zweier statistischer Parameter: des *Willmott's index of agreement D* und des Bias Indexes. Für verschiedene Wellenbedingungen konnte gezeigt werden, dass die signifikante Wellenhöhe innerhalb der Bucht um 40 bis 50% geringer ist als die in der Mündung der Potter Cove. Im Allgemeinen ist die Wellenenergie innerhalb der Bucht eher gering. Weiterhin präsentiert diese Studie einige Resultate von Anwendungen des Modells SWAN auf globalen ozeanischen Skalen.

Das Gezeitenregime innerhalb der Potter Cove ist gemischt und vorwiegend geprägt durch die halbtägliche $M_2$ Gezeitenkomponente. Generell popagieren die Gezeitenwellen aus dem Weddelmeer über die Bransfield Strait weiter in südwestlicher Richtung. Während Gezeiten nur einen geringen Einfluss auf die Zirkulation in der Potter Cove haben, bedingt der Wind in signifikantem Maße die Zirkulationsmuster in der Bucht, die stark korreliert sind mit der Windrichtung und der Windgeschwindigkeit. Darüber hinaus ist der Beitrag der Wellen auf die Strömungen von Bedeutung. Im Allgemeinen kann eine zyklonische Zirkulation beobachtet werden, bei der Wassermassen auf der Nordseite in die Bucht gelangen und diese im südlichen Bereich wieder verlassen. Besonders in den Flachwasserbereichen der Potter Cove ist die durch Wellen induzierte Bodenschubspannung eine wichtige potentielle Einflussgröße auf die Erosion am Boden liegender Sedimente. Im Gegensatz dazu spielt die durch Strömungen induzierte Bodenschubspannung nur eine untergeordnete Rolle. Sowohl die räumliche Charakteristik der Wellenenergiedissipation als auch die Gesamtbodenschubspannung folgen dem Muster der Bodentopographie. Unter dem gemeinsamen Einfluss von Wind und Gezeiten kann die Austauschzeit der Bucht auf eine Zeitspanne zwischen 3,2 und 5,2 Tagen geschätzt werden.

# Contents

# Chapter 1

# Introduction

Potter Cove has been one of the most popular research locations on King George Island, South Shetland Islands, Antarctica (Fig. 3.1). Because of the expense of Antarctic operations, research in Potter Cove is mainly focused on scientific disciplines such as biology, geochemistry, sedimentology, glaciology and hydrography. In recent years, there has been a growing interest in the wave dynamics and hydrodynamic circulation in Potter Cove and their interactions with the surrounding physical and benthic environments. The recent findings of the occurrence of soft-sedimentary habitat (with a scattered occurrence of different marine benthic organisms) and stony habitat (partly covered by macroalgae) in Potter Cove (Hass et al., 2013) have led to further questions among the Antarctic scientific communities regarding the evolution of the seafloor habitat and the mechanisms that affect the bottom sediment distribution. It is still unclear by which physical mechanisms, either currents, waves or both, that potentially influence the bed sediment movement and habitat distributions.

Understanding the physical wave processes and flow circulations is a prerequisite to predict sediment distribution and morphological evolution. Deep water wave properties and the entire bottom topography determine the characteristics of the nearshore waves and currents. In coastal waters, accurate prediction of nearshore waves and hydrodynamics (tides and currents) can improve coastal planning and management and this can provide substantial benefits to coastal communities and useful information to ocean and coastal scientists.

Wind-generated surface gravity waves are the most dominant type of energy in the oceans and they play a major role in ocean and coastal hydrodynamics. Predicting wave climate has been of interest to ocean and coastal scientists and engineers because of the need to estimate the impacts of waves on the natural environment and anthropogenic structures and to provide wave information for human activities at sea such as navigation, fishing, and other marine operations. The Antarctic Peninsula has experienced a major warming for more than half a century (Turner et al., 2005). General climate change, which in turn affects the wave climate, is placing increasing pressure on existing marine habitats. Based on numerical models, Mori et al. (2010) projected future ocean wave climate in relation to the present wave climate and revealed that the wave heights

## 1. INTRODUCTION

of future climate will increase in the Southern Ocean. Waves, which induce bed shear stress on the seabed, can mobilize bottom sediments and disturb the benthic habitats on the continental shelf (Hemer, 2006). This could bring changes to the physical and benthic environments of Potter Cove. Therefore, the understanding of coastal processes and wave conditions unique to Potter Cove and its vicinity is essential to evaluate the impacts of waves on bed sediment erosion, thus implying possible changes in biomass and energy sources.

Wave studies, either through numerical modelling, satellite altimetry or field observations, have been scarcely explored in the remote geographical areas in high latitude regions such as the South Shetland Islands and the Antarctic Peninsula waters. Albeit such scarcity and limitations, it is still possible to estimate the wave climate with wave models that have been widely used over the past two decades. Spectral wind-generated wave models such as WAVEWATCH III (Tolman, 1997, 1999, 2009), WAM (WAve prediction Model, WAMDI Group (1998)) and SWAN (Simulating WAves Nearshore, Booij et al. (1999)) have been developed and constantly improved with continuous theoretical developments as well as the support from wave buoys observations and wave height measurements from satellite altimetry for model validations. Ever since, wave models became effective tools in operational oceanography and they are providing reliable wave predictions at various scales (Rusu, 2011).

As part of the IMCOAST (http://www.imcoast.org) initiative, the present work aims to study and understand the wave dynamics in Potter Cove. This study assesses the wave transformation around the South Shetland Islands and Northern Antarctic Peninsula waters in general and the wave field in Potter Cove in specific, based on a third-generation spectral wave model, namely SWAN, to provide insights into the spatial distribution patterns of significant wave heights under various sea states for an austral summer month. To the authors' knowledge, the present work is the first attempt to address the wave dynamics in Potter Cove and its surrounding waters based on the wave modelling approach. This thesis also addresses the geographical variations of wave energy fluxes as well as different wave energy dissipation distributions throughout this semi-enclosed embayment.

The SWAN model was chosen in the present study because of its flexibility for the applications in ocean and coastal environments (Ortiz-Royero and Mercado-Irizarry, 2008; Rusu, 2011) and because it features proven extensive physics to account for nearshore physical processes such as refraction, shoaling, depth-induced wave breaking, wave energy dissipation due to bottom friction and triad wave-wave interactions. The model was originally developed to predict waves for coastal waters of finite depths. The evaluation of the SWAN model for applications in oceanic environments has received relatively little attention in the wave modelling literature. The present work also intends to test and confirm the viability of the SWAN model for oceanic applications.

Since field observations of sea level have been rather limited in this part of the world, especially in the open sea and deeper water in Bransfield Strait, the second aim of this study is to perform a hydrodynamic modelling using the high-resolution, multiscale coastal ocean model FV-

COM to study and understand the propagation and amplification of tides in the study area, based on tidal harmonic analysis and the construction of cotidal and corange charts. Tidal dynamics in the study area will also be discussed.

Besides waves, the influence of currents on the cove system can be important. Despite the many scientific research activities carried out in Potter Cove, little attention has been paid to the water dynamics for the entire cove. The hydrodynamics of Potter Cove and its surrounding waters has not been modelled previously. Previous studies typically documented general and simplified flow patterns in the cove (Klöser et al., 1994; Roese and Drabble, 1998; Schloss et al., 1997). Judging from its semi-enclosed environment and complex seafloor topography with steep slopes off the opening of the cove (Fig. 2.3b), it is very probable that Potter Cove exhibits complicated current circulation patterns due to various current systems generated by tides, winds, waves and their mutual interactions. It is still unclear by which physical forcing mechanisms, either tides, winds or waves, that dictate the circulation patterns and water renewal in Potter Cove. Therefore, the third aim in this study is to perform a comprehensive set of simulations consisting of current circulations with respect to various physical forcings, and wave-current interactions through the study area to gain an understanding of the flow patterns in Potter Cove and to describe the relative importance of the tides, winds and waves on the circulation patterns in the cove.

Given the potential impact of waves and currents on the bed sediment movement and benthic environment, the identification and description of the effects of these erosive agents on bed sediment dynamics are important in addressing matters essential to seafloor habitats. Hence, the fourth aim is to investigate the influence of waves and currents on the bed sediment erosion characteristics and to identify the potential bed erosion prone regions in Potter Cove. The analysis of the influence of waves and currents on seabed sediments in terms of wave-induced and current-induced bed shear stress estimates will be described.

From a general ecological point of view, it is important to note that the narrower the opening of a cove, the slower the circulation in the cove and this results in a reduced water exchange, thus a decrease in water quality of the system, and vice versa. Such semi-enclosed water inlets are commonly subject to inputs that could alter the health of the whole ecosystem. The self-purification process of these water basins is influenced by the advection and diffusion processes, water mass transport and exchange with the external waters. Water transport time scales provides a general idea of the efficiency of this self-cleansing capacity. The transport time scales also measure how a water system, such as a cove or a small embayment, acts in response to external inputs of waterborne materials (nutrients, contaminants, debris and suspended particulate matters) within the system. It is essential to understand the exchange and transport process in Potter Cove and this information can then be used by scientists to examine the sustainability of the cove. Therefore, the fifth aim of this study is to estimate the local residence and flushing times for Potter Cove. This thesis also presents the spatial distributions of the local residence time.

# Chapter 2

# Description of the study area



Figure 2.1: Potter Cove (the inner side), 2013. Carlini Scientific Station, formerly known as Jubany Station, together with the Dallmann Laboratory, can be seen sitting on the southern coast of Potter Cove. Photo courtesy of Ulrike Falk, Center for Remote Sensing of Land Surfaces (ZFL), Universität Bonn, Germany.

Potter Cove (62°14'S, 58°41'W) is a coastal inlet (Fig. 2.1) indenting the southwestern end of King George Island between Barton and Potter Peninsulas (Fig. 2.2), in the South Shetland Archipelago, Antarctica (Fig. 3.1). Fig. 2.3a depicts the ocean depths of the Northern Antarctic Peninsula areas that are as deep as 5 km and feature a steep shelf break bottom topography. The bathymetry of Potter Cove and its vicinity is shown in Fig. 2.3b. The small inlet (about 4 km long
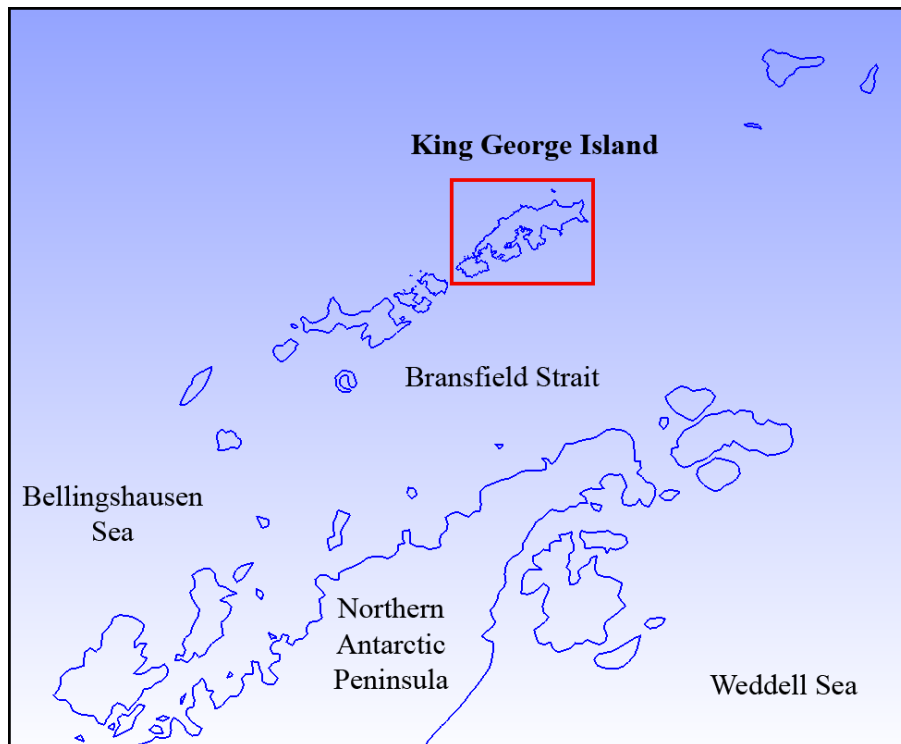
(a) King George Island and the Northern Antarctic Peninsula
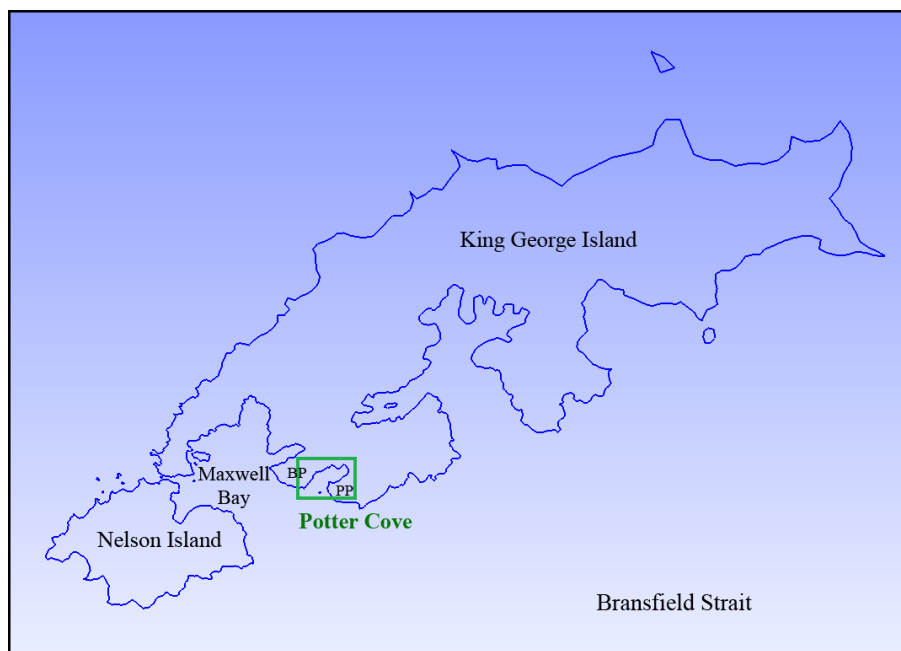


(b) Potter Cove, King George Island

Figure 2.2: Location of the study area. BP: Barton Peninsula; PP: Potter Peninsula.

(a) The Northern Antarctic Peninsula region



(b) Potter Cove, King George Island (KGI)

Figure 2.3: The bathymetry of the study area. Potter Cove is located at the southwestern end of King George Island (KGI). OS: Open Sea; BS: Bransfield Strait; MM: Maxwell Mouth; PM: Potter Mouth; IC: Inner Cove, as indicated by the green squares. The red circles mark the locations of Winship and Mirounga Points.

and 1-2.5 km wide) near the entrance of Maxwell Bay has complex bathymetric features with two sectors where the outer cove has water depths exceeding 100 m and the inner cove comprises depths between 30 and 50 m with a submarine sill of about 30 m at the inner cove.

Off the mouth of Potter Cove, the seafloor topography features steep slopes with an abrupt change in water depth from 50 m down to 400 m or even greater. An outcrop located southwest of Mirounga Point and near the opening of Potter Cove is marked with a white polygon (Fig. 2.3b). Potter Cove connects to the Bransfield Strait via the entrance of Maxwell Bay, which has an average depth of about 470 m. Since it is located in a very remote polar area, the site is free of coastal structures and is surrounded by glaciers that are heavily laden with volcanic material of eolian origin (Griffith and Anderson, 1989). During summer months, glacial meltwater streams discharge sediment-laden water into the cove through several locations from the Barton and Potter Peninsulas (Eraso and Dominguez, 2007; Klöser et al., 1994; Varela, 1998). The cove has a mixed tidal regime with a strong semidiurnal predominance (Roese and Drabble, 1998). The most frequent wind speeds were between 8 and 12 m/s (Schloss and Ferreyra, 2002) and the average wind speeds were generally 10 m/s (Klöser et al., 1994; Schloss et al., 2002). Wave conditions are affected by the winds and complex bathymetry.

According to Schloss et al. (2012), during the past two decades, the air temperature averages have increased. Observations from January 1991 till December 2009 at Jubany Station (presently known as Carlini Station) recorded a temperature increase of 0.39 °C per decade (in summer) and 0.48 °C per decade (in winter). The cove experiences average sea surface temperatures around 1 °C during summer months and a significant increase in sea surface and deep water temperatures has been observed for the summer months in the past two decades. An average water temperature increase of 0.32 °C per decade has been reported. They also analyzed daily sea-ice cover from 1989 to 2009 around the southwestern tip of King George Island and the results showed that the sea-ice cover during summer was typically below 15%. The present study assumed that the ocean and coastal waters are free from sea-ice during summer.

# Chapter 3

# Wave modelling

## 3.1 Model descriptions (SWAN)

The two-dimensional numerical wave model SWAN (Booij et al., 1999), version 40.85 has been implemented to simulate wind-generated waves in Potter Cove and its surrounding waters by transforming deep water waves approaching the shore. SWAN is a third-generation spectral wave model that accounts for physical processes such as wave generation by wind, wave propagation, nonlinear quadruplet-wave and triad-wave interactions, shoaling, refraction, diffraction, reflection and wave energy dissipation. The formulations adapted deep water physics and nearshore processes for shallow water and the wave kinematics are based on the linear wave theory of surface gravity waves.

The wave variance spectrum or energy density $E(\sigma, \theta)$ distributes wave energy over radian frequencies $\sigma$ and propagation directions $\theta$. The spectrum considered in SWAN is the action density spectrum $N(\sigma, \theta)$, which is defined as $E(\sigma, \theta)/\sigma$. The evolution of the wave action density $N$ in SWAN is governed by the action balance equation (Holthuijsen, 2007), which can be formulated in spherical coordinates as follows for the applications at shelf sea or oceanic scales:

$$\frac{\partial N}{\partial t} + \frac{\partial c_\lambda N}{\partial \lambda} + \frac{\partial c_\varphi N}{\partial \varphi} + \frac{\partial c_\sigma N}{\partial \sigma} + \frac{\partial c_\theta N}{\partial \theta} = \frac{S_{tot}}{\sigma} \tag{3.1}$$

where $\lambda$ and $\varphi$ are longitude and latitude; $t$ is the time; $c_\lambda$, $c_\varphi$, $c_\sigma$ and $c_\theta$ are the wave propagation velocities in spatial and spectral spaces $(\lambda, \varphi, \sigma, \theta)$. The first term on the left-hand side in Eq. 3.1 represents the rate of change of wave action density in time. The second and third terms represent propagation of wave action in geographical space. The fourth term represents the effects of relative frequency shifting due to variations in depth and currents. The fifth term represents propagation in directional space due to depth-induced and current-induced refraction. The $S_{tot}$ term on the right-hand side contains the total sources and sinks of wave energy density and is given as

$$S_{tot} = S_{in} + S_{nl3} + S_{nl4} + S_{ds,w} + S_{ds,b} + S_{ds,br} \tag{3.2}$$

These terms represent all physical processes of wave growth by wind ($S_{in}$), nonlinear transfer of wave energy through triad interactions ($S_{nl3}$) and quadruplet interactions ($S_{nl4}$), wave dissipation due to whitecapping ($S_{ds,w}$), bottom friction ($S_{ds,b}$) and depth-induced wave breaking ($S_{ds,br}$). Governing equations for wind source terms and wave energy dissipation are given under Sections 3.1.1 and 3.1.2, respectively.

The relative importance of these processes varies with regions. In relatively shallow waters, shoaling, refraction, wave-bottom interactions, depth-induced wave breaking and triad-wave interactions are dominant. Formulations of physical processes and their associated coefficients adopted in the model for the present study are summarized in Table 3.1. Complete expressions for these physical processes are given in the SWAN scientific and technical manual (SWAN Team, 2011a). More theoretical background related to SWAN as well as waves in oceanic and coastal waters are given by Holthuijsen (2007).

Table 3.1: Formulations of physical processes and their associated coefficients used for the SWAN simulations

| Physical process | Formulation | Coefficients |
|---|---|---|
| Wave growth | Komen et al. (1984) | |
| Whitecapping | WAMDI Group (1998) | $[cds2] = 1.5 \times 10^{-5}$ |
| | | $\tilde{s}_{PM} = \sqrt{3.02 \times 10^{-3}}$ |
| | | $\delta = 0$ |
| | | $p = 4$ |
| Bottom friction | Hasselmann et al. (1973) | $C_b = 0.067 \text{ m}^2\text{s}^{-3}$ |
| Depth-induced wave breaking | Battjes and Janssen (1978) | $\alpha = 1$ |
| | | $\gamma = 0.73$ |

Note: GEN3 KOMen were used with $[cds2] = 1.5 \times 10^{-5}$. QUADrupl, BREaking, FRICtion, TRIad, DIFFRACtion and WCAPping were activated, with default coefficient values. PROP BSBT were used. Please refer to the SWAN user manual (SWAN Team, 2011b) for explanations and details.

### 3.1.1   Wind source terms

Wave growth by wind (SWAN Team, 2011a) is described by:

$$S_{in}(\sigma, \theta) = A + BE(\sigma, \theta) \tag{3.3}$$

in which $A$ describes linear growth and $B$ exponential growth. The expression for the linear growth term $A$ is given by Cavaleri and Malanotte-Rizzoli (1981):

$$A = \frac{1.5 \times 10^{-3}}{2\pi g^2} (U_* \max[0, \cos(\theta - \theta_w)])^4 H_f \tag{3.4}$$

where $U_*$ is the friction velocity (Eq. 3.8), $\theta_w$ is the wind direction and $H_f$ is the filter (Eq. 3.5) to eliminate wave growth at frequencies lower than the Pierson-Moskowitz frequency. Eq. 3.6 gives

the peak frequency $\sigma_{PM}^*$ of the fully developed sea state (Pierson and Moskowitz, 1964).

$$H_f = \exp\left\{-(\frac{\sigma}{\sigma_{PM}^*})^{-4}\right\} \tag{3.5}$$

$$\sigma_{PM}^* = \frac{0.13g}{28\,U_*}2\pi \tag{3.6}$$

For the exponential growth, the expression due to Komen et al. (1984) is used in this study (Eq. 3.7). The exponential growth term becomes significant when wave energy is present.

$$B = \max[0, 0.25\frac{\rho_a}{\rho_w}(28\frac{U_*}{c_{ph}}\cos(\theta - \theta_w) - 1)]\sigma \tag{3.7}$$

where $\rho_a$ and $\rho_w$ are the air and water densities, respectively, and $c_{ph}$ is the phase speed of the wave.

While SWAN is driven by the wind speed at 10 m height $U_{10}$, the friction velocity $U_*$ is used for the computations of $A$ and $B$ and is obtained from the following equation:

$$U_*^2 = C_d U_{10}^2 \tag{3.8}$$

in which $C_d$ is the wind drag coefficient after Wu (1982):

$$C_d = \begin{cases} 1.2875 \times 10^{-3}, & \text{for } U_{10} < 7.5 \text{ m/s} \\ (0.8 + 0.065\,U_{10}) \times 10^{-3}, & \text{for } U_{10} \geq 7.5 \text{ m/s} \end{cases} \tag{3.9}$$

### 3.1.2 Wave energy dissipation

The wave energy dissipation is controlled by three different mechanisms, as represented in the last three terms in Eq. 3.2, i.e. whitecapping, bottom friction and depth-induced wave breaking. Wave spectral dissipation due to whitecapping is dominant in the oceanic waters and shelf seas. As the waves propagate towards intermediate and shallow waters, bottom friction becomes important. Eventually, depth-induced wave breaking contributes to a large portion of energy dissipation in the nearshore region.

#### 3.1.2.1 Whitecapping

Whitecapping on the ocean surface is an important phenomenon for ocean wave evolution. In deep water, considerable wave energy is lost through whitecapping and transferred to surface currents and turbulence. Whitecapping is mainly controlled by the wave steepness and the formulation as adapted by the WAMDI Group (1998) reads:

$$S_{ds,w}(\sigma, \theta) = -\Gamma \tilde{\sigma}\frac{k}{\bar{k}}E(\sigma, \theta) \tag{3.10}$$

where $\tilde{\sigma}$, $k$ and $\tilde{k}$ denote the mean frequency, wave number and mean wave number, respectively. $\Gamma$ is a steepness dependent coefficient and is given by:

$$\Gamma = C_{ds}((1-\delta) + \delta \frac{k}{\tilde{k}}) \left( \frac{\tilde{s}}{\tilde{s}_{PM}} \right)^p \tag{3.11}$$

in which the coefficients $C_{ds}$, $\delta$ and $p$ are tunable coefficients, $\tilde{s}$ is the overall wave steepness, $\tilde{s}_{PM} = \sqrt{3.02 \times 10^{-3}}$ is the value of the wave steepness for the Pierson-Moskowitz spectrum. For the wind input of Komen et al. (1984), which is used in the present study, the default values are $C_{ds} = 2.36 \times 10^{-5}$, $\delta = 0$ and $p = 4$. The overall wave steepness $\tilde{s}$ is defined as:

$$\tilde{s} = \tilde{k}\sqrt{E_{tot}} \tag{3.12}$$

where $E_{tot}$ is the total wave energy:

$$E_{tot} = \int_0^{2\pi} \int_0^{\infty} E(\sigma, \theta) \, d\sigma d\theta \tag{3.13}$$

### 3.1.2.2 Bottom friction

Wave-bottom interaction also contributes to the wave evolution. In water of finite depth, wave energy is attenuated by bottom friction, which involves the turbulent boundary layer at the sea bottom. The empirical model of JONSWAP (Hasselmann et al., 1973) for bottom friction is applied in this study and the formulation can be expressed as follows:

$$S_{ds,b} = -C_b \frac{\sigma^2}{g^2 \sinh^2(kh)} E(\sigma, \theta) \tag{3.14}$$

where $g$ is the gravitational acceleration, $h$ is the water depth and $C_b$ is the bottom friction coefficient that generally depends on the bottom orbital motion $U_{rms}$:

$$U_{rms} = \sqrt{\int_0^{2\pi} \int_0^{\infty} \frac{\sigma^2}{\sinh^2(kh)} E(\sigma, \theta) \, d\sigma d\theta} \tag{3.15}$$

A constant friction coefficient, i.e. $C_b = 0.067$ m$^2$s$^{-3}$, by default in the SWAN model, is adopted in this study.

### 3.1.2.3 Depth-induced wave breaking

In very shallow waters (surf zone), energy dissipation due to depth-induced wave breaking becomes dominant and waves begin to break when the ratio of wave height to water depth reaches

its limiting value. In SWAN, the dissipation is computed with:

$$S_{ds,br}(\sigma, \theta) = -D_{tot} \frac{E(\sigma, \theta)}{E_{tot}} \tag{3.16}$$

where $D_{tot}$ is given by:

$$D_{tot} = \frac{1}{4} \alpha Q_b \left( \frac{\tilde{\sigma}}{2\pi} \right) H_{max}^2 \tag{3.17}$$

in which $\alpha = 1$ in SWAN and $H_{max}$ is the maximum individual wave height that can exist at a given depth. $H_{max}$ can be calculated from $H_{max} = \gamma h$, where $\gamma$ is the breaker parameter. In this study, $\gamma = 0.73$ is used. $Q_b$ is the fraction of breaking waves calculated in SWAN with:

$$Q_b = \begin{cases} 0, & \text{for } \beta \leq 0.2 \\ Q_0 - \beta^2 \frac{Q_0 - \exp(Q_0 - 1)/\beta^2}{\beta^2 - \exp(Q_0 - 1)/\beta^2}, & \text{for } 0.2 < \beta < 1 \\ 1, & \text{for } \beta \geq 1 \end{cases} \tag{3.18}$$

where $\beta = H_{rms}/H_{max}$ and $H_{rms}$ is the root-mean-square wave height. In addition, for $\beta \leq 0.5$, $Q_0 = 0$ and for $0.5 < \beta \leq 1$, $Q_0 = (2\beta - 1)^2$.

### 3.1.3 Model configurations, forcing and boundary conditions

#### 3.1.3.1 Model domain and computational grid

Wave model downscaling has been widely used to achieve high-resolution estimates at the place of interest from coarse-resolution models (Breivik et al., 2009; Chen et al., 2010; Gaslikova and Weisse, 2006; Stopa et al., 2013). Such techniques capture features of the large-scale forcing and include the small-scale effects that are not resolved by the driving large-scale data (Gaslikova and Weisse, 2006). A final high-resolution nested model can be used to provide insights into small-scale wave conditions at specific coastal locations. Furthermore, it accounts for shallow water effects. In this study, wave generation, propagation and transformation from deep ocean to coastal waters around Potter Cove during an austral summer month in January 1999 were modelled to cover the full scale of the wave modelling process entirely based on a single wave model. This was carried out using a one-way grid nesting approach where five different SWAN computational domains (Fig. 3.1) with increasing spatial resolution were run consecutively.

A global model (Fig. 3.1a) with a resolution of 1.0° in latitude and 1.25° in longitude was prepared and used to capture the swell energy from the Pacific Ocean, Atlantic Ocean and Indian Ocean that enters the Antarctic Peninsula domain. It is also required so that the modelled results can be validated with the observed data, which cover most part of the Pacific and Atlantic Oceans, from the National Data Buoy Center (NDBC). The global model agrees with the grid size used by WAVEWATCH III (hereafter referred to as the WW3 model) for general qualitative comparisons. In addition, since the model domains are rather on a large scale, spherical coordinates were implemented in this study so that the curvature of the Earth was taken into account. Note that

(a) Global model domain



(b) South America and Antarctic Peninsula



(c) Northern Antarctic Peninsula



(d) South Shetland Islands
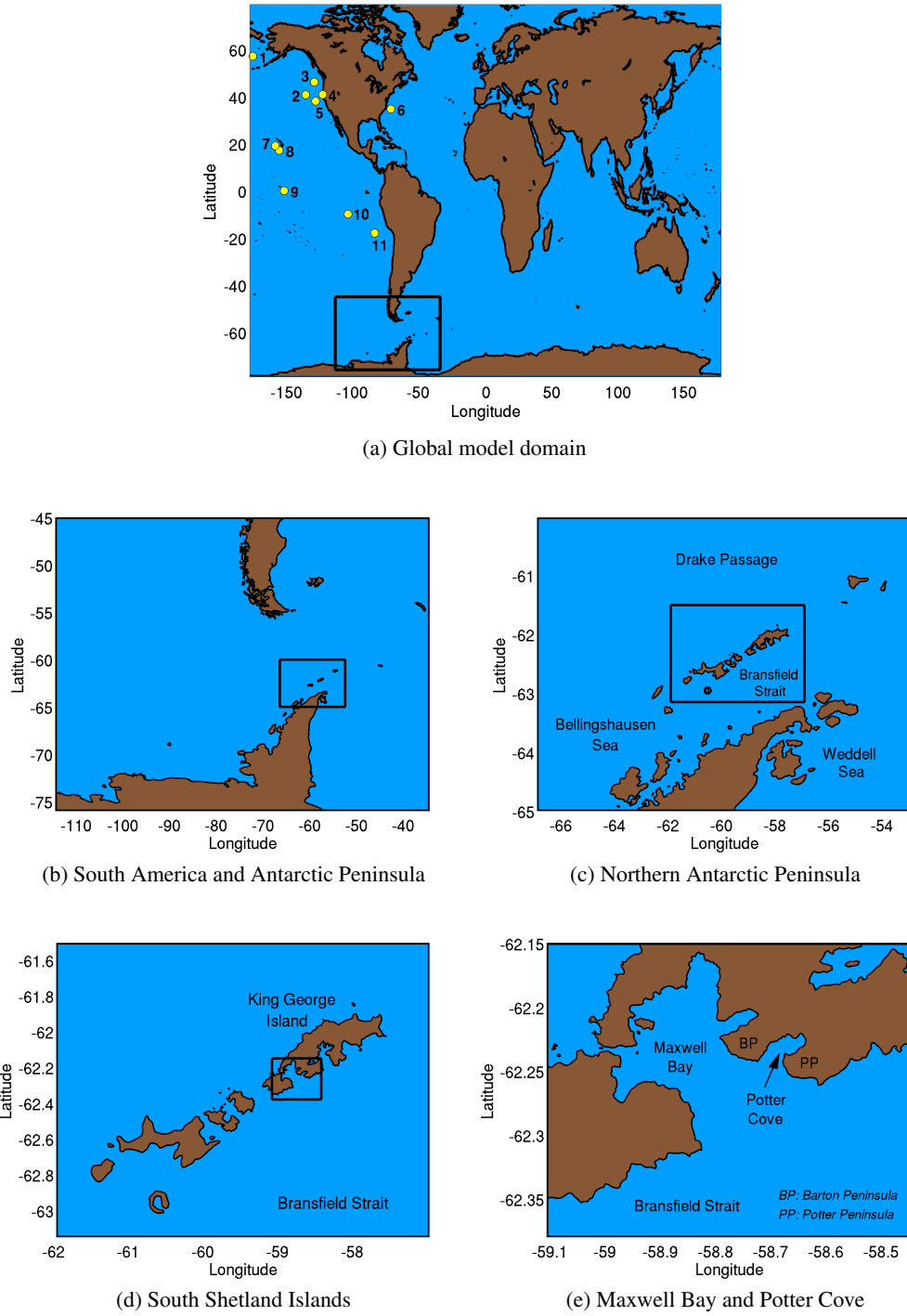


(e) Maxwell Bay and Potter Cove

Figure 3.1: One-way SWAN nesting approach: from global scale down to high resolution domain of interest in Potter Cove. The geographic locations of the NDBC observation stations (Stations 1-11) are marked in yellow circles in (a) Global model domain. The coordinates of each station can be found in Table 3.3.

it is not the aim of this study to quantitatively compare the performance of SWAN and WW3. Nevertheless, for an intercomparison of SWAN and WW3 with observations at oceanic scales, one may consult the work by Ortiz-Royero and Mercado-Irizarry (2008).

Nested into the global model domain is a domain with a 10-km grid resolution that covers South America and the Antarctic Peninsula region (Fig. 3.1b). The subsequent nested domain covers the area of the Northern Antarctic Peninsula (Fig. 3.1c) with a grid spacing of 2 km, followed by a 600-m resolved domain of the South Shetland Islands (Fig. 3.1d). The smallest nested domain covers the waters of Maxwell Bay and Potter Cove (Fig. 3.1e) with a numerical grid resolution of 75 m. Wave frequencies that range from 0.042 up to 0.8 Hz were used. The frequency spectrum was discretized into 30 bins together with 60 bins in direction, giving a spectral directional resolution of $6°$, for a full circle. Table 3.2 summarizes the main details of the computational grids.

Table 3.2: Computational grids for the SWAN simulations

| Grid | Resolution $\Delta x \times \Delta y$ | Time step $\Delta t$ (min) | $n\theta$ or [mdc][1] | $nf$ or [msc][2] |
|---|---|---|---|---|
| Fig. 3.1a - Global model | $1.25°$ lon $\times$ $1.0°$ lat | 30 | 60 | 30 |
| Fig. 3.1b - South America and Antarctic Peninsula | 10000 m $\times$ 10000 m | 15 | 60 | 30 |
| Fig. 3.1c - Northern Antarctic Peninsula | 2000 m $\times$ 2000 m | 10 | 60 | 30 |
| Fig. 3.1d - South Shetland Islands | 600 m $\times$ 600 m | 30 | 60 | 30 |
| Fig. 3.1e - Maxwell Bay and Potter Cove | 75 m $\times$ 75 m | 30 | 60 | 30 |

[1] CIRCLE, i.e. the spectral directions cover the full circle $360°$, was used.
[2] Lowest and highest discrete frequencies, [flow]= 0.042 Hz and [fhigh] = 0.8 Hz.

The implicit numerical schemes in SWAN for wave propagation are not subject to the Courant-Friedrichs-Lewy (CFL) stability criterion, therefore the propagation is unconditionally stable. In other words, the space (both geographical and spectral) and time steps can be chosen on the accuracy basis instead of numerical stability and relatively large time steps are permitted in the computations. In the present study, the time step for the nonstationary computations varies between 10 and 30 min. For the iterative procedure in SWAN computations, a change of less than 2% in signficant wave height and mean wave period between two successive iterations in 98% of the water covered grid points was chosen to terminate the iteration.

The coastline was formed by a combination of data from various sources. In order to have a very fine coastline geometry for the area of interest around the South Shetland Islands, the coastlines around the region were digitized from maps (Antarctic Place-names Committee, 2009a,b, 2010) where coastlines are mainly interpreted from Landsat ETM+ images. The coastlines in other regions were extracted from the Coastline Extractor (http://www.ngdc.noaa.gov/mgg/coast/getcoast.html), provided by the National Oceanic and Atmospheric Administration (NOAA)'s National Geophysical Data Center (NGDC). The World Vector Shoreline (designed for 1:250,000) and the World Coast Line (designed for 1:5,000,000) databases were used to extract the coastline data for the Northern Antarctic Peninsula region and the entire world, respectively.

### 3.1.3.2 Bathymetry

The bathymetry for all the model domains for wave modelling has been interpolated from a combination of various sources which include: (1) the ETOPO1 data set (Amante and Eakins, 2009); (2) the General Bathymetric Chart of the Oceans (GEBCO_08 Grid and GEBCO One Minute Grid, http://www.gebco.net); (3) multibeam bathymetric data gathered during the German expeditions of RV Polarstern (ANT-XXXIII/9) within the region of 59°- 66°S and 68°- 52°W provided by the Bathymetry Group of the Alfred Wegener Institute for Polar and Marine Research (AWI); and (4) high-resolution bathmetric data of Potter Cove provided by the Instituto Antártico Argentino (IAA).

### 3.1.3.3 Wind input

The SWAN model was spun up and driven by 6-hourly zonal and meridional wind speeds of the global National Centers for Environmental Prediction (NCEP)/NCAR Reanalysis products (Kalnay et al., 1996), which is widely used as a driver for wave modelling. The variations of the winds are given at 10 m above sea level $U_{10}$ and the spatial resolution of the wind fields is $\sim 1.9047°$ in latitude and $1.875°$ in longitude. During the computations, SWAN obtained the wind information by interpolating the data in horizontal space to the model grids. NCEP surface wind fields are available for download at http://www.esrl.noaa.gov/psd/data/gridded/reanalysis. Fig. 3.2 depicts the local wind speeds $U_{10}$ in Potter Cove for January 1999 where the wind speeds were interpolated from the NCEP Reanalysis data to a location in Potter Cove at 62° 14'S, 58° 40'W.

Studies have shown that wave-current interactions affect the surface wave growth and decay. Wave height and wave steepness increase in the presence of strong opposing currents (Liu et al., 1989). Nonetheless, the influence of ambient currents on waves is not covered within the framework of the present investigation.
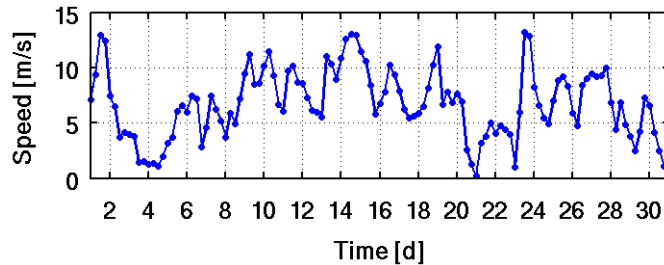


Figure 3.2: Wind speed $U_{10}$ variations in Potter Cove for January 1999. Data were extracted and interpolated from the NCEP Reanalysis data.

### 3.1.3.4   Boundary and initial conditions

For the global model, an option in SWAN called 'REPeating' is activated so that wave energy leaving at one end of the computational domain (in computational *x*-direction) enter at the other side. This is to create a continuous wave field in longitudinal direction around the globe. The global model was forced with NCEP winds with a 10-day spin-up prior to 1-Jan-1999, 00:00:00 UTC in order to allow the sea state to develop and propagate through the computational area before reliable results were obtained. The initial spectra are computed from the wind velocities at the first time step using the deep-water growth curve of Kahma and Calkoen (1992). A two-dimensional spectral output along the boundary of a nested grid was generated and saved during the coarse grid simulation for the subsequent nested run. The boundary conditions in the relevant spectral output file of the previous SWAN run together with the NCEP wind fields were applied at the start time of the nested run. This nesting approach was repeated on decreasing scales using the nested computations. The land boundaries in SWAN do not generate waves and all incoming wave energy is absorbed along the coastlines. For open sea boundaries, SWAN assumes that waves can leave the computational domain freely.

## 3.2   Oceanographic buoy and satellite altimeter data

Up to the time when SWAN simulations were carried out, there were no in situ wave measurements in Potter Cove. Oceanographic observation data in remote polar regions are extremely scarce and measurements from the Southern Pacific, Southern Atlantic and Southern Oceans are very limited. The NOAA's National Data Buoy Center (NDBC) has long-term archive and distribution of oceanographic buoy data around the globe: http://www.ndbc.noaa.gov. Somehow, the in situ buoys are mainly located in the northern hemisphere and around the Equator. For the present study, NDBC data sets from nine stations (Stations 1-9) for January 1999 and two stations (Stations 10-11) for March 1986 were used for model validation. The locations of the NDBC observation stations are shown in Fig. 3.1a and the details of each station are given in Table 3.3.

A recent initiative by the European ESA GlobWave project (http://www.globwave.org) offers a public domain platform for satellite data on ocean waves. Altimeter along-track level 2 preprocessed (L2P) data from the ERS-2 and Topex/Poseidon satellites were obtained from the GlobWave website for the validation of the results from the smaller nested model. In this case, the domain as shown in Fig. 3.1d is covered and the ground tracks of the satellites are shown in Fig. 3.8a. ERS-2 has a repeat cycle of 35 days and Topex/Poseidon followed an orbit with a 10-day period. The quality assessment has been made in GlobWave for each $H_s$ measurement in the L2P data and there is an associated quality variable (*swh_quality*) that is assigned a quality level. In this study, only altimeter records with good quality (*swh_quality* = 0) are used. Data with suspected (*swh_quality* = 1) and bad (*swh_quality* = 2) measurements are excluded from the analysis.

Table 3.3: The coordinates of the NDBC observation stations

| Stations | Latitude | Longitude |
|---|---|---|
| 1. Stn 46035 | 57° 04' 00'' N | 177° 45' 00'' W |
| 2. Stn 46006 | 40° 45' 16'' N | 137° 27' 51'' W |
| 3. Stn 46005 | 46° 05' 59'' N | 131° 00' 05'' W |
| 4. Stn 46022 | 40° 46' 35'' N | 124° 35' 20'' W |
| 5. Stn 46059 | 38° 02' 49'' N | 129° 58' 08'' W |
| 6. Stn 41001 | 34° 40' 30'' N | 072° 41' 54'' W |
| 7. Stn 51003 | 19° 01' 06'' N | 160° 34' 54'' W |
| 8. Stn 51002 | 17° 05' 39'' N | 157° 48' 27'' W |
| 9. Stn 51028 | 00° 00' 01'' N | 153° 54' 46'' W |
| 10. Stn 32301 | 09° 54' 00'' S | 105° 12' 00'' W |
| 11. Stn 32302 | 18° 00' 00'' S | 085° 05' 59'' W |

## 3.3 Statistical assessment of modelled results

The SWAN results were interpolated to each of the buoy's locations so that statistical comparisons between observed and modelled results could be made. Willmott (1981, 1982) suggested that the correlation coefficient $r$, coefficient of determination $r^2$, tests of their statistical significance, and even the root mean squared error (RMSE), which are frequently used in physical oceanography, are inadequate and not the most reliable measures of a model's ability to estimate empirical observations. Alternatively, an index of agreement $D$ has been proposed by Willmott (1981) to reflect the degree to which the observed data $O_n$ is accurately estimated by the predicted values $P_n$, rather than to act as a measure of correlation. The Willmott's index of agreement $D$ is defined as follows:

$$D = 1 - \frac{\sum_{n=1}^{N}(P_n - O_n)^2}{\sum_{n=1}^{N}(\left|P_n - \bar{O}\right| + \left|O_n - \bar{O}\right|)^2} \qquad (3.19)$$

where $N$ is the number of evaluated data and $\bar{O}$ is the mean value of the observed data. The index $D$ varies between 0 and 1.0 where $D = 0$ indicates complete disagreement between $P_n$ and $O_n$ and a value of 1.0 shows perfect agreement. Wornom et al. (2002) examined their wave model results relative to the observations and reported that Willmott's index is more sensitive to the modelling errors than root-mean-square norms of the differences between the predicted and observed values.

The performance of the model was also evaluated using the bias index (Yapo et al., 1996), expressed as follows:

$$\text{bias} = \frac{\sum_{n=1}^{N}(P_n - O_n)}{\sum_{n=1}^{N} O_n} \qquad (3.20)$$

The bias index measures the average tendency of the simulated values to be larger or smaller than their observed data. Bias $= 0$ is the optimal value, with low index values indicating accurate model calculation. Positive values indicate that the solution over predicts the observed data, whereas negative values indicate a tendency of underestimation. For instant, a bias of 0.05 indicates that on average the simulated solution over predicts the observed data by 5%.

### 3.3.1 Goodness-of-fit and error index

The modelled significant wave height $H_s$ (Eq. 3.21), using the default coefficient $C_{ds} = 2.36 \times 10^{-5}$ for whitecapping dissipation, are compared with the NDBC buoy observations. Fig. 3.3 shows an example of the comparisons of time series between observed and modelled $H_s$ at station 3 (Stn 46005). The results indicate that using the default value for $C_{ds}$ (i.e. [cds2] in SWAN) has resulted in underestimation of the $H_s$. The coarse resolution of the NCEP wind data might also contribute to the $H_s$ underestimation.
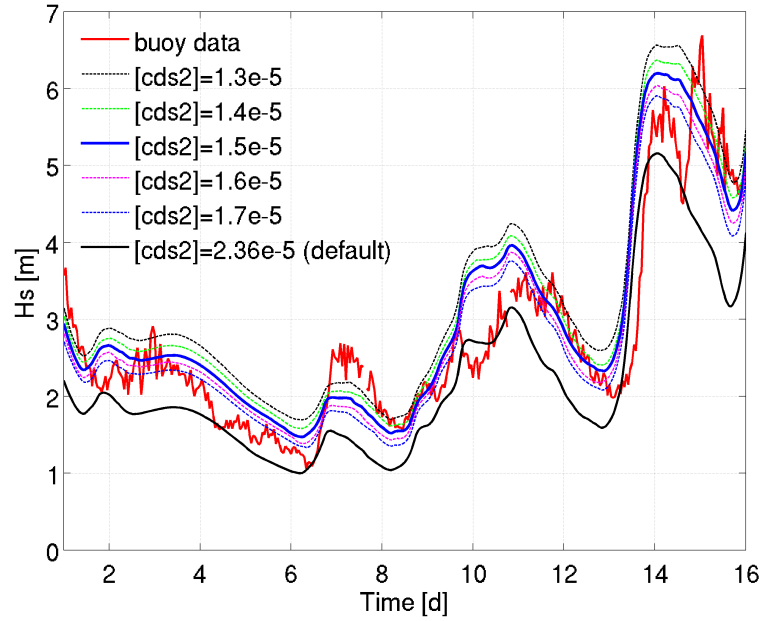


Figure 3.3: Time series of modelled $H_s$ for 1-16 January 1999 at the location of station 3 (Stn 46005) for various $C_{ds}$ values ($C_{ds}$ = [cds2] in SWAN).

Based on Eqs. 3.10 and 3.11, increasing wave steepness will result in an increase of whitecapping dissipation and thereby reduce the total wave energy density. This could lead to an underestimation of $H_s$. The default mode in SWAN does not always use the entire potential of the model and better results can be achieved by tuning some parameters or activating alternative formulations for certain physical processes (Rusu, 2011). In order to achieve good agreement between modelled results and observations, the value of the coefficient for determining the rate of whitecapping dissipation $C_{ds}$ in Eq. 3.11 was optimized. This was done by carrying out further simulations using various lower $C_{ds}$ values, i.e. $1.3 \times 10^{-5}, 1.4 \times 10^{-5}, 1.5 \times 10^{-5}, 1.6 \times 10^{-5}$ and $1.7 \times 10^{-5}$. The results of the SWAN computations with various $C_{ds}$ values are compared with the observed $H_s$. Fig. 3.3 shows the comparisons of modelled $H_s$ time series with the observed data at station 3 (Stn 46005) for different $C_{ds}$ values.

The $H_s$ results were statistically analyzed and the results of the statistical analysis are presented in Table 3.4. The average index of agreement $D$ was taken as the mean value of the $D$

Table 3.4: Average Willmott's index of agreement $D$ and average bias index

| $C_{ds}$ or [cds2] | $1.3 \times 10^{-5}$ | $1.4 \times 10^{-5}$ | $1.5 \times 10^{-5}$ | $1.6 \times 10^{-5}$ | $1.7 \times 10^{-5}$ | $2.36 \times 10^{-5}$ |
|---|---|---|---|---|---|---|
| Average $D$ index | 0.896 | 0.907 | 0.909 | 0.906 | 0.896 | 0.780 |
| Average bias index | 0.065 | 0.020 | -0.018 | -0.055 | -0.089 | -0.263 |

indices for stations 1-9. Similar calculation was performed for the average bias index. From Table 3.4, the statistical parameters provide a perspective regarding the accuracy of the results and the tendency of the estimations. Having the average index $D = 0.909$, which is the closest to unity, and the average bias index = -0.018, which is the smallest value, therefore, the tunable parameter $C_{ds}$ was set equal to $1.5 \times 10^{-5}$ as the most appropriate value and was used in the remainder of the simulations in this study. The *bias* of -0.018 indicates that on average the simulated solution under predicts the observed data by 1.8%.

Table 3.5 summarizes the two statistical parameters for each station with respect to the observed data for $C_{ds} = 1.5 \times 10^{-5}$. In general, the $D$ indices indicate that the agreement between the modelled and observed $H_s$ is very good with most of the $D$ index values are equal or greater than 0.85 except for Stn 51028, which has the lowest $D$ index of 0.76. The *bias* indices indicate that the estimation errors are less than 10% for all stations except for Stn 46022 where the modelled results under predict the observed $H_s$ by 12% on average.

Table 3.5: Willmott's $D$ index and bias index for $H_s$ for stations 1-9 with $C_{ds} = 1.5 \times 10^{-5}$

| Stations | $D$ index | bias index |
|---|---|---|
| 1. Stn 46035 | 0.95 | -0.01 |
| 2. Stn 46006 | 0.95 | 0.02 |
| 3. Stn 46005 | 0.96 | 0.03 |
| 4. Stn 46022 | 0.90 | -0.12 |
| 5. Stn 46059 | 0.97 | -0.04 |
| 6. Stn 41001 | 0.94 | -0.07 |
| 7. Stn 51003 | 0.85 | -0.02 |
| 8. Stn 51002 | 0.89 | -0.03 |
| 9. Stn 51028 | 0.76 | 0.07 |

## 3.4 Wave conditions and spectral analysis

In spectral analyses, significant wave height can be estimated as four times the square root of the total energy (SWAN Team, 2011b):

$$H_s = 4\sqrt{E_{tot}} \tag{3.21}$$

The time series of modelled $H_s$ (in blue), as shown in Figs. 3.4 and 3.5 are in reasonable agreement with the observed $H_s$ (in red) compiled from the NDBC observations. In general, the
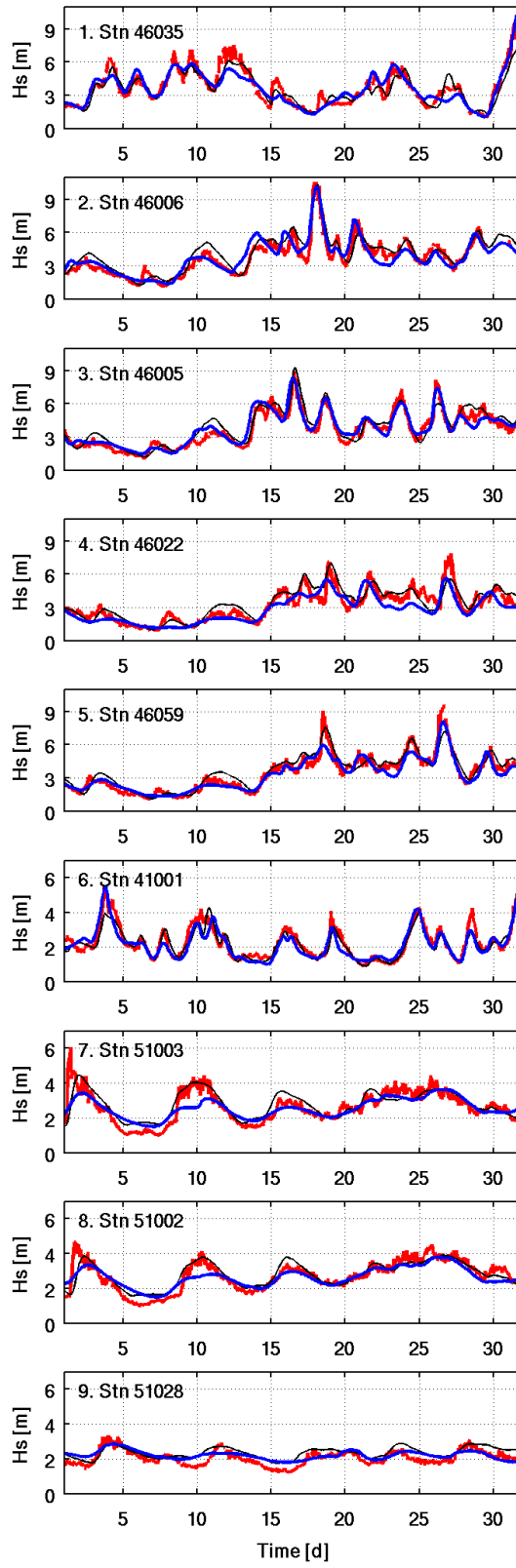
Figure 3.4: Time series of $H_s$ for January 1999 at NDBC Buoy Stations 1-9. Measured data in red, SWAN results in blue and WW3 results in black.
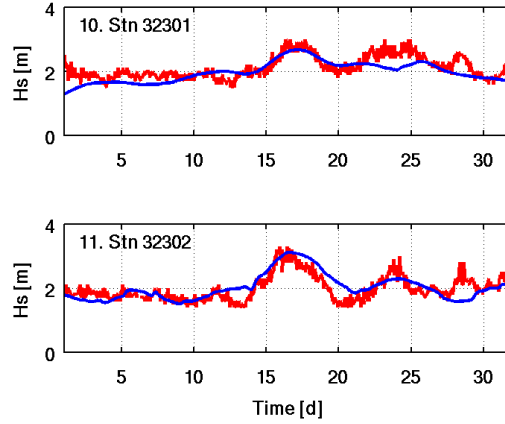
Figure 3.5: Time series of $H_s$ for March 1986 at NDBC Buoy Stations 10-11. Measured data in red and SWAN results in blue.

significant wave heights during extreme events (e.g. at stations 1-2) are fairly well reproduced by the SWAN model. Some $H_s$ values are underpredicted, e.g. at station 4. The discrepancies can be attributed to the accuracy and the resolution (i.e. 6-hourly) of the wind speed data used to force the model. Time series of $H_s$ from WW3, extracted and interpolated from the historical archived data from the NOAA WW3 global ocean wave model (http://polar.ncep.noaa.gov/waves/wavewatch), are plotted in Fig. 3.4 to qualitatively provide a comparative visual overview with the $H_s$ computed from SWAN as well as with the NDBC observations. Note that WW3 global model used 3-hourly winds as wind input.

Observed versus predicted scatterplot of $H_s$ for all the data at the locations of stations 1-9 are plotted in Fig. 3.6 to illustrate the comparative data description and provide visual credibility to the quantitative comparison. A black solid 1:1 line is drawn as a reference of perfect agreement between the observed and modelled $H_s$ under ideal condition. The plot suggests that the observed and modelled results generally agree with each other. Fig. 3.7 illustrates an example of the computed $H_s$ contours of SWAN and WW3 for 14 January 1999 where a storm was approaching the South Shetland Islands from the west. It is reassuring that the $H_s$ pattern of SWAN appears to be consistent with the modelled results extracted from the WW3 model.

The performance of the smaller nested model in the South Shetland Islands region (Fig. 3.1d) was assessed by comparing the modelled $H_s$ with the measurements from the ERS-2 and Topex/Poseidon satellites (Fig. 3.8a). Fig. 3.8b shows the comparisons of the modelled and satellite-derived $H_s$ for three selected satellite tracks, i.e. A*-A, B*-B and C*-C. The asterisk (*) indicates the location of the first data record along the corresponding satellite track within the model domain. Fig. 3.8c shows a scatterplot of observed versus modelled $H_s$ for all the track points. By taking all the satellite records into account, the $D$ index of agreement and bias index were calculated to be 0.90 and 0.014, respectively, indicating a good agreement between the model and the measurements.
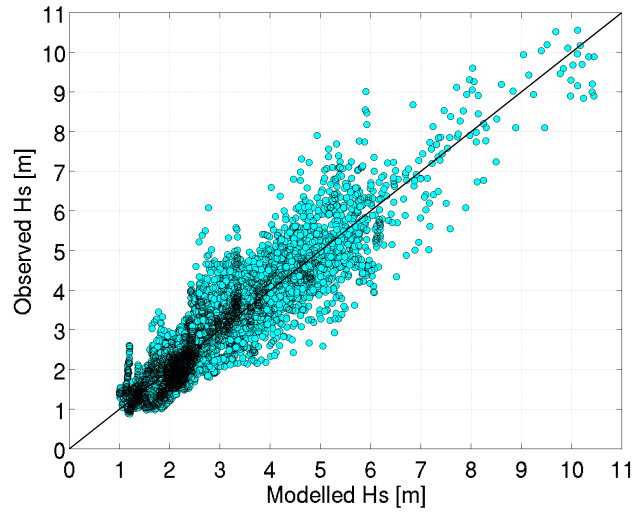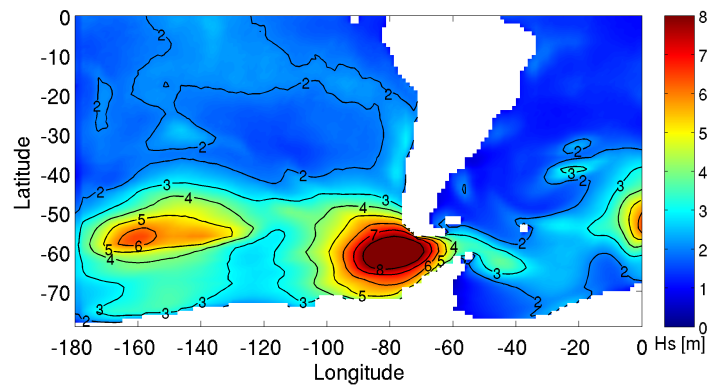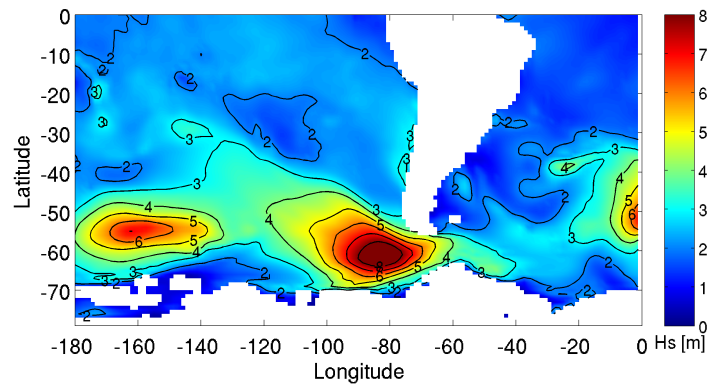
21

Figure 3.6: Scatterplot of observed versus predicted significant wave heights for January 1999 at the locations of stations 1-9.



(a) Significant wave height (SWAN)



(b) Significant wave height (WW3)

Figure 3.7: Significant wave height contours of SWAN and WW3, 14-01-1999, 00:00:00 UTC. A storm was approaching the South Shetland Islands from the west.
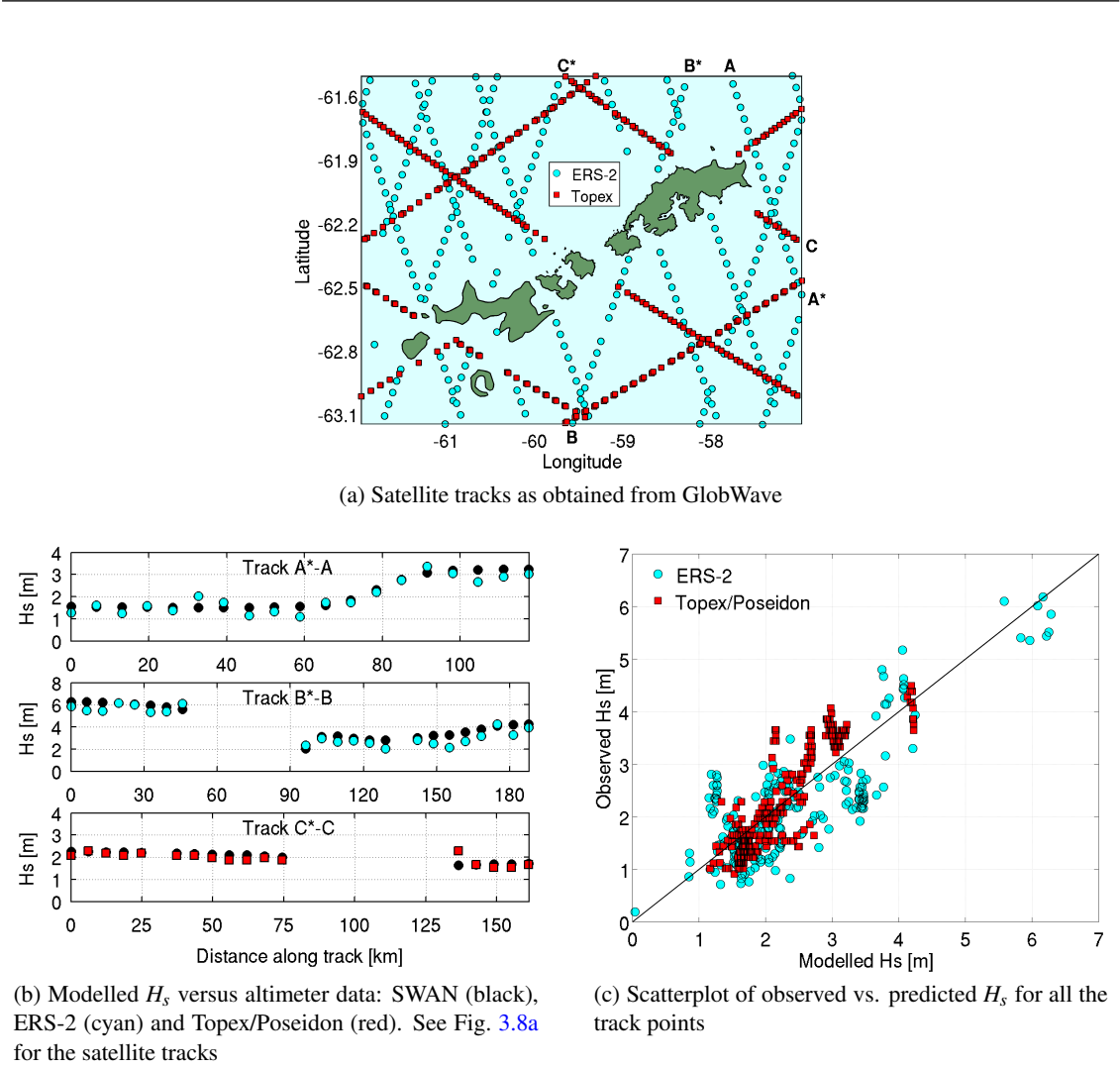
(a) Satellite tracks as obtained from GlobWave



(b) Modelled $H_s$ versus altimeter data: SWAN (black), ERS-2 (cyan) and Topex/Poseidon (red). See Fig. 3.8a for the satellite tracks

(c) Scatterplot of observed vs. predicted $H_s$ for all the track points

Figure 3.8: Comparison between modelled $H_s$ and altimeter data for January 1999 for the model domain as shown in Fig. 3.1d.

Fig. 3.9 presents the spatial distribution of the modelled $H_s$ around the waters of the South Shetland Islands and Northern Antarctic Peninsula (left panels), and Maxwell Bay (middle panels) and Potter Cove (right panels) for four different wave conditions from mild to rough sea states. The corresponding wind speeds and directions are shown in Fig. 3.10. Waves propagate from the open seas such as Drake Passage and Southern Ocean into the Bransfield Strait through the many smaller straits between the South Shetland Islands and the waters from the Bellingshausen and Weddell Seas. Part of the waves are diffracted at the northeastern end of King George Island before they propagate into the Bransfield Strait, which is located between the northern tip of the Antarctic Peninsula and the South Shetland Islands. The waves then travel from the Bransfield Strait into Maxwell Bay before they refract into Potter Cove over a complex sea bottom topography.

Surrounded by the South Shetland Islands, the Bransfield Strait is generally sheltered from

(a) 13-Jan-1999, 00:00:00 UTC, mild sea state around Maxwell Bay and Potter Cove

(b) 15-Jan-1999, 00:00:00 UTC, rough sea state around Maxwell Bay and Potter Cove

(c) 16-Jan-1999, 00:00:00 UTC, moderate sea state around Maxwell Bay and Potter Cove

(d) 19-Jan-1999, 00:00:00 UTC, rough sea state around Maxwell Bay and Potter Cove
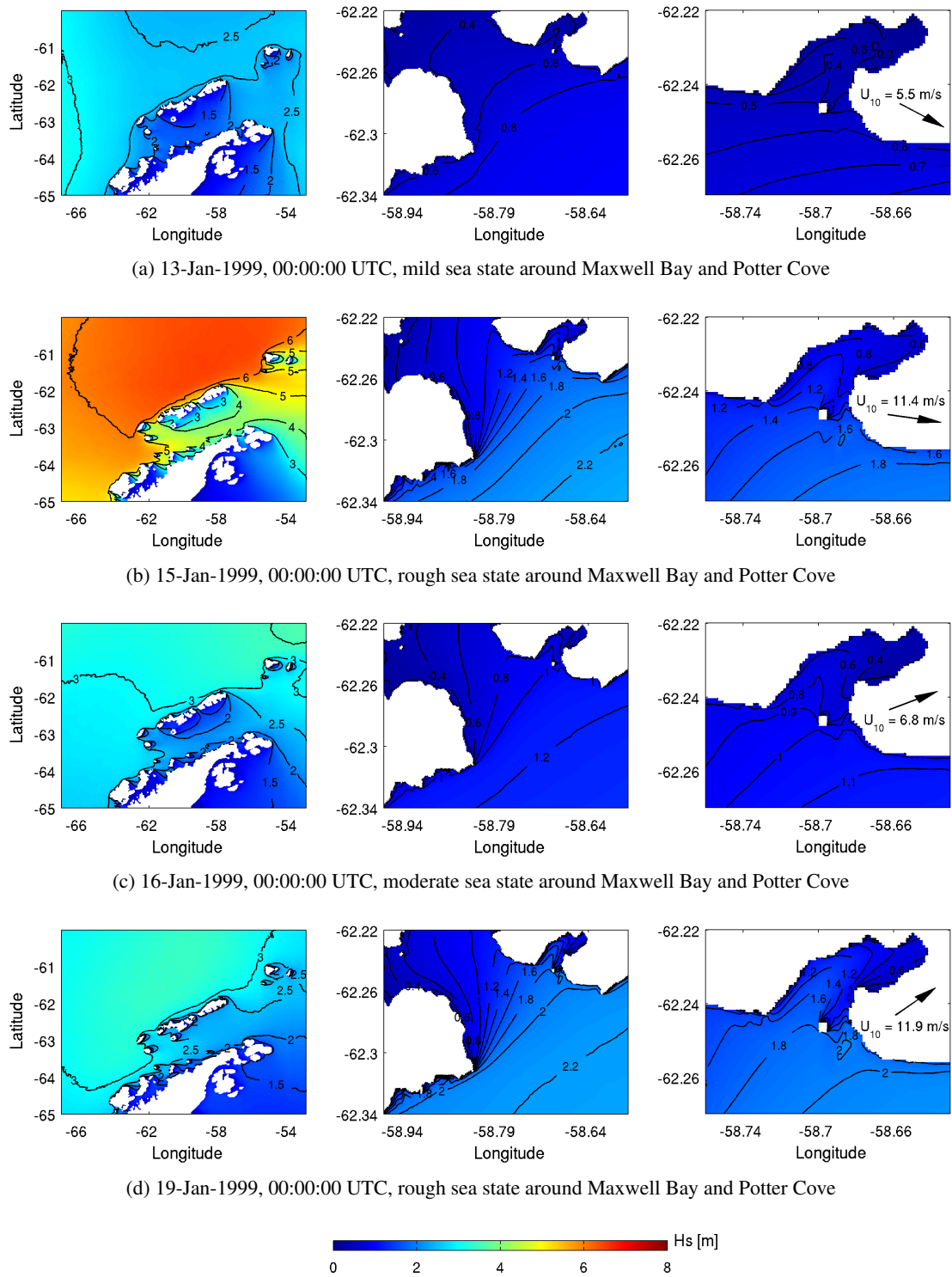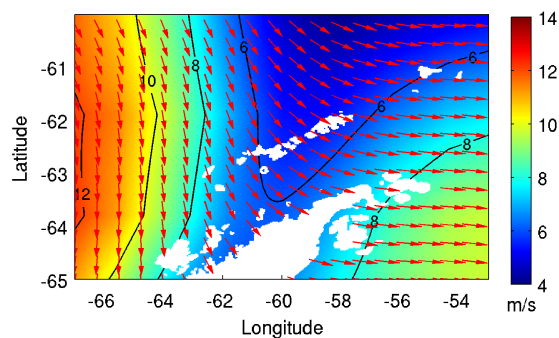
Figure 3.9: Significant wave height contours around the waters of the South Shetland Islands and Northern Antarctic Peninsula (left panels), Maxwell Bay (middle panels) and Potter Cove (right panels). The arrows mark the wind directions around Potter Cove together with the wind speeds, which are corresponding to the wind velocity fields as shown in Fig. 3.10.

(a) Wind velocity, 13-Jan-1999, 00:00:00 UTC
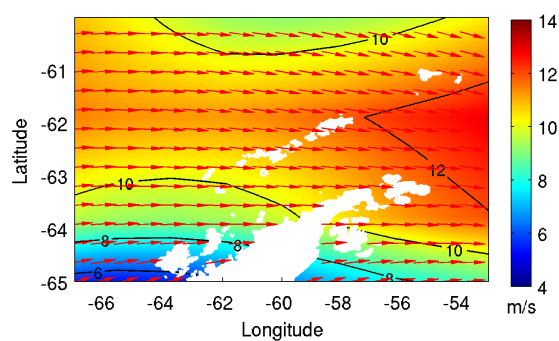

(b) Wind velocity, 15-Jan-1999, 00:00:00 UTC
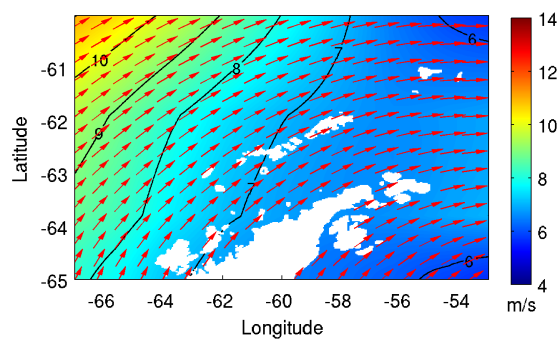

(c) Wind velocity, 16-Jan-1999, 00:00:00 UTC
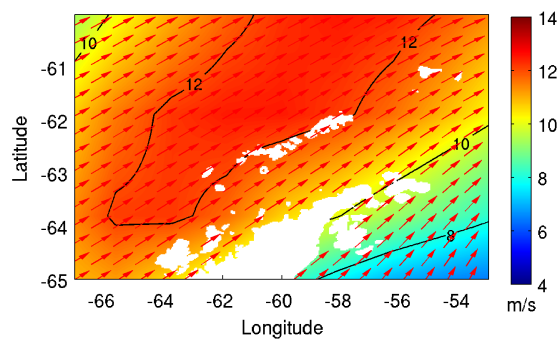

(d) Wind velocity, 19-Jan-1999, 00:00:00 UTC

Figure 3.10: Wind fields around the South Shetland Islands and Northern Antarctic Peninsula.

extreme wave conditions (see the left panels of Fig. 3.9). The event on 15-Jan-1999, 00:00:00 UTC, where a storm with $H_s$ of over 6 m was approaching from the open sea, is particularly distinct to demonstrate the sheltering effect of the islands by a reduction of the $H_s$ in the Bransfield Strait. In general, the terms 'mild', 'moderate' and 'rough' are used in this thesis to cover and describe the various wave conditions or sea states in Maxwell Bay and Potter Cove. The middle and right panels of Fig. 3.9 illustrate the three different wave conditions in Maxwell Bay and Potter Cove: (1) mild sea state (Fig. 3.9a); (2) moderate sea state (Fig. 3.9c); and (3) rough sea state (Figs. 3.9b and 3.9d). Comparing the two rough sea states on 15-Jan-1999 and 19-Jan-1999, it was observed that both events had almost similar $H_s$ distribution pattern, with the 19-Jan-1999 event having slightly larger $H_s$ in Maxwell Bay and Potter Cove. This shows that although the storm with $H_s$ of over 6 m from the open ocean on 15-Jan-1999 resulted in an increase of $H_s$ in Bransfield Strait, it seems to have had no major impact on the wave conditions in Maxwell Bay and Potter Cove.

In order to further identify whether the wave states around Maxwell Bay and Potter Cove are swell-generated, locally wind-generated or mixtures of both, the distributions of wave spectra, as illustrated in Fig. 3.11, are plotted at different locations at open sea (OS), Bransfield Strait (BS), Maxwell Mouth (MM), Potter Mouth (PM), and inner cove (IC) (see Fig. 2.3). Remotely generated swells, created by storms in the open seas, may arrive in Bransfield Strait and Potter Cove and meet the locally generated wind sea, therefore it is not unusual that swell-generated waves are mixed with wind-sea waves. Swell waves are generally regular and long-crested, so they are characterized by narrow spectra, whereas wind seas are more irregular and short-crested and have broader spectra. The distinction between wind sea and swell from the wave spectrum can be determined based on a separation frequency $f_s$ where frequencies higher than $f_s$ correspond to wind waves and frequencies lower than $f_s$ are from swells. The separation frequency $f_s$ (Eq. 3.22) can be related to the local wind speed $U_{10}$ based on the peak frequency $f_{PM}$ (Eq. 3.23) of the spectrum of Pierson and Moskowitz (1964):

$$f_s = 0.8 f_{PM} \tag{3.22}$$

$$f_{PM} = 0.13 \frac{g}{U_{10}} \tag{3.23}$$

A factor of 0.8 is commonly applied to indicate the separation frequency (Eq. 3.22) to account for uncertainties in the angular shift between wind and waves (Earle, 1984; Portilla et al., 2009).

In Figs. 3.11a-3.11c, unimodal density spectra with frequencies smaller than the separation frequencies $f_s$ (indicated by vertical dashed lines) can be seen in the open sea at OS on 13-Jan-1999, 15-Jan-1999 and 16-Jan-1999. These show that the wave states at OS were mainly influenced by swell waves. The wave climate at BS in the Bransfield Strait, which had clear evidence of bimodality (energy distributed between two distinct peaks), comprises both ocean swells from
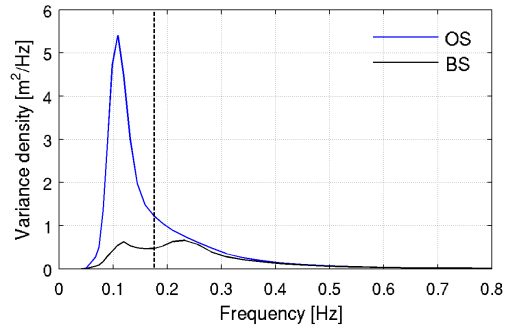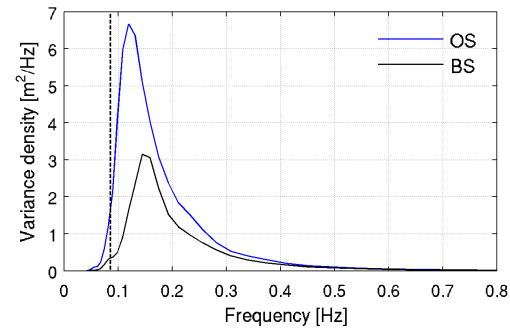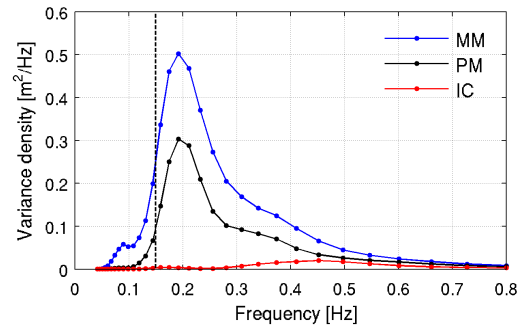
(a) Wave spectra, 13-Jan-1999, 00:00:00 UTC
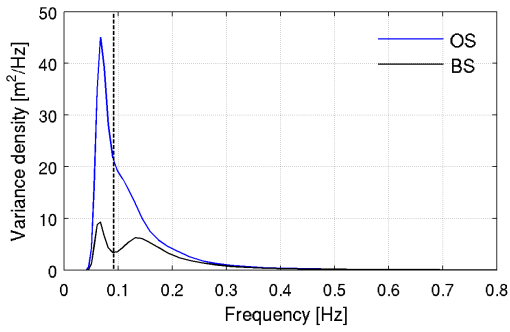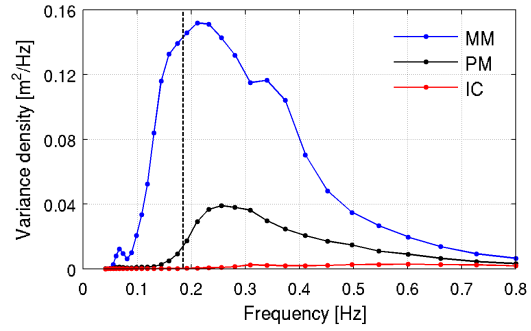


(b) Wave spectra, 15-Jan-1999, 00:00:00 UTC
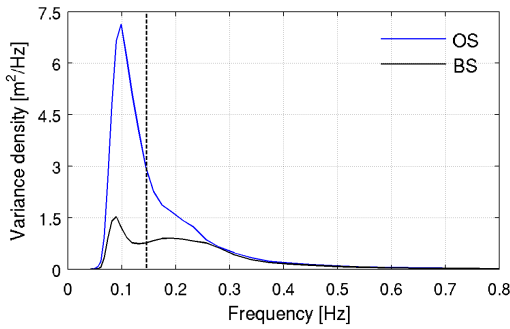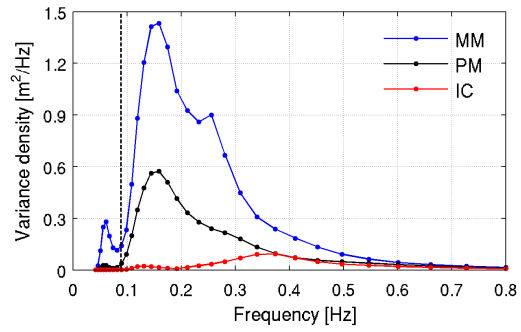


(c) Wave spectra, 16-Jan-1999, 00:00:00 UTC



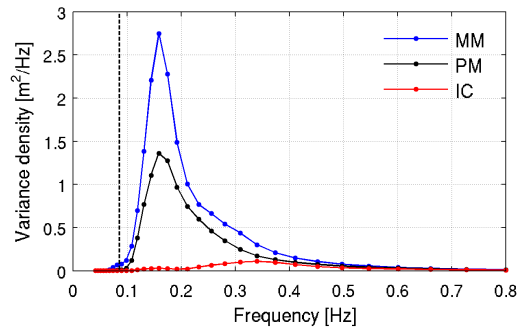(d) Wave spectra, 19-Jan-1999, 00:00:00 UTC

Figure 3.11: Wave spectra distributions at points OS, BS, MM, PM and IC. See Fig. 2.3 for the location of the points. Vertical dashed lines indicate the separation frequencies $f_s$. Lower frequencies indicate swells, higher frequencies indicate locally generated wind seas.

the opean seas and locally generated wind seas. As waves travelled from the Bransfield Strait into Maxwell Bay, it is noticeable that the sea states at MM (near the mouth of Maxwell Bay) had peak frequencies around 0.14-0.21 Hz, indicating that the wave conditions were influenced by wind seas generated by the local weather conditions. Low energy peaks smaller than 0.1 Hz (or greater than 10 s) are seen at MM, which were likely to be the remnant swell waves propagating towards the Maxwell Bay from the Bransfield Strait.

At PM (near the mouth of Potter Cove) and IC (inner cove), the shapes of the wave spectra are broader with most of the frequencies higher than $f_s$. The results indicate that the wave climate in Potter Cove was strongly influenced by the local wind conditions and only subject to minimal swell energy (those with frequencies lower than $f_s$). From the wave spectra distributions on 15-Jan-1999 (Fig. 3.11b), it was observed that the highly energetic swell conditions in the open seas (e.g. peak variance density of about 45.1 $m^2$/Hz at OS) had a relatively large impact on the wave climate in Bransfield Strait (e.g. peak variance density of about 9.3 $m^2$/Hz at BS) but they had no significant influence on the sea states in Potter Cove (variance density generally below 0.03 $m^2$/Hz). On 19-Jan-1999, the wave condition in the study area comprised mainly of locally generated wind waves (Fig. 3.11d). Given that the wind velocities around Maxwell Bay and Potter Cove were generally larger on 19-Jan-1999 than 15-Jan-1999 (see Fig. 3.10), it can be seen from the spectra distributions (frequencies higher than $f_s$) that the locally wind-generated waves produced higher variance densities.

Fig. 3.9 (middle panels) shows that the opening of Potter Cove is exposed directly to the incident waves from the Bransfield Strait and the spatial evolution of the $H_s$ in Potter Cove for the various sea states are depicted in the right panels. The corresponding $H_s$ near the mouth of Potter Cove (PM, see Fig. 2.3b) and inner cove (IC) are summarized in Table 3.6, as $H_{s,mouth}$ and $H_{s,inner}$, respectively. During the various wave conditions, the significant wave heights at the inner cove IC were found to be about 40-50% smaller than the ones near the mouth at PM.

Table 3.6: Different wave conditions near the mouth (PM) and inner water (IC) of Potter Cove

| Date, time [UTC] | Sea state | $H_{s,mouth}$ [m] | $H_{s,inner}$ [m] |
|---|---|---|---|
| 13-01-99, 00:00 | Mild | 0.43 | 0.17 |
| 15-01-99, 00:00 | Rough | 1.27 | 0.64 |
| 16-01-99, 00:00 | Moderate | 0.87 | 0.33 |
| 19-01-99, 00:00 | Rough | 1.69 | 0.71 |

During the mild sea state on 13-Jan-1999, the $H_s$ reduces gradually from about 0.4-0.5 m at the mouth of Potter Cove to below 0.2 m at the inner cove (see the right panel in Fig. 3.9a). The $H_s$ varies between 0.8-0.9 m at the mouth during the moderate sea state on 16-Jan-1999 and the significant wave heights were attenuated to below 0.4 m at the inner cove (see the right panel in Fig. 3.9c). For the two rough sea states, the local $H_{s,mouth}$ (1.69 m) and $H_{s,inner}$ (0.71 m) on 19-Jan-1999 are higher than the $H_{s,mouth}$ (1.27 m) and $H_{s,inner}$ (0.64 m) on 15-Jan-1999, as given

in Table 3.6. Figs. 3.9b and 3.9d (right panels) compare the $H_s$ distributions in Potter Cove for the two rough sea states. As previously mentioned, the wave conditions in Potter Cove mainly depends on the local wind conditions. The $H_s$ is dependent upon the wind speed and the duration that the wind blows. According to Fig. 3.2, the local wind speed had been gradually decreased over the past 12 h from its peak to 11.4 m/s on 15-Jan-1999, compared to the rapid wind growth over the past 36 h to its peak at 11.9 m/s on 19-Jan-1999. The slightly higher local wind speed together with the wind growth (contrary to the relatively lower wind speed and wind decay on 15-Jan-1999) resulted in higher $H_s$ distribution in Potter Cove on 19-Jan-1999.

As waves travel into Potter Cove, the outcrop located near the opening of the cove blocks the wave travel thus creating a sheltering effect on the lee side and forming lower $H_s$. Further into the cove, due to the surface-piercing landform around Mirounga Point, the waves around Mirounga Point experience diffraction and carry relatively weaker wave energy (see Fig. 3.13 for wave energy flux) into the shadow zone towards the coast near the Carlini station (62° 14' 16" S, 58° 39' 52" W). Due to depth effect, waves also refract as they approach the coast.

The joint distributions of $H_s$-$T_p$ and $H_s$-$\tilde{\theta}$ (where $\tilde{\theta}$ is mean wave direction) for PM and IC are illustrated in Fig. 3.12 to quantify the modelled wave climate in Potter Cove for the summer month. For PM, modelled $H_s$, $T_p$ and $\tilde{\theta}$ data were sorted with bin sizes of 0.15 m, 1 s and 15°, respectively. The data for IC were binned with $\Delta H_s = 0.02$ m, $\Delta T_p = 1$ s and $\Delta\tilde{\theta} = 15°$. The joint distribution $JD$, e.g. $H_s$-$T_p$, was calculated according to Lettmann et al. (2009) as follows:

$$JD(H_s, T_p) = \frac{n_{bin}(H_s, T_p)}{N_{data}} \times 100 \qquad (3.24)$$

where $n_{bin}$ is the number in a specific bin, and $N_{data}$ is the total number of data.

Based on the modelled results for January 1999, the dominant significant wave heights were approximately 0.4 m at PM and peak periods were 3.5 s, with predominant wave direction from the south (Fig. 3.12a). Cartesian convention, i.e. the direction to where the vector points, measured counterclockwise from the positive $x$-axis of the system, is used for the mean wave direction $\tilde{\theta}$. From the same figure, it can be clearly seen that there was another dominant wave condition at PM with significant wave heights of about 0.7 m and peak periods of 4.5 s, coming from the southwest direction. As for IC, two predominant wave conditions were found commonly coming from the W-SW quadrant: (1) $H_s$ below 0.2 m and $T_p = 1.5$ s; and (2) $H_s = 0.4$ m and $T_p = 2.5$ s (Fig. 3.12b). The modelled results show that the wave conditions during the summer month of January 1999 were generally mild and moderate with occasional occurrences of rough seas. The modelled results also provide a general overview of the spatial distributions of various wave height conditions (in terms of $H_s$) in Potter Cove from mild to moderate to rough sea states, which have not been studied previously.

(a) $H_s$-$T_p$ and $H_s$-$\tilde{\theta}$ joint distributions for PM



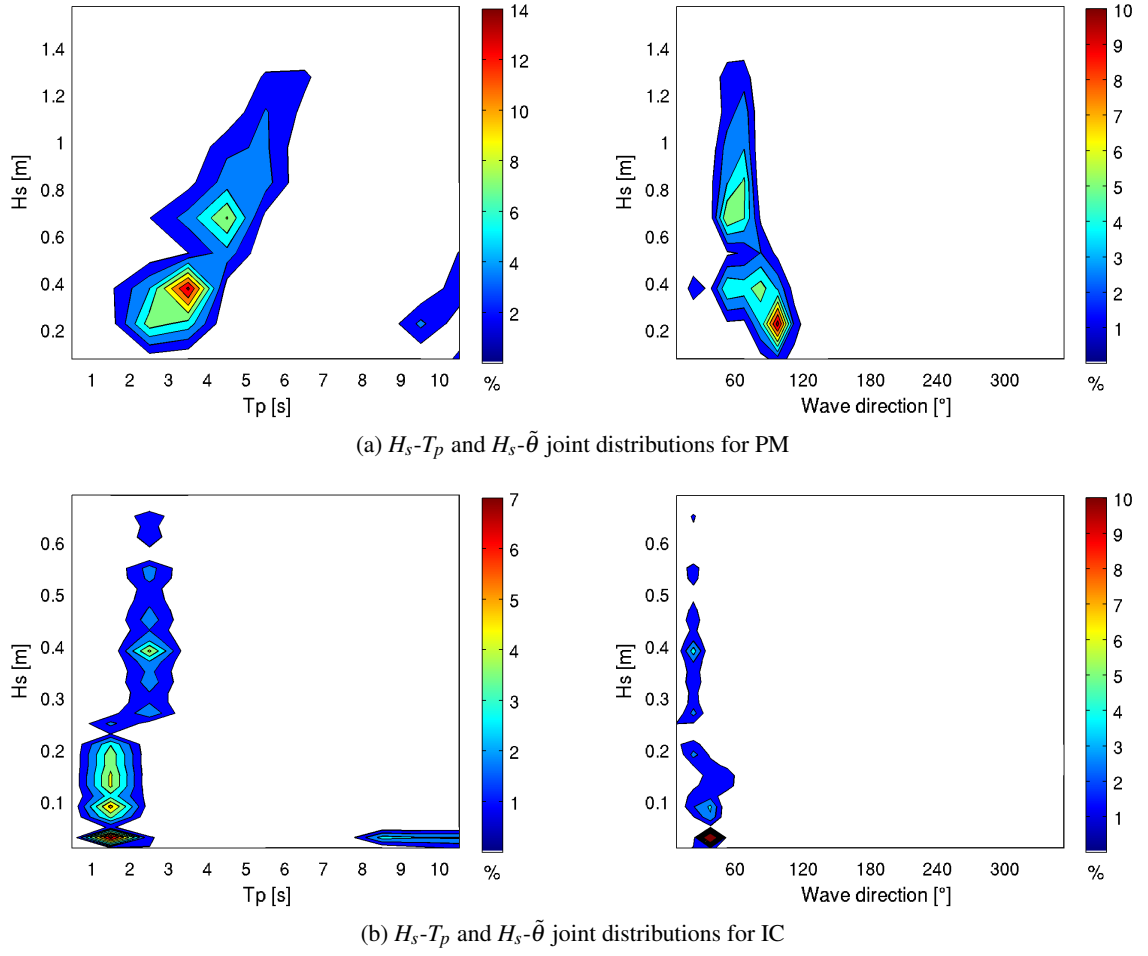(b) $H_s$-$T_p$ and $H_s$-$\tilde{\theta}$ joint distributions for IC

Figure 3.12: Joint distributions of $H_s$-$T_p$ and $H_s$-$\tilde{\theta}$ at PM and IC for January 1999. Note the mean wave direction $\tilde{\theta}$ is taken counterclockwise from geographic East.

## 3.5 Wave energy flux and dissipation

### 3.5.1 Wave energy flux

As waves propagate in the ocean, their energy is transported. As a result, the wave energy flux, which flows in the direction of wave propagation, can be estimated by the following energy transport components:

$$P_\lambda = \rho g \iint c_{g,\lambda} \, E(\sigma,\theta) \, d\sigma d\theta \tag{3.25a}$$

$$P_\varphi = \rho g \iint c_{g,\varphi} \, E(\sigma,\theta) \, d\sigma d\theta \tag{3.25b}$$

where $c_{g,\lambda}$ and $c_{g,\varphi}$ are the components of the group velocity. For the present study, in the absence of currents, the group velocity $(c_{g,\lambda}, c_{g,\varphi})$ is equal to the propagation velocity of energy $(c_\lambda, c_\varphi)$.

Wave energy is measured as the amount of power (in W) and the energy flux is expressed in W/m, i.e. energy transport per meter of wave front. The absolute value of the energy transport or wave power is given by:

$$P = \sqrt{P_\lambda^2 + P_\varphi^2} \tag{3.26}$$

The duration frame considered in the simulations in this study covers various energetic situations in Potter Cove. Fig. 3.13 presents the wave energy flux distributions, both the wave power scalar fields and the energy transport vectors, in Potter Cove for various sea states. Figs. 3.13a and 3.13c correspond to the energetic conditions encountered during the mild and moderate sea states on 13-Jan-1999 and 16-Jan-1999, respectively and the other two (Figs. 3.13b and 3.13d) relate to the energetic patterns of the rough sea conditions describing decaying waves (15-Jan-1999) and growing waves that nearly reached their energetic peak (19-Jan-1999). It was observed that the overall patterns of the wave power fields more or less follow the ones of the $H_s$ (see the right panels in Fig. 3.9). However, both wave power and significant wave height patterns do not always correspond to each other. This is due to the fact that the wave power is also governed by the group velocity ($c_{g,\lambda}$, $c_{g,\varphi}$), as defined in Eqs. 3.25 and 3.26.



(a) Mild sea state, 13-Jan-1999, 00:00:00 UTC

(b) Rough sea state, 15-Jan-1999, 00:00:00 UTC

(c) Moderate sea state, 16-Jan-1999, 00:00:00 UTC
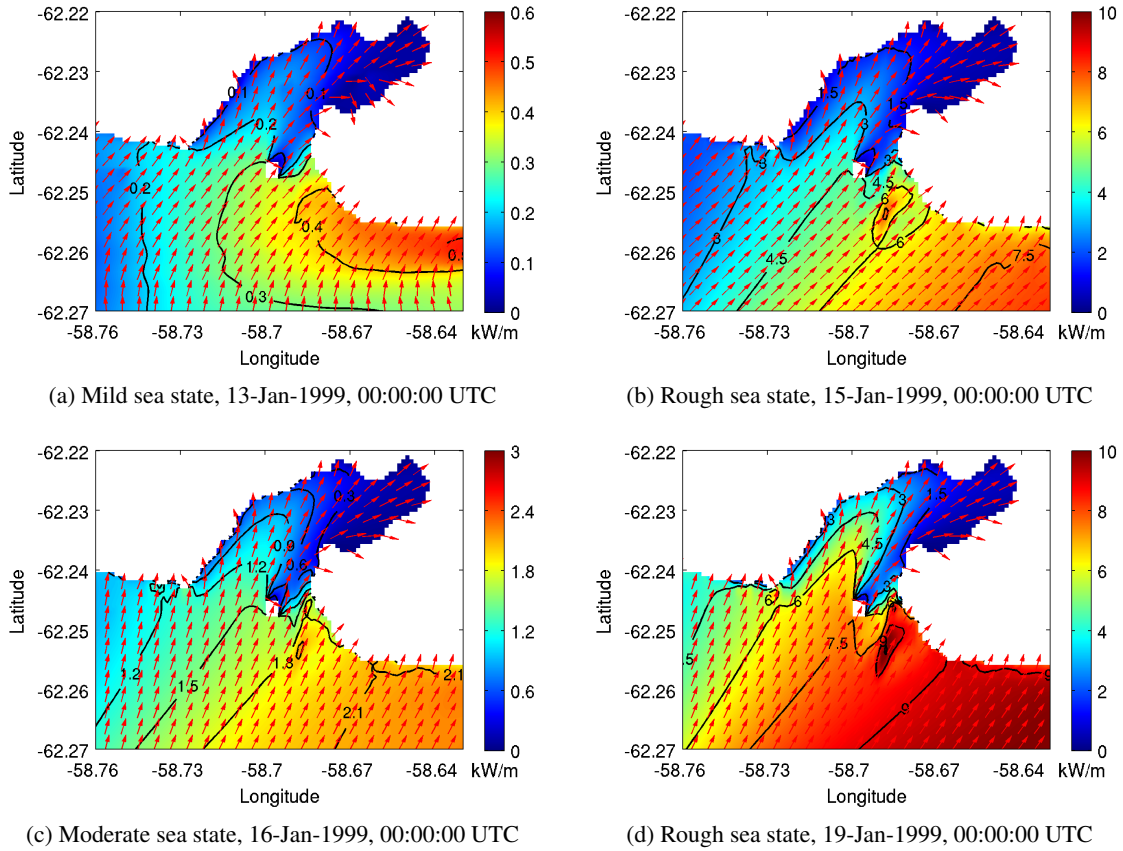
(d) Rough sea state, 19-Jan-1999, 00:00:00 UTC

Figure 3.13: Wave energy flux in Potter Cove in kW per meter of wave front. Colour background shows the wave power and the arrows show the energy transport vectors.

The wave power in Potter Cove is generally low, regardless of any sea states reported in Section 3.4. The overall level of wave power is generally below 0.3 kW/m during mild sea state and below 1.5 kW/m during moderate sea state, as represented by the scenarios on 13-Jan-1999 and 16-Jan-1999, respectively. During the rough sea state on 19-Jan-1999, approximately 7 kW/m wave power was available near the opening of Potter Cove in deeper water depths and wave power gradually decreases towards the inner cove. In general, the results present an overview of the tendencies of the wave energy flux in Potter Cove for various wave conditions.

### 3.5.2  Wave energy dissipation



(a) Total energy dissipation

(b) Dissipation due to whitecapping

(c) Dissipation due to bottom friction

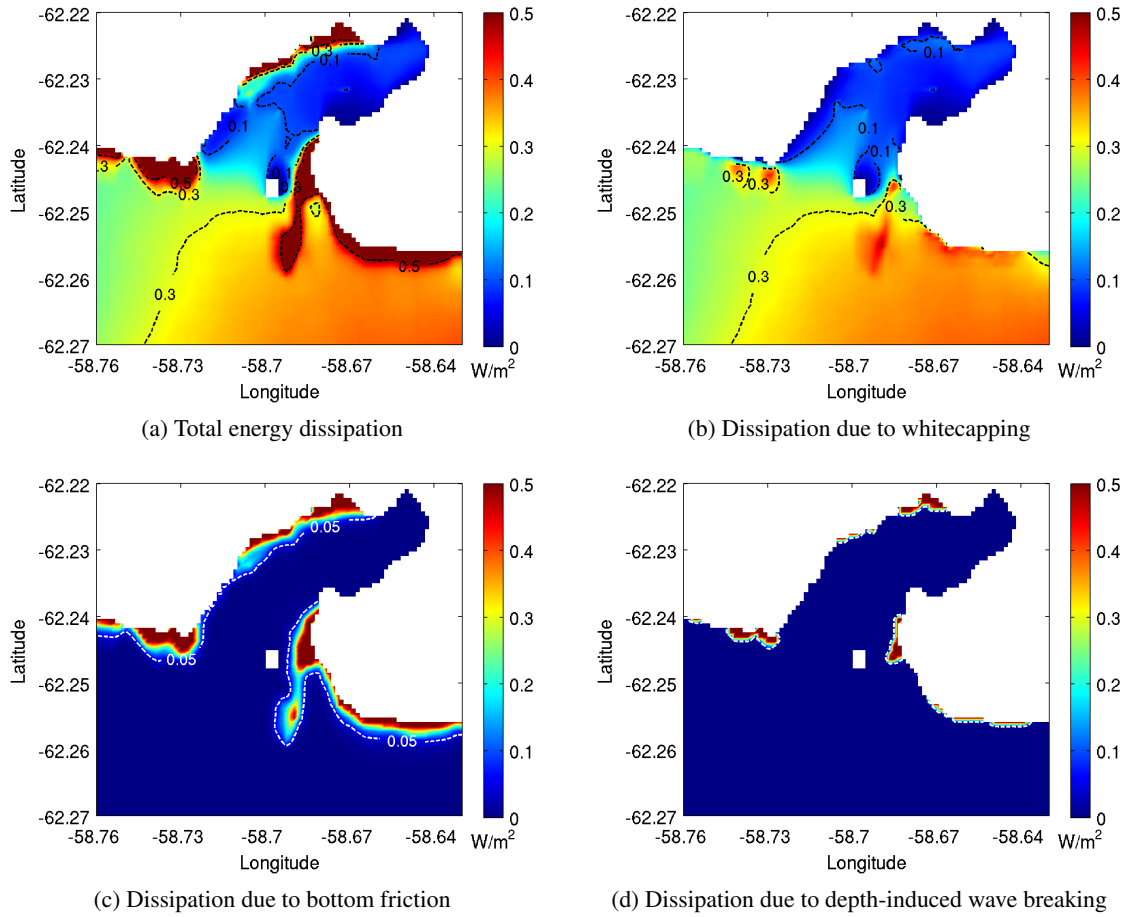(d) Dissipation due to depth-induced wave breaking

Figure 3.14: Wave energy dissipation in Potter Cove, 19-Jan-1999, 00:00:00 UTC.

The distributions of wave energy dissipation of various processes in Potter Cove for the scenario of 19-Jan-1999 are shown in Fig. 3.14. The total energy dissipation resulting from the sum of whitecapping, bottom friction and depth-induced wave breaking is depicted in Fig. 3.14a. Appreciable wave energy is dissipated around Winship Point, along the northern coastal water of Potter Cove, and the western and southern coastal areas along the perimeter of Potter Penin-

sula. The geographical variation of whitecapping dissipation in Fig. 3.14b clearly shows that the whitecapping dissipation in deeper water, mostly around the opening and offshore of Potter Cove, is dominant. Bottom friction becomes significant along the shallower areas (Fig. 3.14c) where white dashed lines of 0.05 W/m$^2$ mark and approximate the areas where wave-bottom interaction begins to occur. Depth-induced wave breaking is only important in the very shallow regions where wave energy is dissipated rapidly at certain isolated coastal locations as shown in Fig. 3.14d. Simulations from the model indicate that the processes such as wave-bottom interaction and depth-induced wave breaking only appear in the shallow water zone. For the rest of the cove, the water depths are too deep to experience shallow water effects on wave evolution.

# Chapter 4

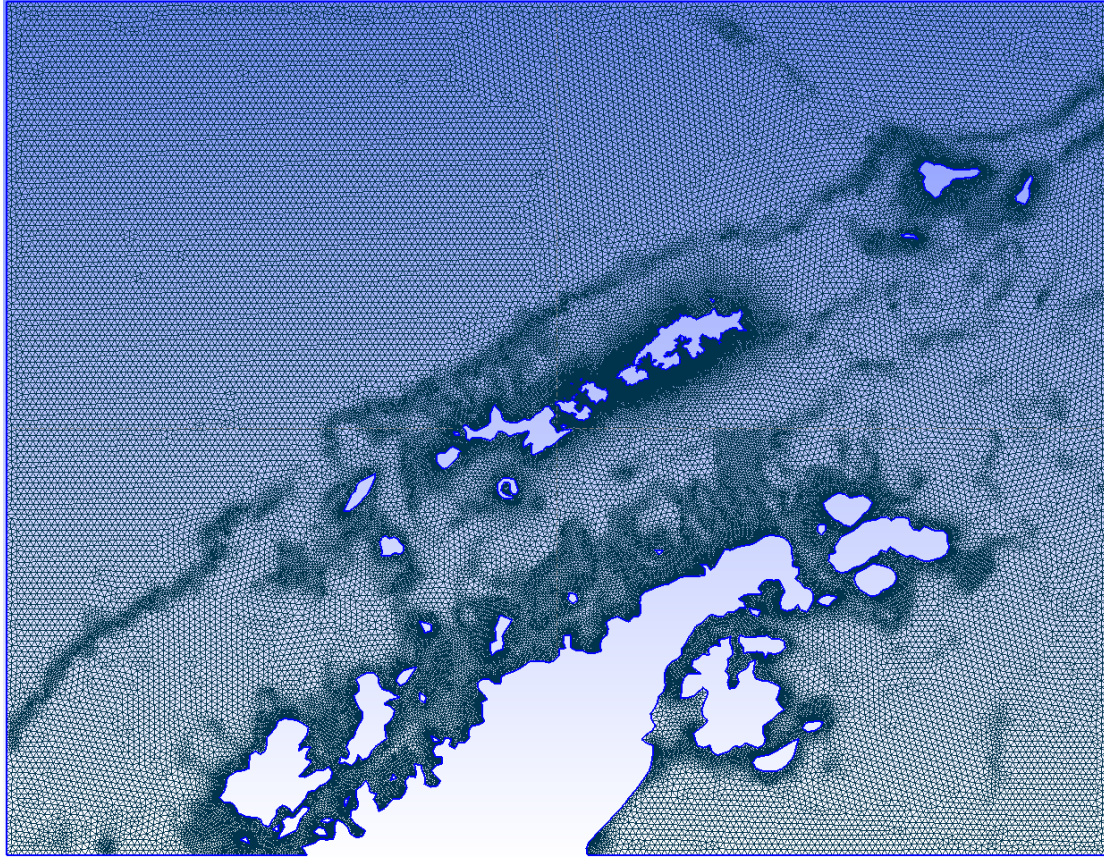# Hydrodynamic modelling

## 4.1 Model descriptions (FVCOM and FVCOM-SWAVE)

### 4.1.1 The governing equations of motion

The unstructured grid, finite-volume coastal ocean model FVCOM (Chen et al., 2003) was used to compute the tides and currents in Potter Cove. The model is discretized with unstructured triangular grids in the horizontal plane and a generalized terrain-following sigma coordinate vertically. Triangular grid meshes provide adequate irregular coastal boundary fitting. Fig. 4.1 shows some snapshots of the unstructured triangular meshes, generated from an open-source 3-D finite element grid generator Gmsh 2.5.0 (Geuzaine and Remacle, 2009).

The Smagorinsky and modified Mellor and Yamada level 2.5 (MY-2.5) turbulent closure schemes were applied for horizontal and vertical mixing, respectively (Mellor and Yamada, 1982; Smagorinsky, 1963). The theoretical background of the FVCOM model can be found in Chen et al. (2006, 2007). The free-surface three-dimensional primitive equations in Cartesian and $\sigma$ coordinates consist of the following momentum and continuity equations:

$$\frac{\partial uD}{\partial t} + \frac{\partial u^2 D}{\partial x} + \frac{\partial uvD}{\partial y} + \frac{\partial u\omega D}{\partial \sigma} - fvD$$

$$= -gD\frac{\partial \zeta}{\partial x} - \frac{gD}{\rho_o}\left[\frac{\partial}{\partial x}\left(D\int_\sigma^0 \rho' d\sigma'\right) + \sigma\rho'\frac{\partial D}{\partial x}\right]$$

$$+\frac{1}{D}\frac{\partial}{\partial \sigma}\left(K_m \frac{\partial u}{\partial \sigma}\right) + DF_x \tag{4.1}$$

(a) Mesh for the entire FVCOM model domain
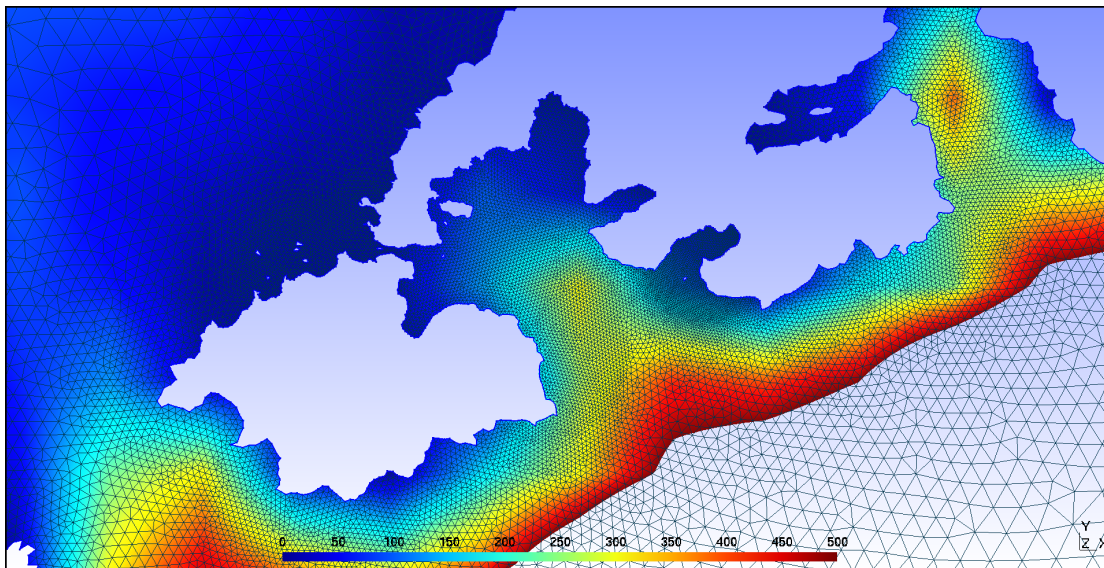


(b) Mesh around area of interest. The colour indicates the bathymetric depths (in meter) up to 500 m

Figure 4.1: Snapshots of the unstructured triangular meshes generated from Gmsh.

$$\frac{\partial vD}{\partial t} + \frac{\partial uvD}{\partial x} + \frac{\partial v^2 D}{\partial y} + \frac{\partial v\omega D}{\partial \sigma} + fuD$$

$$= -gD\frac{\partial \zeta}{\partial y} - \frac{gD}{\rho_o}\left[\frac{\partial}{\partial y}\left(D\int_\sigma^0 \rho' d\sigma'\right) + \sigma\rho'\frac{\partial D}{\partial y}\right]$$

$$+\frac{1}{D}\frac{\partial}{\partial \sigma}\left(K_m \frac{\partial v}{\partial \sigma}\right) + DF_y \tag{4.2}$$

$$\frac{\partial \zeta}{\partial t} + \frac{\partial Du}{\partial x} + \frac{\partial Dv}{\partial y} + \frac{\partial D\omega}{\partial \sigma} = 0 \tag{4.3}$$

where $x$, $y$ and $\sigma$ are the east, north and vertical axes of the Cartesian and $\sigma$ coordinates; $u$, $v$ and $\omega$ are the $x$, $y$ and $\sigma$ velocity components; $t$ is the time; $f$ is the Coriolis parameter; $\rho$ is the total density equal to a sum of perturbation density $\rho'$ and reference density $\rho_o$; $g$ is the gravitational acceleration; $K_m$ is the vertical eddy viscosity coefficient; $F_x$ and $F_y$ are the horizontal momentum diffusivity terms in the $x$ and $y$ directions. The total water column depth is $D = h + \zeta$, where $h$ is the mean water depth and $\zeta$ is the sea surface elevation. The $\sigma$-coordinate transformation (Eq. 4.4) is used in the vertical to obtain a smooth representation of irregular bottom topography:

$$\sigma = \frac{z - \zeta}{D} \tag{4.4}$$

where $z$ is the vertical axis in the Cartesian coordinate system, and $\sigma$ varies from -1 at the bottom to 0 at the surface. The governing equations are solved numerically by flux calculation over a triangular mesh using the finite-volume approach, with guarantee of mass conservation. In this study, spherical coordinates were implemented to account for the curvature of the Earth.

In order to investigate the influence of waves on the circulation in Potter Cove, a FVCOM-based wave-current model (FVCOM-SWAVE) was used for the simulation of wave-current interactions. FVCOM-SWAVE, developed by Qi et al. (2009), is an unstructured-grid finite-volume surface wave model converted from the structured-grid wave model SWAN. The evolution of wave spectra is determined by the wave action balance equation given in Eq. 3.1 and the total source-sink term expressed in Eq. 3.2. The governing equations of momentum and continuity with the inclusion of three-dimensional radiation stress, which is associated with the wave-induced circulation, can be found in Wu et al. (2011). In wave-current simulations, the parameters and source terms used in the FVCOM-SWAVE setup are the same as those used in the SWAN simulations, as described in Chapter 3, except that the time step of 150 s is used for the wave computation.

### 4.1.2 Model configurations, forcings and boundary conditions

#### 4.1.2.1 Model domain and computational grid



(a) Bathymetry and model domain

(b) Tide gauge stations

(c) Mesh around Maxwell Bay and Potter Cove
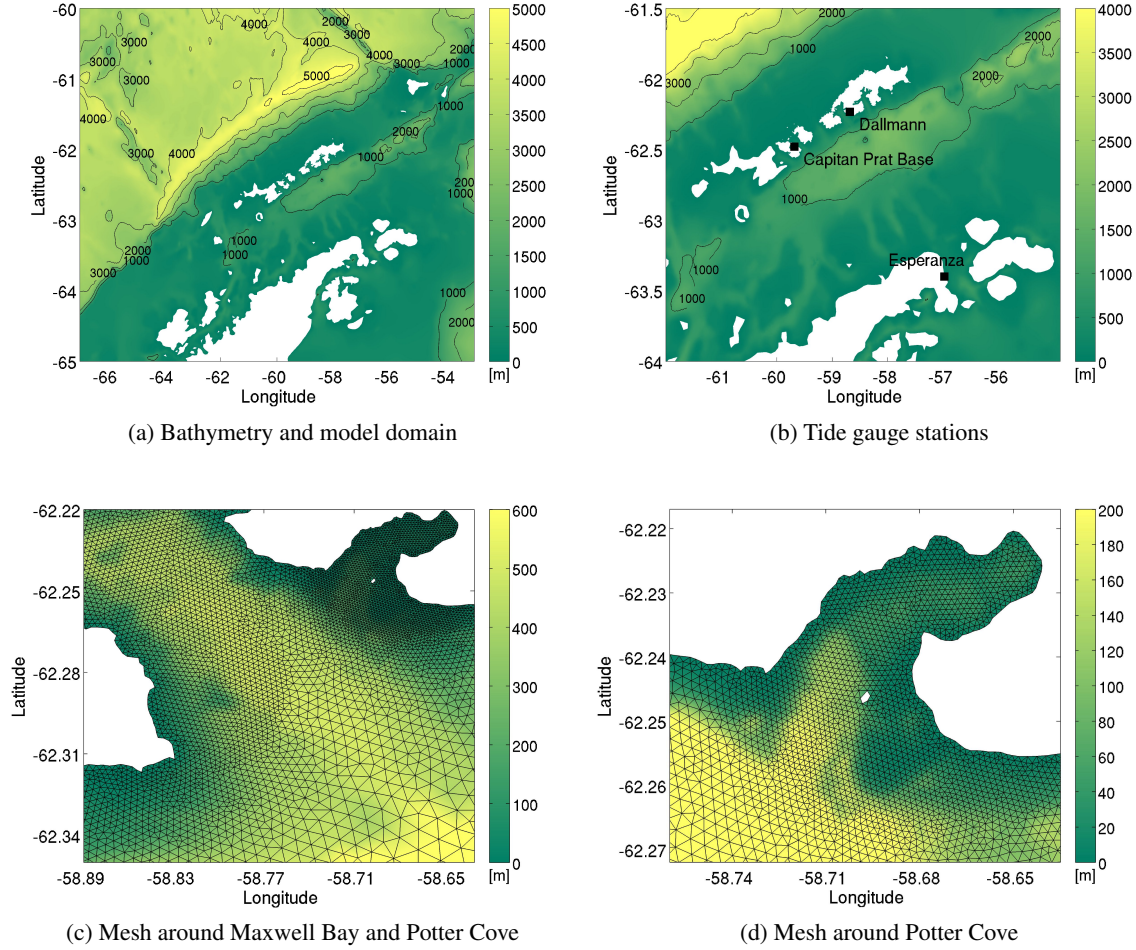
(d) Mesh around Potter Cove

Figure 4.2: The bathymetry of the study area and model domain (a), the locations of the tide gauge stations (b), the meshes around Maxwell Bay and Potter Cove (c)-(d). The colourmap and colourbar indicate the bathymetric depths in meter.

The hydrodynamic FVCOM model domain covers the region of the Northern Antarctic Peninsula (Fig. 4.2a). The coastline was created based on the details provided in Section 3.1.3.1. Tidal elevation data sets from three tide gauge stations (Fig. 4.2b) were used for the evaluation of the model simulation. The multiscale model was discretized using a triangular mesh with a total of 152,805 elements and 78,702 nodes in the horizontal plane, respectively (Fig. 4.1a). The horizontal resolution varies from approximately 1500 to 2000 m over the shelf break, up to 4000 m close to the open boundaries in the open ocean (Fig. 4.1a), about 200 m in Maxwell Bay (Fig. 4.2c) and 100 m as the highest resolution in Potter Cove (Fig. 4.2d). The domain is divided into

37

40 equidistant uniform $\sigma$ layers in the vertical. For computational efficiency, a mode-splitting technique is used in FVCOM to solve the momentum equations with two different time steps, i.e. external and internal mode time steps to adapt the faster and slower barotropic and baroclinic responses, respectively. According to Chen et al. (2006), the ratio of internal mode time step to external mode time step ISPLIT is recommended to be equal or smaller than 10. Based on the CFL criterion, computational time steps of 2 s and 10 s were used in this study for the external and internal modes, respectively, giving the ISPLIT = 5. The time step used for the wave computation is 150 s.

### 4.1.2.2 Bathymetry

The bathymetry for the model domain used for hydrodynamic modelling has been interpolated from a combination of various sources, which are similar to the ones used for wave modelling (see Section 3.1.3.2). The bathymetries of the Northern Antarctic Peninsula region and Potter Cove are shown in Fig. 4.2.

### 4.1.2.3 Tidal, wind and wave inputs

The FVCOM simulations were forced by tidal elevations with the predicted tides from the global tide model Finite Element Solution (FES2004), computed from the tidal hydrodynamic equations (derived from the classical shallow water equations) and data assimilation (Lyard et al., 2006). A new global tide model FES2012, aimed to replace the FES2004, was still not available during the time of the model simulations. Therefore, the simulations in the present study utilized the FES2004 predicted tides. For wind forcing, the models were driven by 6-hourly zonal and meridional wind speeds of the global NCEP/NCAR Reanalysis products (Kalnay et al., 1996). Wave forcing was added into the FVCOM-SWAVE model system with one-way nesting approach by prescribing the wave parameters, obtained from the hourly SWAN outputs, along the open boundaries of the model.

### 4.1.2.4 Boundary and initial conditions

Using the FES2004, the tidal elevations were interpolated to the nodes along all the open boundaries at the East, West, North and South. The model was driven and spun up by the tidal forcing specified at the open boundaries with a zero velocity field at the start. Wind is the major driving force to cause the waves to grow and is an important factor that affects the local circulation patterns in Potter Cove. Spatially varying wind speeds (and hence wind stresses) were applied to the models as surface boundary conditions. Wind stress within FVCOM is computed according to the bulk formula of Large and Pond (1981) that relates the drag coefficient (and consequently also the wind stress) to the wind speed.

For the bottom boundary, the bottom friction is described by a quadratic law with the bottom drag coefficient determined by the logarithmic bottom layer as a function of bottom roughness (Blumberg and Mellor, 1987). The minimum bottom stress drag coefficient and bottom roughness lengthscale are set to 0.0025 and 0.001 m, respectively. Wave parameters from the SWAN outputs were interpolated to the nodes along all the open boundaries for the FVCOM-SWAVE boundary conditions. With the inclusion of wind fields, the sea state develops and propagates through the computational domain.

Considering the complex bathymetry at the open boundaries, a sponge layer, with a friction (or damping) coefficient of 0.0005 at the open boundaries over a distance of influence radius of 5000 m, was used to absorb disturbances and filter computational noise at the open boundary. The sponge layer only affects the numerical solution near the boundaries and has no influence on the interior solution. This method works well and has shown to be stable throughout the simulations.

## 4.2 Tides

### 4.2.1 Goodness-of-fit and error index

The University of Hawaii Sea Level Center (UHSLC) hosts tide gauge data from around the world through three online databases, i.e. the research quality, GLOSS/CLIVAR 'fast delivery' and SLP-Pac map databases (http://ilikai.soest.hawaii.edu/uhslc/datai.html). Data in the Antarctic Peninsula region are extremely scarce. Nevertheless, hourly sea level data from three tide gauge stations were obtained for one austral summer month for the assessment of the modelled results. The stations, as shown in Fig. 4.2b, are Capitan Prat Base (ST#: 730A) at Iquique Cove, Greenwich Island; Dallmann (ST#: 682C) at Potter Cove, King George Island; and Esperanza (ST#: 601) in Hope Bay, Trinity Peninsula, Antarctic Peninsula. Table 4.1 provides the details of each station.

Table 4.1: Coordinates of the tide gauge stations, instrument types and data types. n/a: not available

| Stations | Lat (S) | Lon (W) | Instrument type | Data type |
|---|---|---|---|---|
| 1. Capitan Prat Base | 62°29' | 59°38' | Pneumatic bubbler gauge | Research quality |
| 2. Dallmann | 62°14' | 58°41' | Anderra CTD sensor 3231 | Research quality |
| 3. Esperanza | 63°24' | 56°59' | n/a | Fast delivery |

Time series of modelled and observed tidal elevations at the three stations are presented in Fig. 4.3 and the comparisons show that the model reproduces the tidal amplitudes and phases fairly well. From the tidal signals, it can be clearly seen that the tides at the three stations are comprised of mixed tides. The tidal elevation results were statistically analyzed based on Eq. 3.19 (for $D$ index) and Eq. 3.20 (for bias index) and the results are summarized in Table 4.2. The $D$ indices,

which are close to unity, for all the three stations indicate that the modelled results agree very well with the measurements. The bias indices indicate that the estimation errors are less than 1% for all stations.
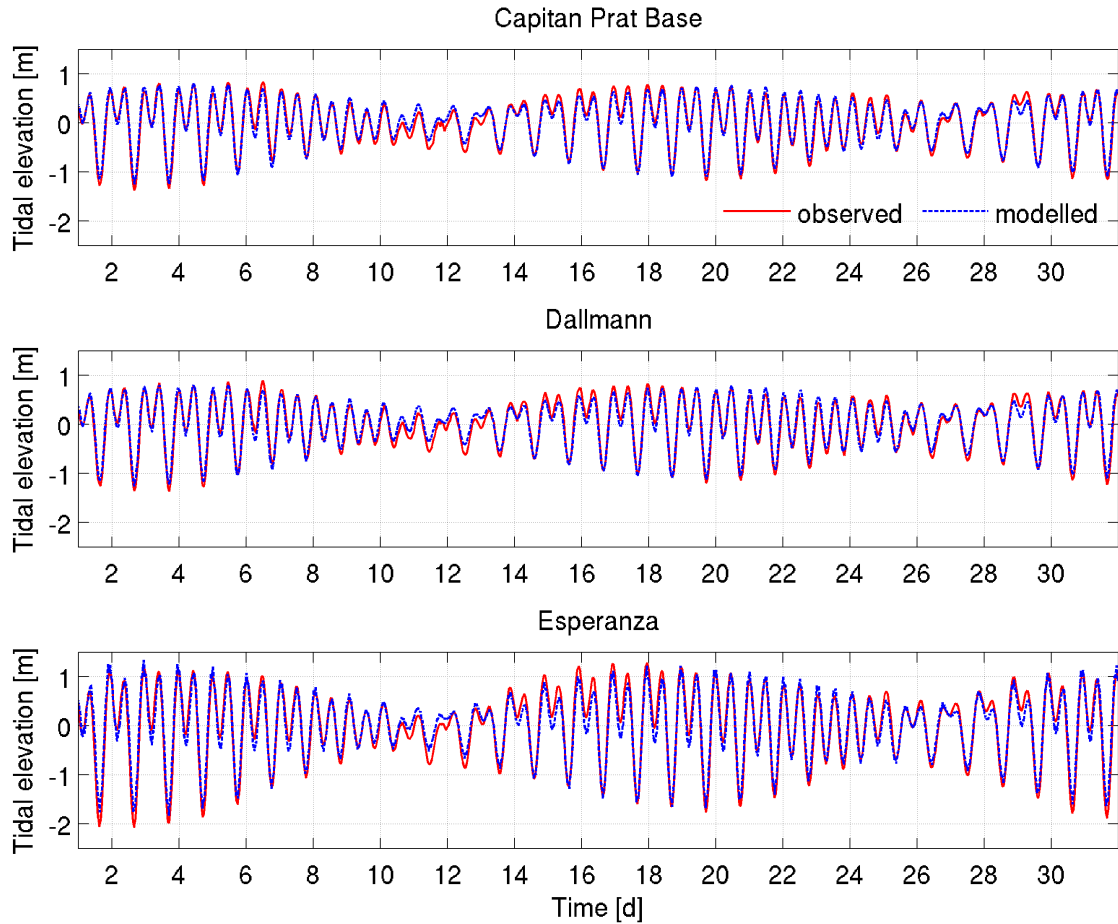


Figure 4.3: Time series of observed and modelled tidal elevations for January 1999 at Capitan Prat Base, Dallmann and Esperanza stations.

Table 4.2: $D$ index and bias index for tidal elevations for various tide gauge locations

| Stations | $D$ index | bias index (%) |
|---|---|---|
| 1. Capitan Prat Base | 0.990 | 0.82 |
| 2. Dallmann | 0.989 | 0.53 |
| 3. Esperanza | 0.986 | 0.02 |

### 4.2.2 Tidal harmonic analysis

Estimates for amplitude and phase of tidal constituents were computed using the widely-used tidal harmonic analysis program T_TIDE (Pawlowicz et al., 2002). The time series of hourly tidal elevations were analyzed for an austral summer month, i.e. January 1999, both from the modelled outputs and tide gauge data. Modelled tidal elevations were interpolated to the tide gauge locations for comparisons. Table 4.3 compares the harmonic constants of the principal semi-diurnal ($M_2$ and $S_2$) and diurnal ($K_1$ and $O_1$) constituents, together with their associated errors, at Capitan Prat Base, Dallmann and Esperanza. The phase of the constituent is reported as the Greenwich phase. The dominant tidal constituents for all the three locations are $M_2$ and $K_1$. All the four constitutents generally have reasonably small amplitude and phase errors.

The tidal regime in different locations can be classified in terms of a form factor $F$, which measures the relative strength of the diurnal and semi-diurnal tides (Pugh, 1987; Reeve et al., 2004):

$$F = \frac{K_1 + O_1}{M_2 + S_2} \tag{4.5}$$

where the tidal constituent symbols denote the amplitudes of the respective tidal constituent. The tides may be classified as follows:

| | |
|---|---|
| $F = 0$ to $0.25$ | semi-diurnal form |
| $F = 0.25$ to $1.50$ | mixed, predominantly semi-diurnal |
| $F = 1.50$ to $3.00$ | mixed, predominantly diurnal |
| $F > 3.00$ | diurnal form |

In order to describe the tidal regime at the tide gauge locations, the form factor $F$ was calculated and given in Table 4.3. The tides at all the three locations are of a mixed, predominantly semi-diurnal type, which demonstrates large inequalities in range and time between the highs and lows each day (Fig. 4.3). Within the central basin of the Bransfield Strait, the form factor $F$ slowly increases from 0.76 (modelled result) at Esperanza towards the west (or northwest) to 0.87 at Capitan Prat Base due to the decrease of the semi-diurnal constituents. Based on the modelled results, the tidal form factor $F$ and mean spring tide range $2(M_2+S_2)$ at Dallmann, Potter Cove are 0.83 and 1.36 m, respectively. A mean neap tide range, calculated as $2(M_2-S_2)$, is approximately 0.4 m for Dallmann.

The $F$ values are generally in the similar order of magnitude as reported in the literature. For instant, $F = 0.8$ for Dallmann was reported by Schöne et al. (1998) with $F = 0.81$ in 1996 and $F = 0.82$ in 1997. Ardley Cove, which is located approximately 14 km northwest of Potter Cove, was reported to have a $F$ ratio of 0.84 (Dragani et al., 2004). Both D'Onofrio et al. (2003) and Dragani et al. (2004) reported that $F = 0.75$ for Esperanza. Table 4.4 tabulates the tidal harmonic constants for Dallmann (Schöne et al., 1998) and Esperanza (D'Onofrio et al., 2003).

Table 4.3: Harmonic constants of the principal tidal constituents and their associated errors calculated from the FVCOM model and measurements obtained at Capitan Prat Base, Dallmann and Esperanza. Phase lags are referenced to Greenwich

| Station | Capitan Prat Base | | | |
| Source | FVCOM model | | Tide gauge station | |
| Constituents | Amplitude (m) | Phase (°) | Amplitude (m) | Phase (°) |
|---|---|---|---|---|
| $M_2$ | $0.425 \pm 0.003$ | $280.6 \pm 0.4$ | $0.438 \pm 0.008$ | $282.4 \pm 1.1$ |
| $S_2$ | $0.234 \pm 0.003$ | $346.3 \pm 0.7$ | $0.219 \pm 0.009$ | $344.7 \pm 2.1$ |
| $K_1$ | $0.311 \pm 0.003$ | $74.0 \pm 0.6$ | $0.351 \pm 0.010$ | $77.4 \pm 1.5$ |
| $O_1$ | $0.263 \pm 0.003$ | $46.3 \pm 0.7$ | $0.292 \pm 0.011$ | $48.0 \pm 1.9$ |
| F | 0.87 | | 0.98 | |
| $2(M_2+S_2)$ | 1.32 m | | 1.31 m | |

| Station | Dallmann | | | |
| Source | FVCOM model | | Tide gauge station | |
| Constituents | Amplitude (m) | Phase (°) | Amplitude (m) | Phase (°) |
|---|---|---|---|---|
| $M_2$ | $0.440 \pm 0.003$ | $280.1 \pm 0.4$ | $0.452 \pm 0.009$ | $283.2 \pm 1.1$ |
| $S_2$ | $0.242 \pm 0.003$ | $343.4 \pm 0.8$ | $0.224 \pm 0.011$ | $343.0 \pm 2.4$ |
| $K_1$ | $0.303 \pm 0.003$ | $73.0 \pm 0.7$ | $0.348 \pm 0.009$ | $76.1 \pm 1.6$ |
| $O_1$ | $0.260 \pm 0.004$ | $46.2 \pm 0.9$ | $0.299 \pm 0.010$ | $46.9 \pm 2.1$ |
| F | 0.83 | | 0.96 | |
| $2(M_2+S_2)$ | 1.36 m | | 1.35 m | |

| Station | Esperanza | | | |
| Source | FVCOM model | | Tide gauge station | |
| Constituents | Amplitude (m) | Phase (°) | Amplitude (m) | Phase (°) |
|---|---|---|---|---|
| $M_2$ | $0.589 \pm 0.004$ | $277.4 \pm 0.5$ | $0.646 \pm 0.011$ | $277.0 \pm 0.9$ |
| $S_2$ | $0.375 \pm 0.005$ | $326.8 \pm 0.7$ | $0.365 \pm 0.010$ | $324.0 \pm 1.9$ |
| $K_1$ | $0.384 \pm 0.005$ | $59.5 \pm 0.8$ | $0.501 \pm 0.012$ | $67.1 \pm 1.4$ |
| $O_1$ | $0.352 \pm 0.005$ | $36.0 \pm 0.9$ | $0.453 \pm 0.013$ | $35.9 \pm 1.7$ |
| F | 0.76 | | 0.94 | |
| $2(M_2+S_2)$ | 1.93 m | | 2.02 m | |

Table 4.4: Tidal harmonic constants for Dallmann (Schöne et al., 1998) and Esperanza (D'Onofrio et al., 2003)

| Stations Constituents | Dallmann[1] | | Esperanza[2] | |
|---|---|---|---|---|
| | Amplitude (m) | Phase (°) | Amplitude (m) | Phase (°) |
| $M_2$ | 0.463 | 278.6 | 0.627 | 274.5 |
| $S_2$ | 0.251 | 330.9 | 0.397 | 311.7 |
| $K_1$ | 0.285 | 60.1 | 0.364 | 53.1 |
| $O_1$ | 0.298 | 44.8 | 0.403 | 34.9 |
| F | 0.82 | | 0.75 | |

[1] based on tide gauge record: March - December 1997 (Schöne et al., 1998).
[2] based on tide gauge record: January 1971 - July 1972 (D'Onofrio et al., 2003).

### 4.2.3 Tidal propagation and amplification

Amplitude and phase of tidal constituents were further computed from the modelled tidal elevations for all the nodes in the model. Based on the calculated harmonic constants, cotidal (or co-phase) and corange (or co-amplitude) charts of the four major tidal constituents in the entire model domain were constructed (Figs. 4.4-4.5). Figs. 4.6-4.7 show the detailed cotidal and corange charts for the Bransfield Strait region.

From the $M_2$ cotidal lines, as presented in Fig. 4.4a, it was observed that the $M_2$ wave coming from the northwestern boundary of the model domain enters the continental shelf towards the northwestern Antarctic Peninsula. From the southeastern boundary, the $M_2$ wave propagates from the Weddell Sea, turns around the northern tip of the Antarctic Peninsula before entering the Bransfield Strait. From Fig. 4.4a, it can be clearly seen that the tidal amplitudes significantly increase from about 0.2 m around the Bellingshausen Sea in the west to larger than 0.6 m around the Weddell Sea in the east. The corange lines are generally perpendicular to the peninsula except around the northeastern region of the Bransfield Strait where they are nearly parallel to the King George Island. Taking a closer look at the Bransfield Strait region, as shown in Figs. 4.6a, it is noteworthy that the $M_2$ waves, both coming from the Southern Ocean and Weddell Sea, slow down as they propagate into the Bransfield Strait where the water depths are relatively shallower. The $M_2$ wave that is coming from the northwestern direction seems to adjust itself to the seafloor topography through a refraction process before it meets the diffracted wave from the Weddell Sea in the middle of the central basin. They subsequently travel towards the western coast of the Northern Antarctic Peninsula.

In general, the $S_2$ constituent (Figs. 4.4b and 4.6b) has similar amplification pattern with the $M_2$ constituent, i.e. a progressive eastward increase in amplitude, although the amplitudes are smaller. The cotidal lines are approximately orthogonal to the coast. The $S_2$ wave travels from the Weddell Sea, turns into the Bransfield Strait and propagates further southwestward. Similar to the semi-diurnal constituents, the $K_1$ and $O_1$ tidal waves propagate from the Weddell Sea and turn
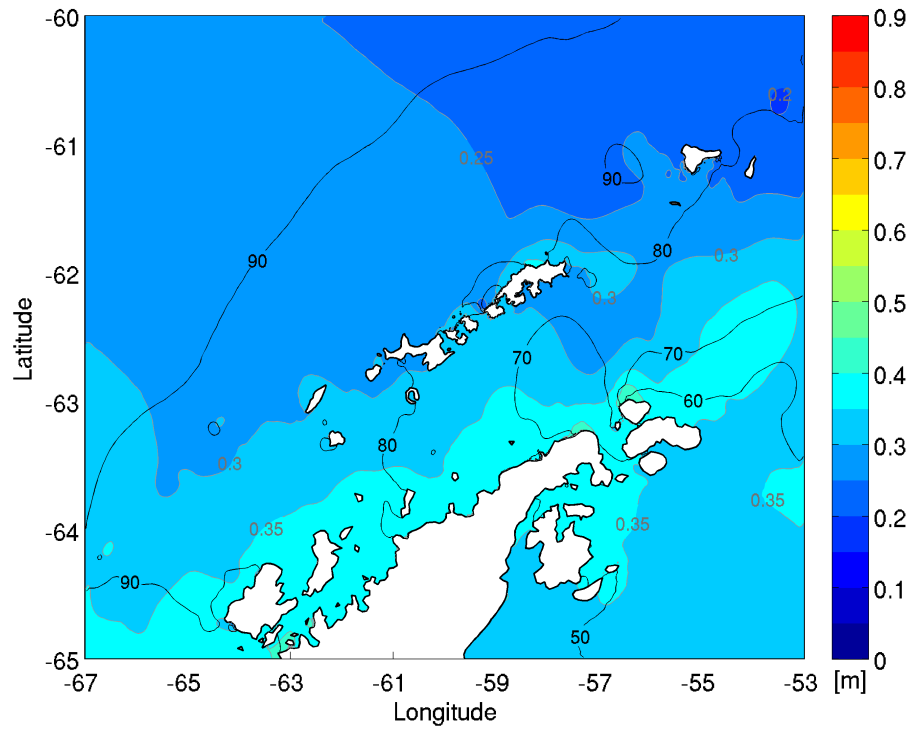
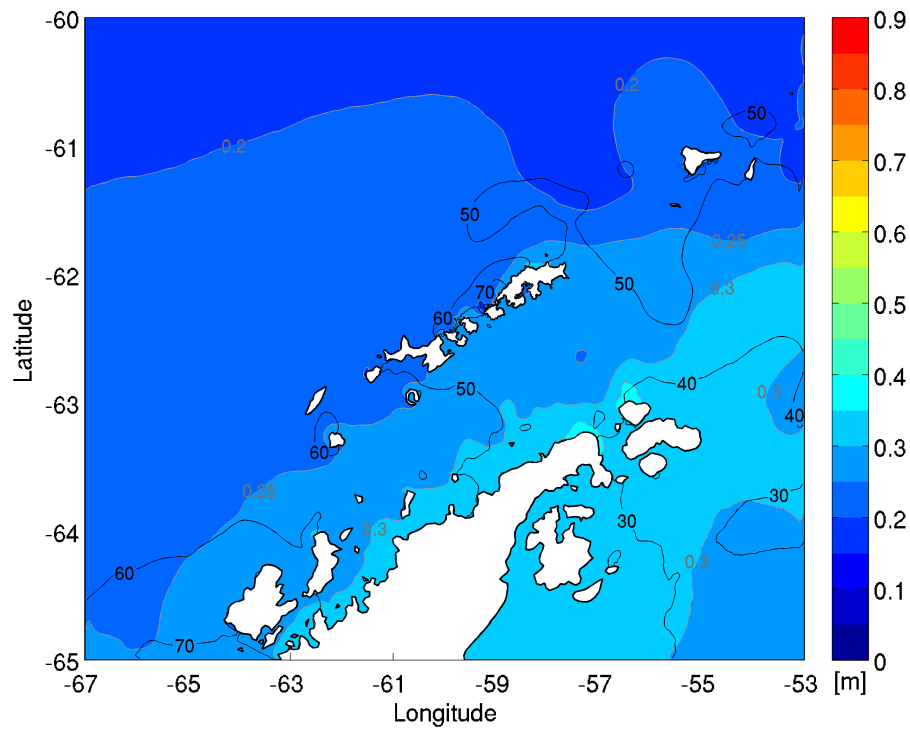43
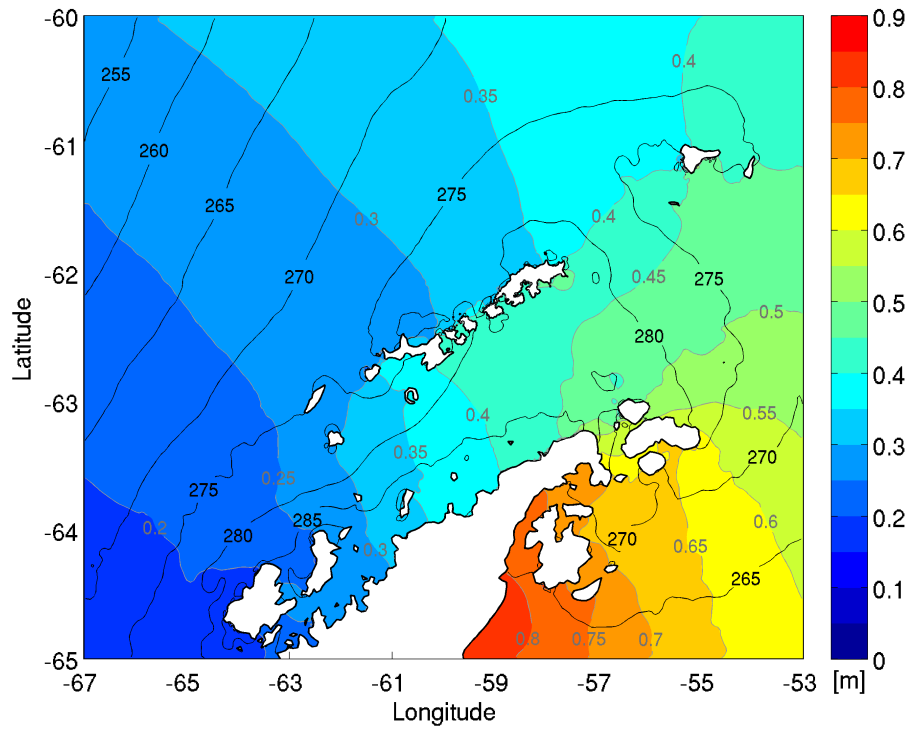
(a) M$_2$ tidal constituent
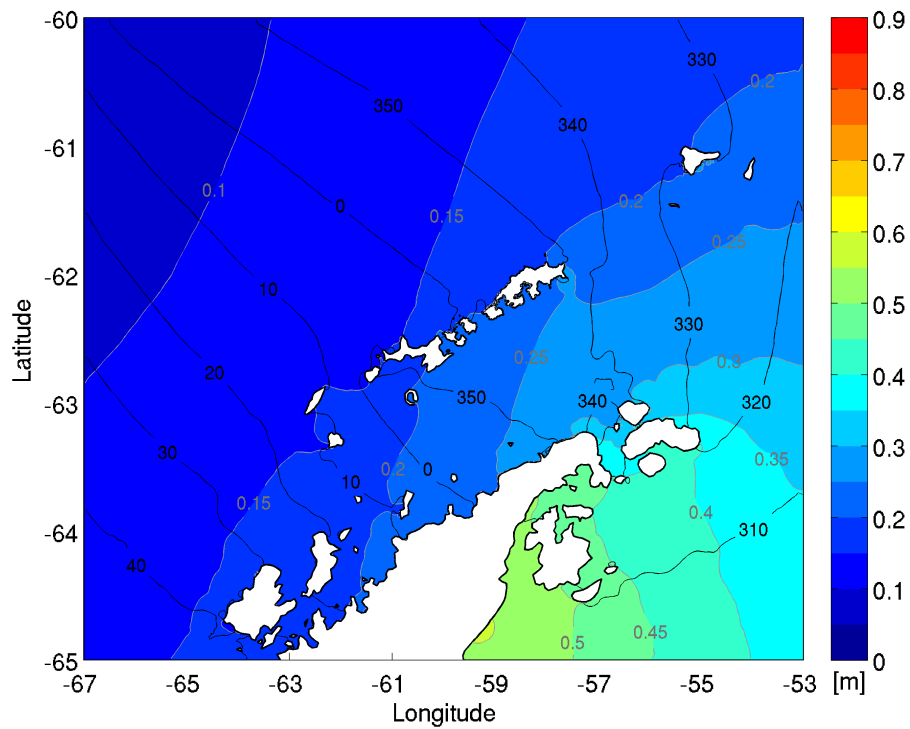


(b) S$_2$ tidal constituent

Figure 4.4: The tidal amplitudes and phases of the (a) M$_2$ and (b) S$_2$ constituents, for the Northern Antarctic Peninsula region. The amplitude is indicated by the colour scale and the phase by the black contour lines.
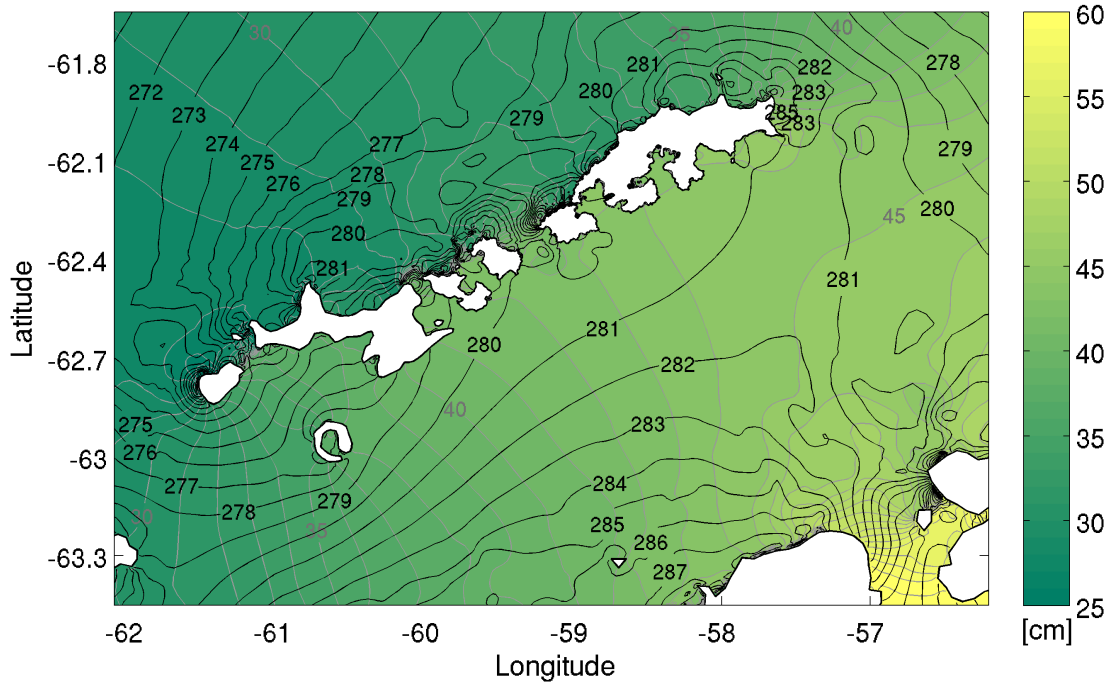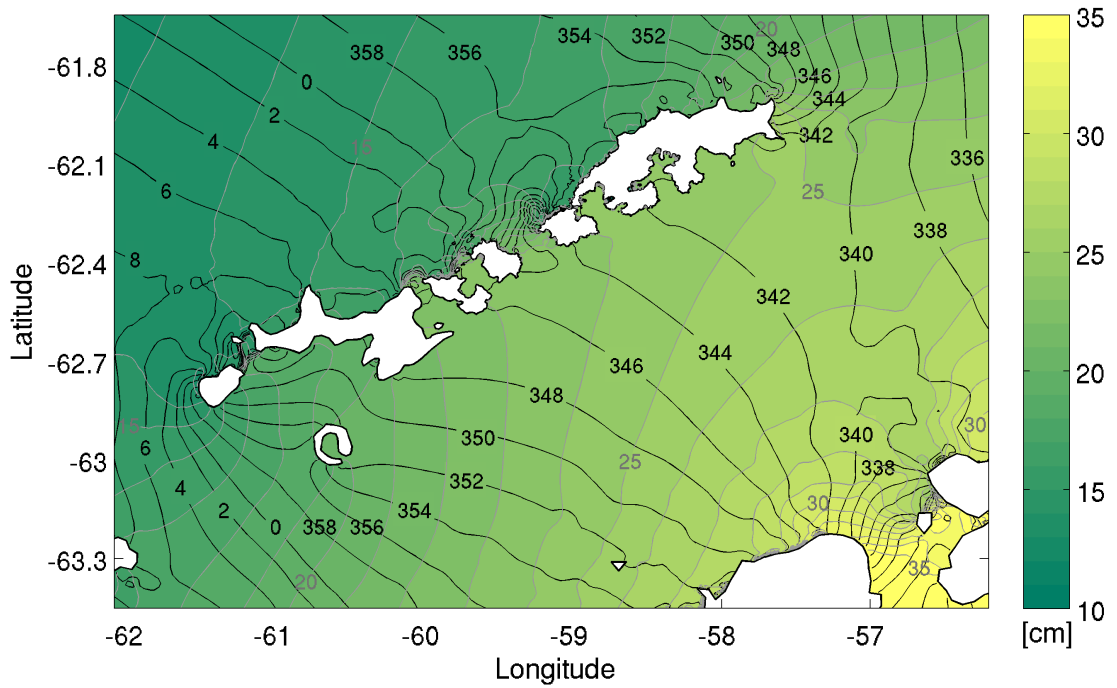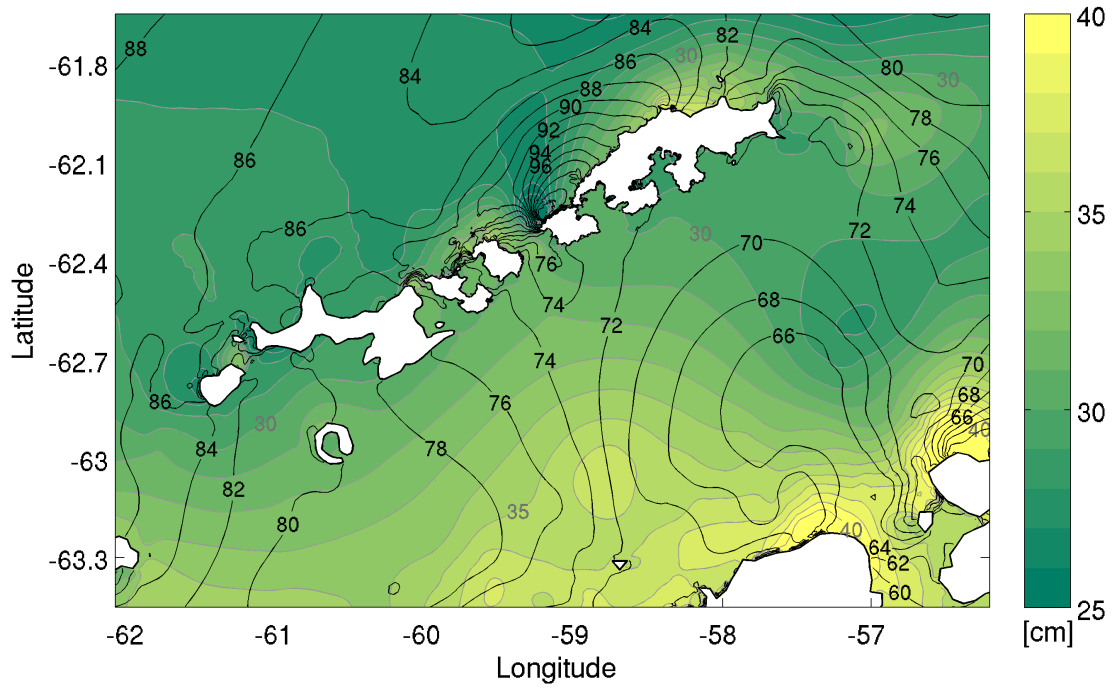
(a) $K_1$ tidal constituent



(b) $O_1$ tidal constituent
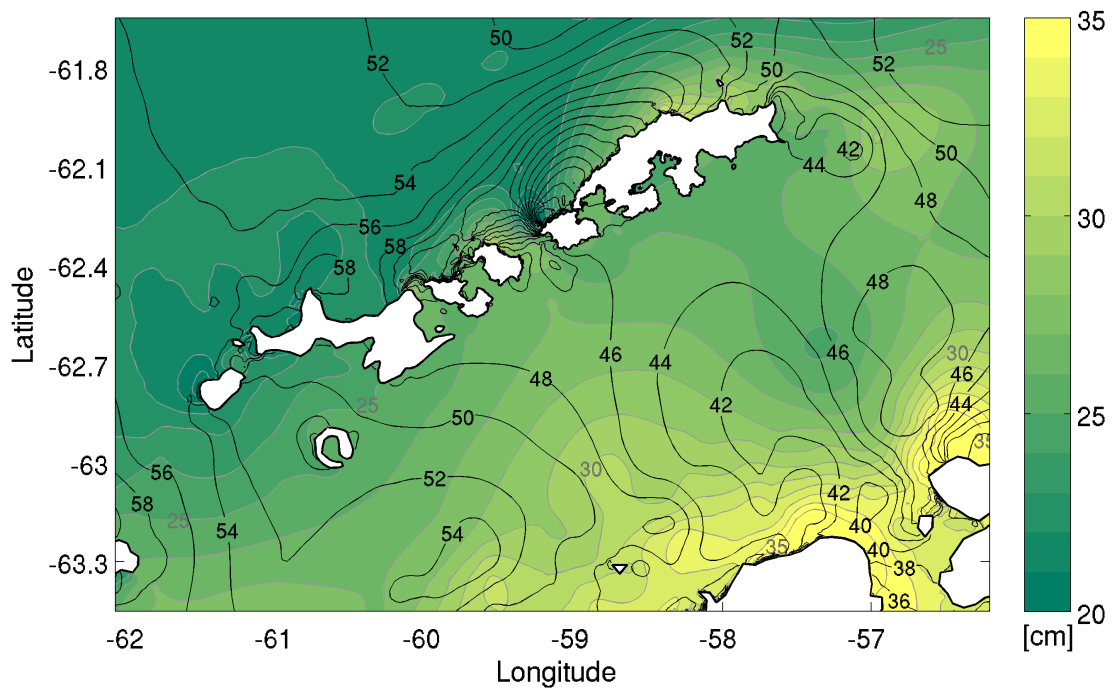
Figure 4.5: The tidal amplitudes and phases of the (a) $K_1$ and (b) $O_1$ constituents, for the Northern Antarctic Peninsula region. The amplitude is indicated by the colour scale and the phase by the black contour lines.

(a) $M_2$ tidal constituent



(b) $S_2$ tidal constituent

Figure 4.6: The tidal amplitudes and phases of the (a) $M_2$ and (b) $S_2$ constituents, for the Brans-field Strait region. The amplitude is indicated by the individual colour scale and the phase by the black contour lines.

(a) K$_1$ tidal constituent



(b) O$_1$ tidal constituent

Figure 4.7: The tidal amplitudes and phases of the (a) K$_1$ and (b) O$_1$ constituents, for the Brans-field Strait region. The amplitude is indicated by the individual colour scale and the phase by the black contour lines.

into the Bransfield Strait before they travel further towards the Bellingshausen Sea (Figs. 4.5 and 4.7). The corange lines show that the amplitudes of the diurnal constituents generally increase from the Southern Ocean towards the Northern Antarctic Peninsula. The cotidal and corange charts for all the four principal tidal constituents are qualitatively reasonable and generally in agreement with previous results when compared to similar charts based on observations (Dragani et al., 2004) and other numerical model (Robertson et al., 1998).

## 4.3 Currents

### 4.3.1 Tide-induced currents

The local circulation in the Bransfield Strait is strongly influenced by tides. Field measurements of currents performed during the austral summer 1992/93 have revelead the relative importance of tidal currents in the Bransfield Strait (López et al., 1994). In the present study, modelled tidal currents in the proximity of Maxwell Bay opening appear to be significant and they flow predominantly northeastward following closely along the coasts as shown in Figs. 4.8 and 4.9. In each figure, two snapshots with a two-hour interval are plotted for the tidal current velocities near the water surface, at midwater and near the bottom to illustrate the temporal evolution of the current velocities.

Regardless of the depths, the tidal currents approach the mouth of Maxwell Bay from the southwestern direction and subsequently travel towards the direction of Potter Cove. Due to the restricted entrance and the presence of seafloor topography with steep slopes in front of Potter Cove, the incoming tidal currents are diverted away from entering Potter Cove. Figs. 4.8 and 4.9 respectively show that both the relatively low and high incoming tidal currents, when approaching close to the mouth of Potter Cove, are diverted eastward flowing away from Potter Cove. Part of the tidal currents enter Maxwell Bay where a cyclonic circulation can be observed. Cyclonic circulation is clockwise in the Southern Hemisphere and counterclockwise in the Northern Hemisphere. Cylonic circulation in Maxwell Bay has also been previously documented in Chang et al. (1994). While the results show that the circulation off Potter Cove is significantly driven by tides, it can be clearly seen that tides, on the contrary, have minimal influence on the circulation in Potter Cove.

To further demonstrate the relative tidal influence on the currents in Potter Cove and area outside Potter Cove, time series of near-surface and near-bottom current speeds, for example during 12-22 January 1999, are plotted for MM (near the opening of Maxwell Bay, see Figs. 4.28c and 4.28f), PM (near the opening of Potter Cove, see Figs. 4.29c and 4.29f), Dallmann (Figs. 4.30c and 4.30f) and IC (at the inner cove, see Figs. 4.31c and 4.31f). At MM near the opening of Maxwell Bay, the tide-induced currents generally vary around 10-30 cm/s, with maximum current speeds of about 50 cm/s and 45 cm/s registered for the near-surface and near-bottom current speeds, respectively. At PM, Dallmann and IC, that are located in Potter Cove, the current
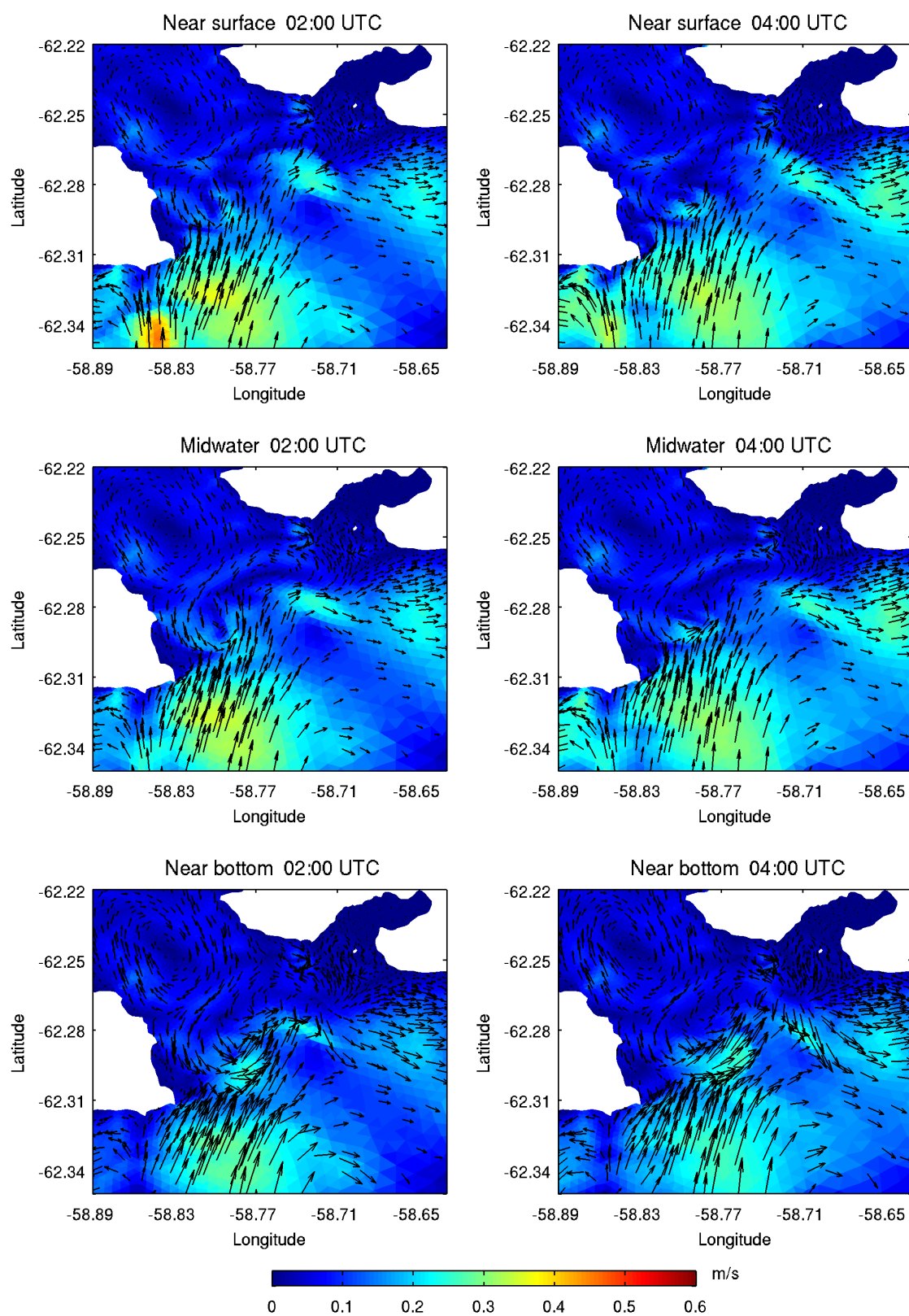
Figure 4.8: Tidal circulation patterns in front of Potter Cove with relatively low incoming current velocities on 13-Jan-1999.
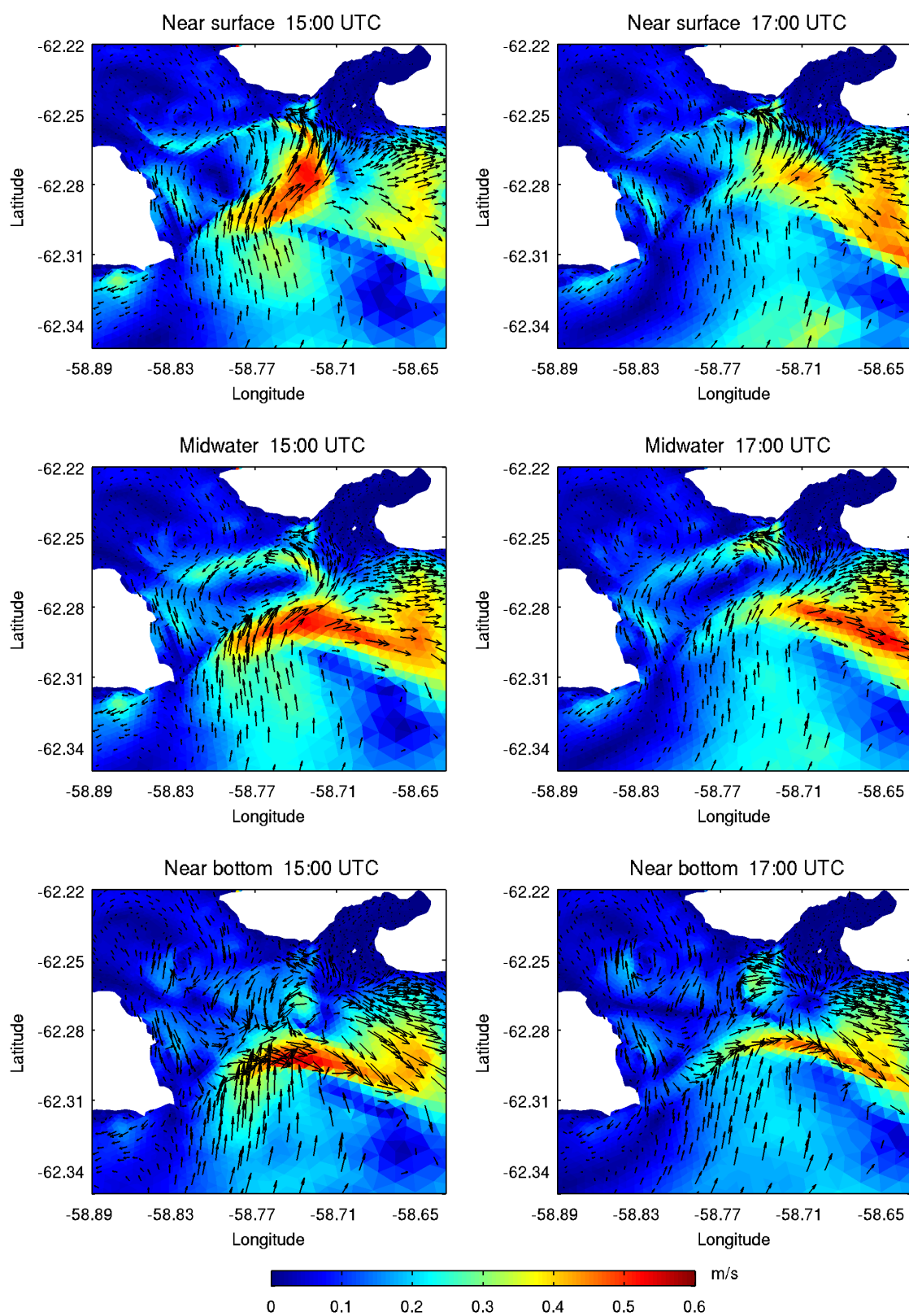
Figure 4.9: Tidal circulation patterns in front of Potter Cove with relatively high incoming current velocities on 18-Jan-1999.

speeds are generally below 6 cm/s with exceptionally low current speeds (below 2 cm/s) found occurring at IC.

In order to look into the tidal circulation patterns in Potter Cove, the distributions of the tidal velocity fields are schematically presented for ebb and flood conditions during neap and spring tides. Two typical flow fields during ebb condition (neap tide) are given in Fig. 4.10 for near-surface flow and Fig. 4.11 for near-bottom flow. Both the near-surface and near-bottom flow circulations in Potter Cove show similar patterns. During the ebb, the currents exit the cove (Figs. 4.10a and 4.11a). The outflow can be better visualized as normal flow through various vertical transects along Potter Cove as shown in Fig. 4.12 (left panels). See inset for transects A-B, C-D and E-F. Negative velocities indicate outflow. The flow fields around the opening of Potter Cove is also directly affected by the surrounding external waters (Figs. 4.10 and 4.11).

As the tidal currents become slower, the flow fields in Potter Cove change and develop a general cyclonic circulation pattern where the currents enter and flow along the northern part of the cove and exit from the southern region (Figs. 4.10b and 4.11b). Such cylconic circulation can often be noted during low tidal current condition. A plot of near-surface velocity vectors (arrows) together with the bathymetric depths (colour background), as shown in Fig. 4.13, exhibits that the tidal circulation follows the meanders of the seafloor topography. Cyclonic (clockwise-rotating) gyres (or eddies) are found swirling around their centers in the cove. This feature, which is rather transient, is clearly evident from the modelled results, especially at the inner cove and the location in front of the Carlini Station, i.e. the western side of the submarine sill. Fig. 4.12 (right panels) shows the vertical distributions of the flows across the three transects. Positive velocities indicate inflow and vice versa.

Two common flow fields during flood condition (neap tide) are shown in Fig. 4.14 for the near-surface flow. The near-bottom flow fields, not shown here, have similar pattern as the near-surface flow circulation. During the flood, the currents enter the cove (Fig. 4.14a). The inflow across the transects A-B and C-D are illustrated in Fig. 4.15 (left panels). Around the mouth of Potter Cove, where the flow fields are also steered by the external waters, inflows and outflows can be observed along the transect E-F. Again, as the tidal currents become weaker, the flow fields are circulated cyclonically around Potter Cove and are steered by the seafloor topography (Fig. 4.14b) and the vertical distributions of the flows across the three transects are depicted in Fig. 4.15 (right panels). Similar to the ebb, several gyres exist at a number of locations within and near the mouth of the cove during flood condition (Fig. 4.14).

During spring tide, the circulations in Potter Cove during the ebb (Figs. 4.16 and 4.17) present analogous patterns and vertical distributions as the ones during neap tide. The flows during the flood (Figs. 4.18 and 4.19) also appear to have similar patterns and vertical flow structures to the ones during neap tide. However, the velocities near the mouth of Potter Cove do not show any consistent patterns between spring and neap as a result of the constant influence of the external waters. The results also show that the tidal currents during spring tide are relatively stronger than
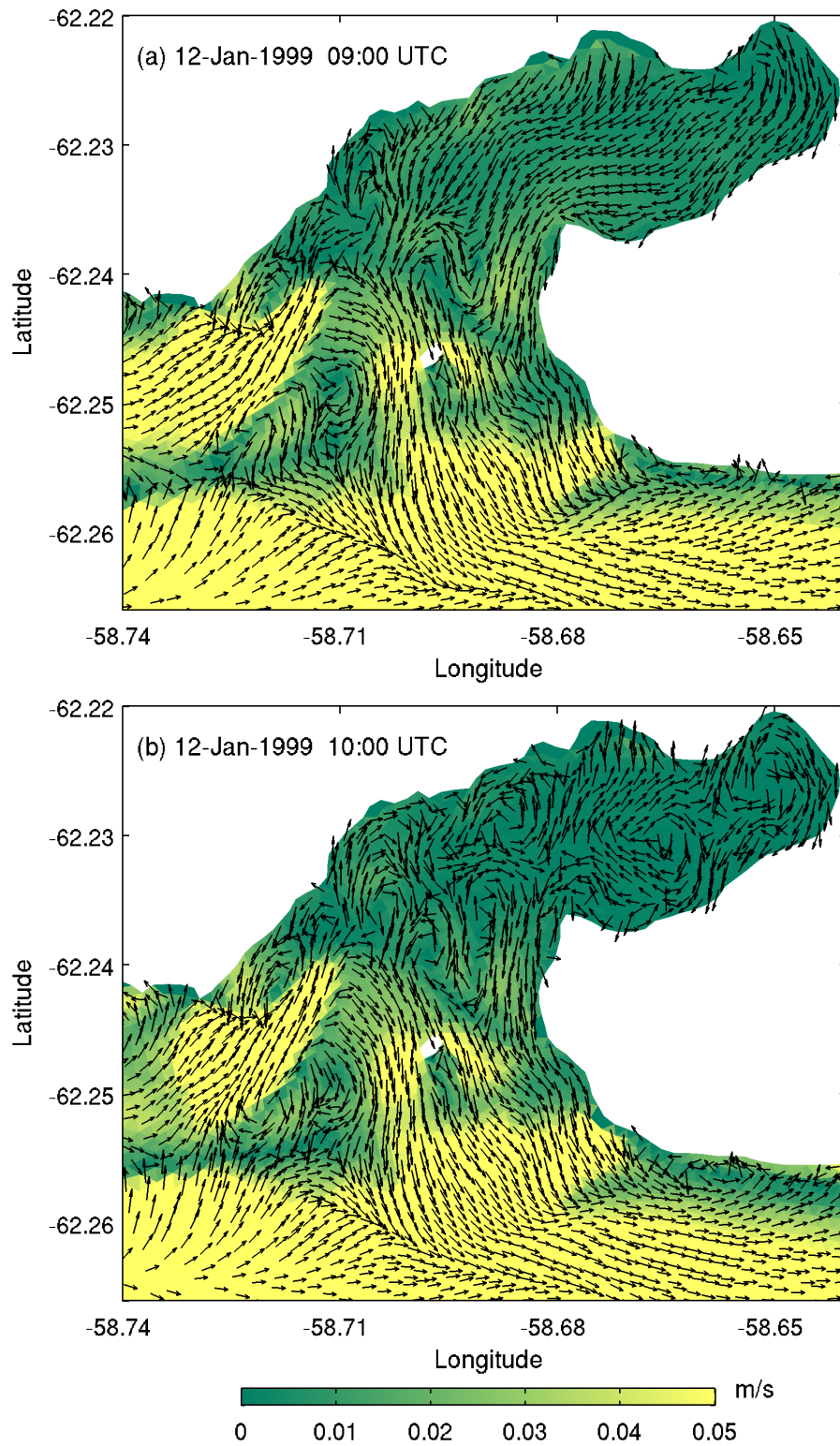
Figure 4.10: Near-surface tidal circulation patterns in Potter Cove during neap tide (ebb condition) on 12-Jan-1999.
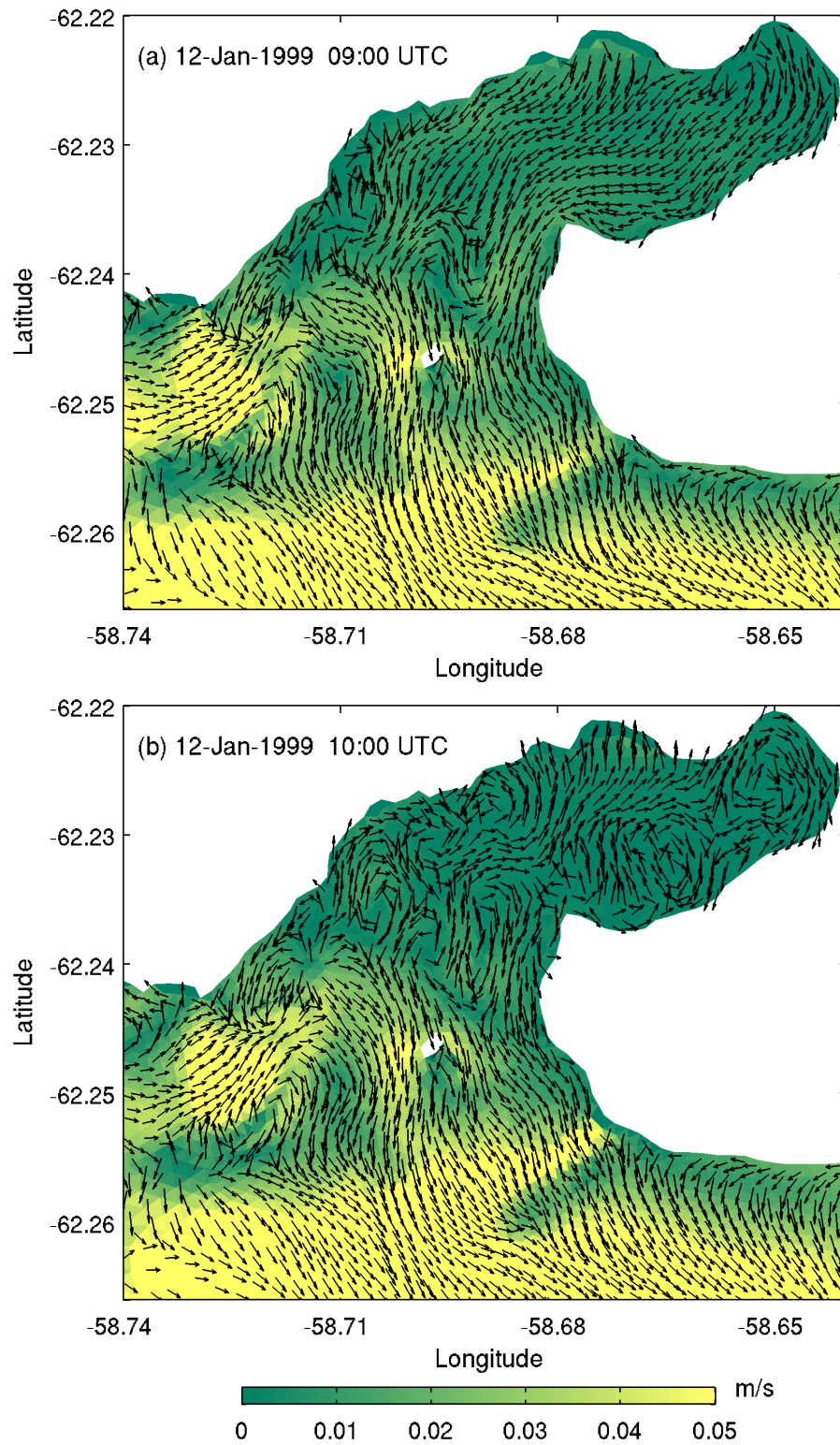
Figure 4.11: Near-bottom tidal circulation patterns in Potter Cove during neap tide (ebb condition) on 12-Jan-1999.
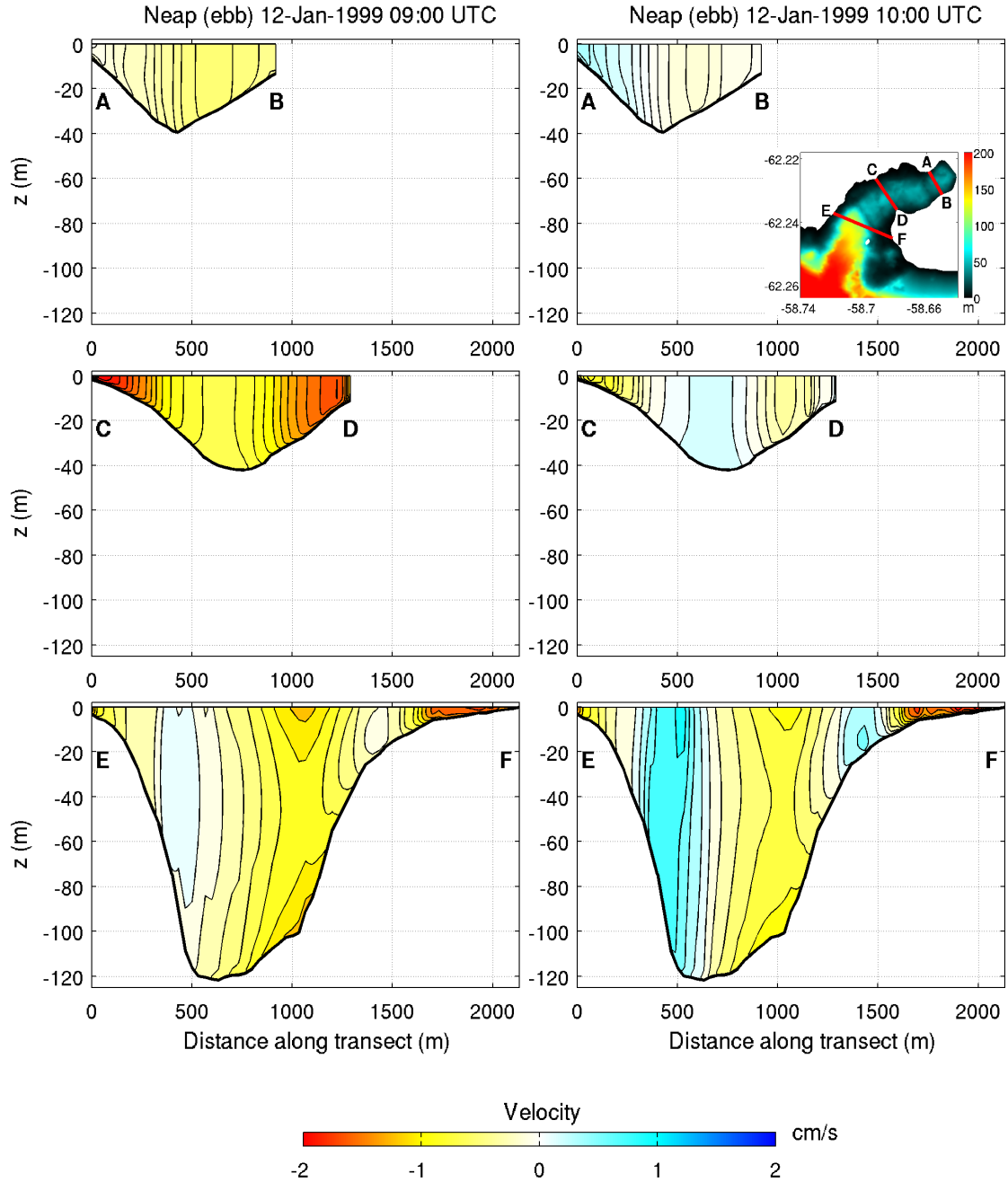
Figure 4.12: Tide-induced normal flows (in cm/s) through the transects (see inset with bathymetric depths), during neap tide (ebb condition) on 12-Jan-1999 at 09:00 UTC and 10:00 UTC. Positive velocities indicate inflow and negative velocities indicate outflow.
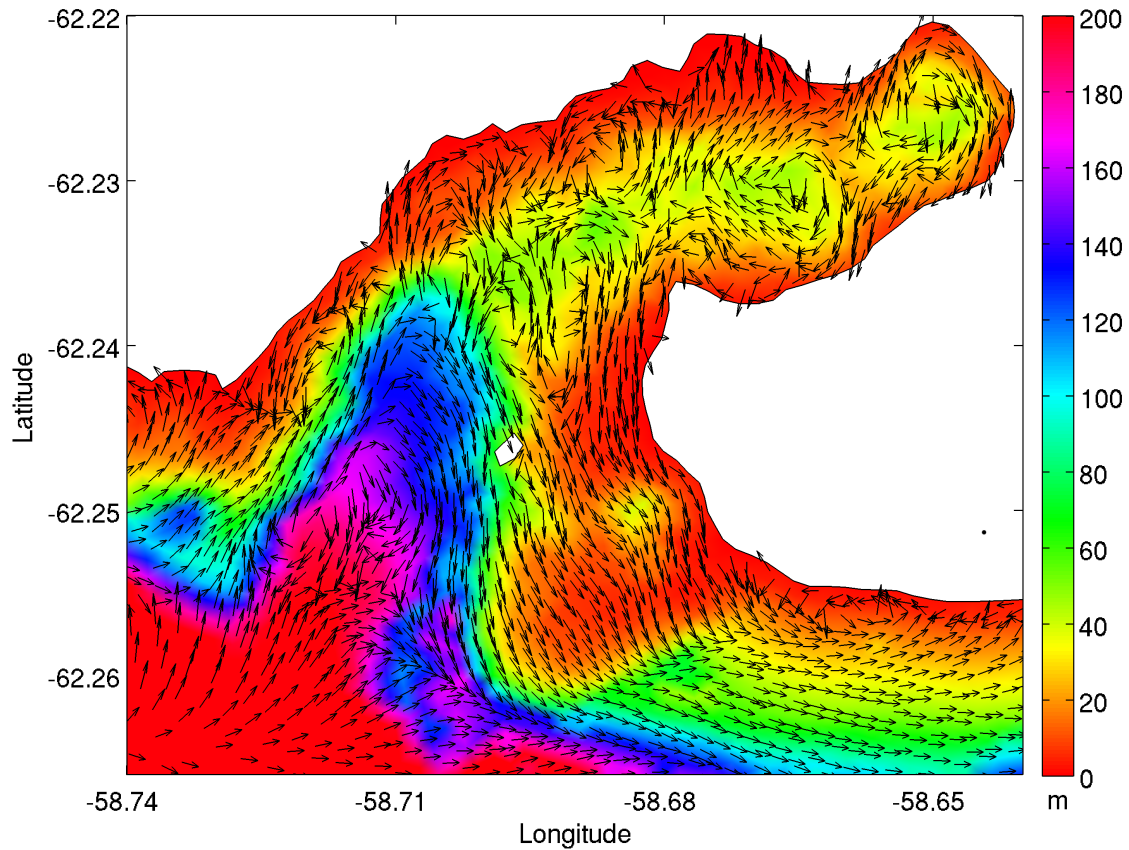
Figure 4.13: Near-surface tidal circulation fields following the seafloor topography in Potter Cove during neap tide (ebb condition) on 12-Jan-1999 at 10:00 UTC. The colour background shows the bathymetric depths in meter.

the ones during neap tide. This can also be evident from the time series of the current speeds at Dallmann (Figs. 4.30c and 4.30f) and IC (Figs. 4.31c and 4.31f) within the cove.

The modelled results revealed that the tide-induced currents in Potter Cove are generally low and independent of depths. The current regime is complex with occasional cyclonic circulation during relatively low current condition where waters entering the northern sector and exiting through the southern sector. In addition, gyres exist at a number of locations within and near the mouth of the cove.

## 4.3.2  Tide- and wind-induced currents

In a previous study, Klöser et al. (1994) reported that the surface circulation in Potter Cove is dictated by winds where westerly winds generate a cyclonic circulation with an enhanced inflow into the cove and a slackening outflow. Roese and Drabble (1998) performed direct current measurements at the inner sector of Potter Cove during the austral summer of 1992 and the austral winter of 1994. They reported that the wind-driven circulation pattern in Potter Cove is highly depen-
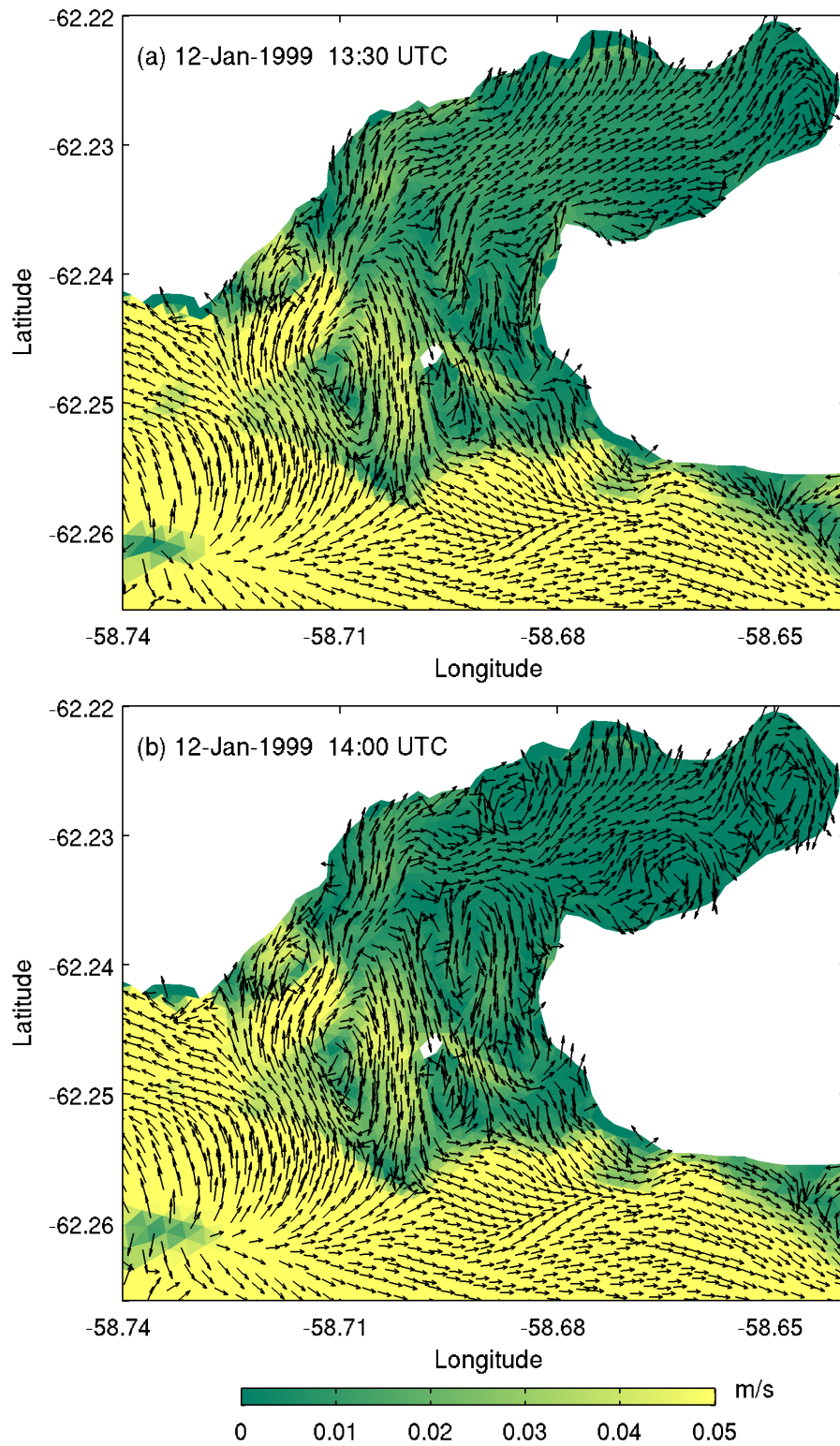
Figure 4.14: Near-surface tidal circulation patterns in Potter Cove during neap tide (flood condition) on 12-Jan-1999.
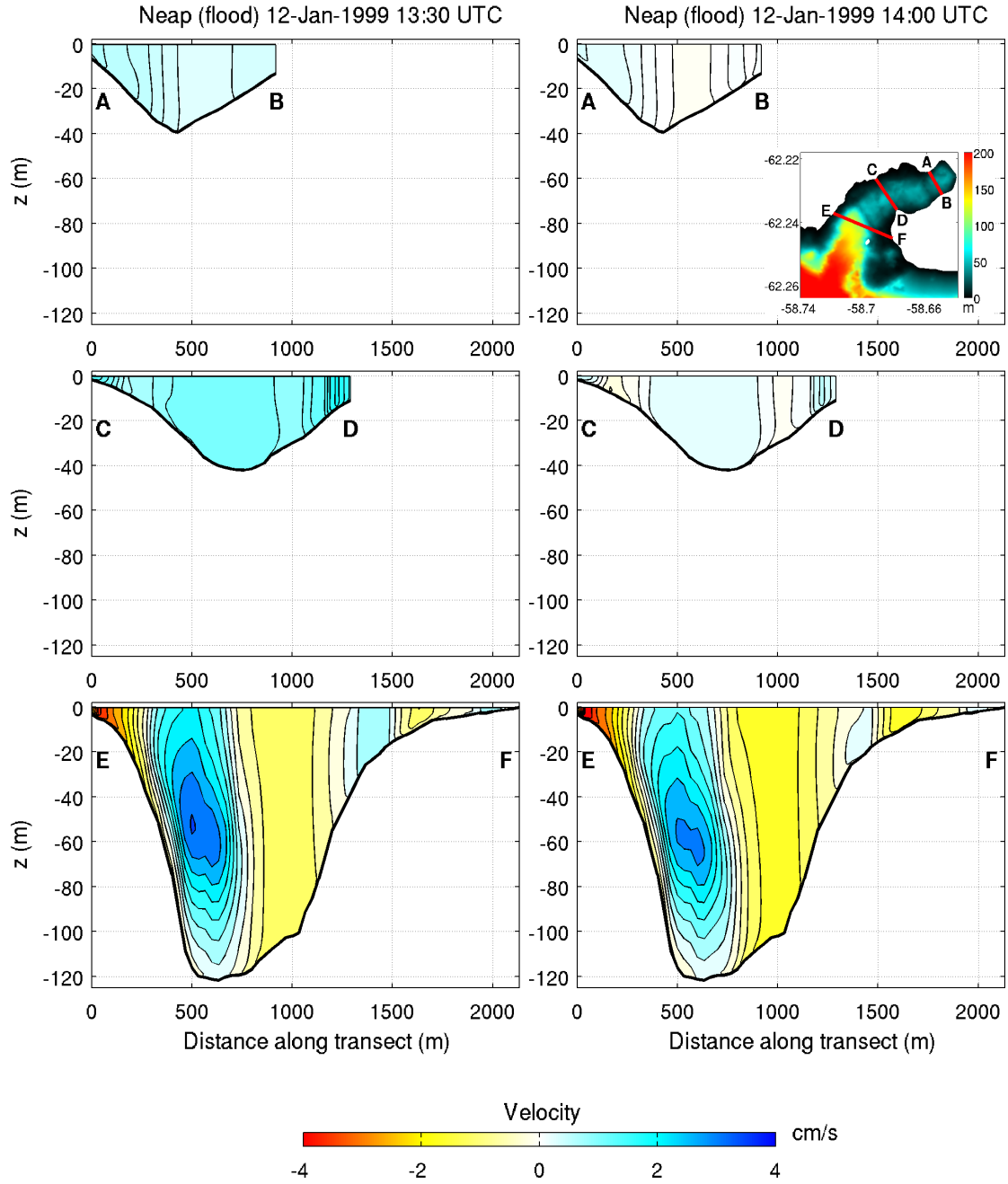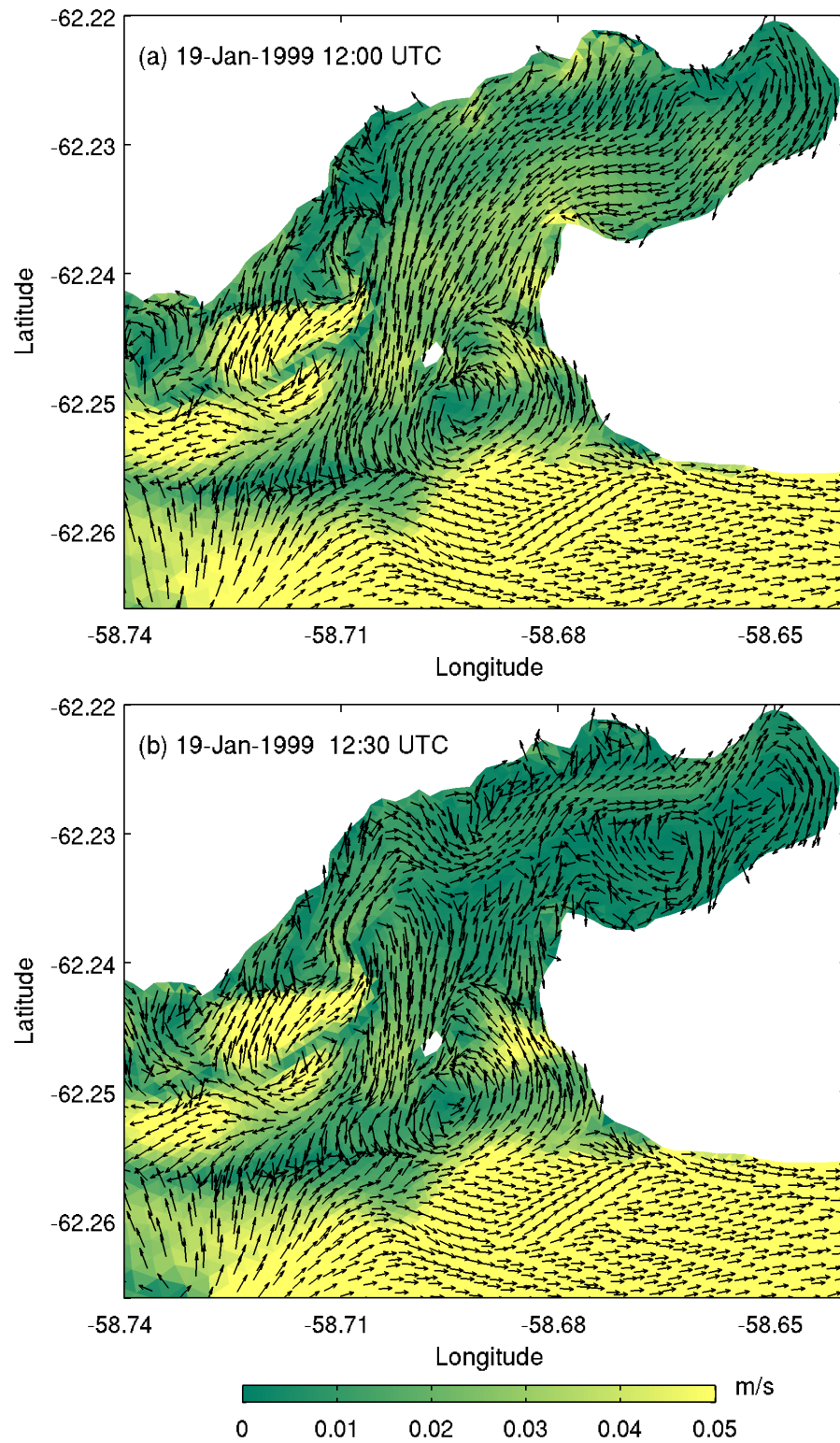
Figure 4.15: Tide-induced normal flows (in cm/s) through the transects (see inset with bathymetric depths), during neap tide (flood condition) on 12-Jan-1999 at 13:30 UTC and 14:00 UTC. Positive velocities indicate inflow and negative velocities indicate outflow.

Figure 4.16: Near-surface tidal circulation patterns in Potter Cove during spring tide (ebb condition) on 19-Jan-1999.
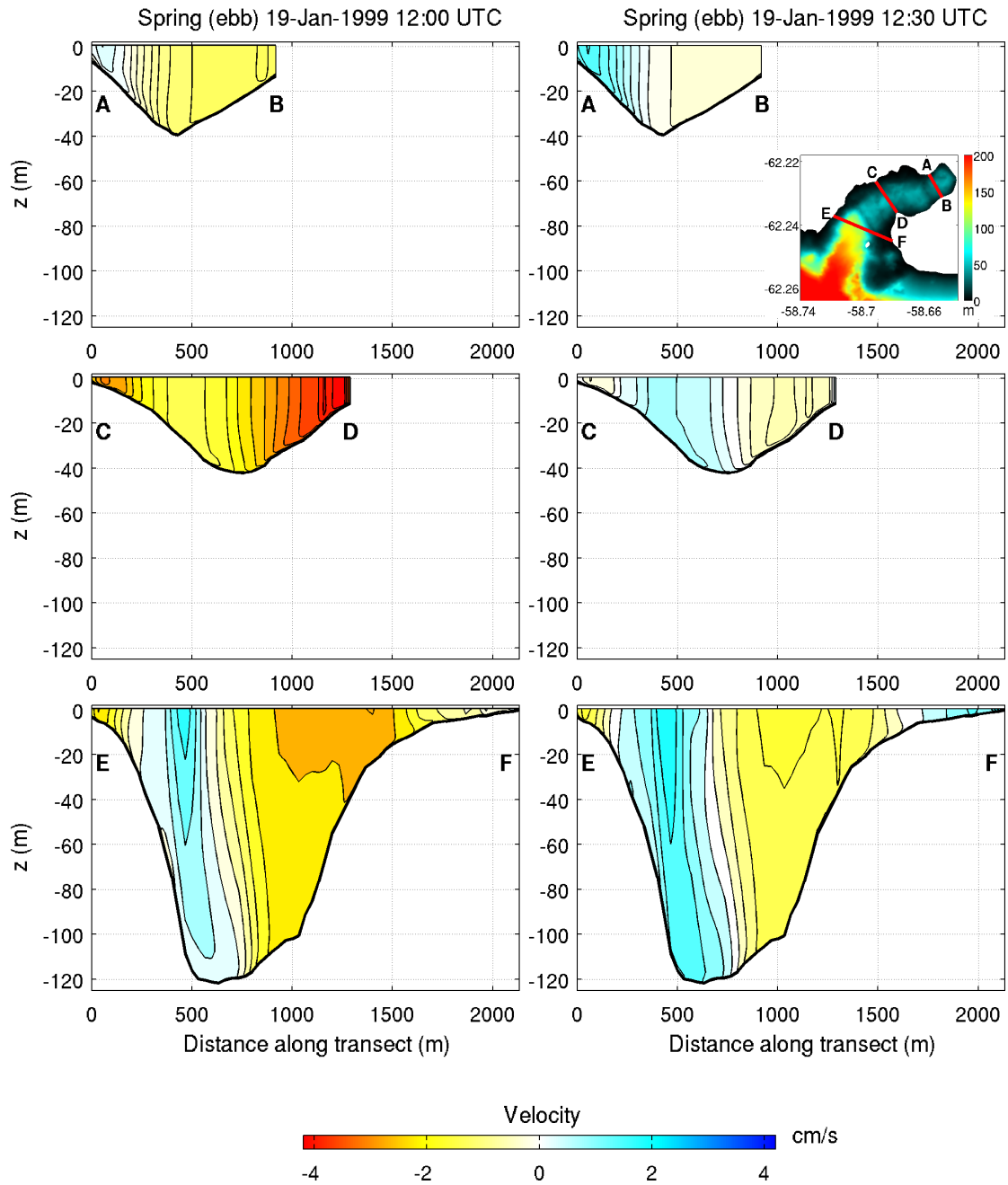
Figure 4.17: Tide-induced normal flows (in cm/s) through the transects (see inset with bathymetric depths), during spring tide (ebb condition) on 19-Jan-1999 at 12:00 UTC and 12:30 UTC. Positive velocities indicate inflow and negative velocities indicate outflow.
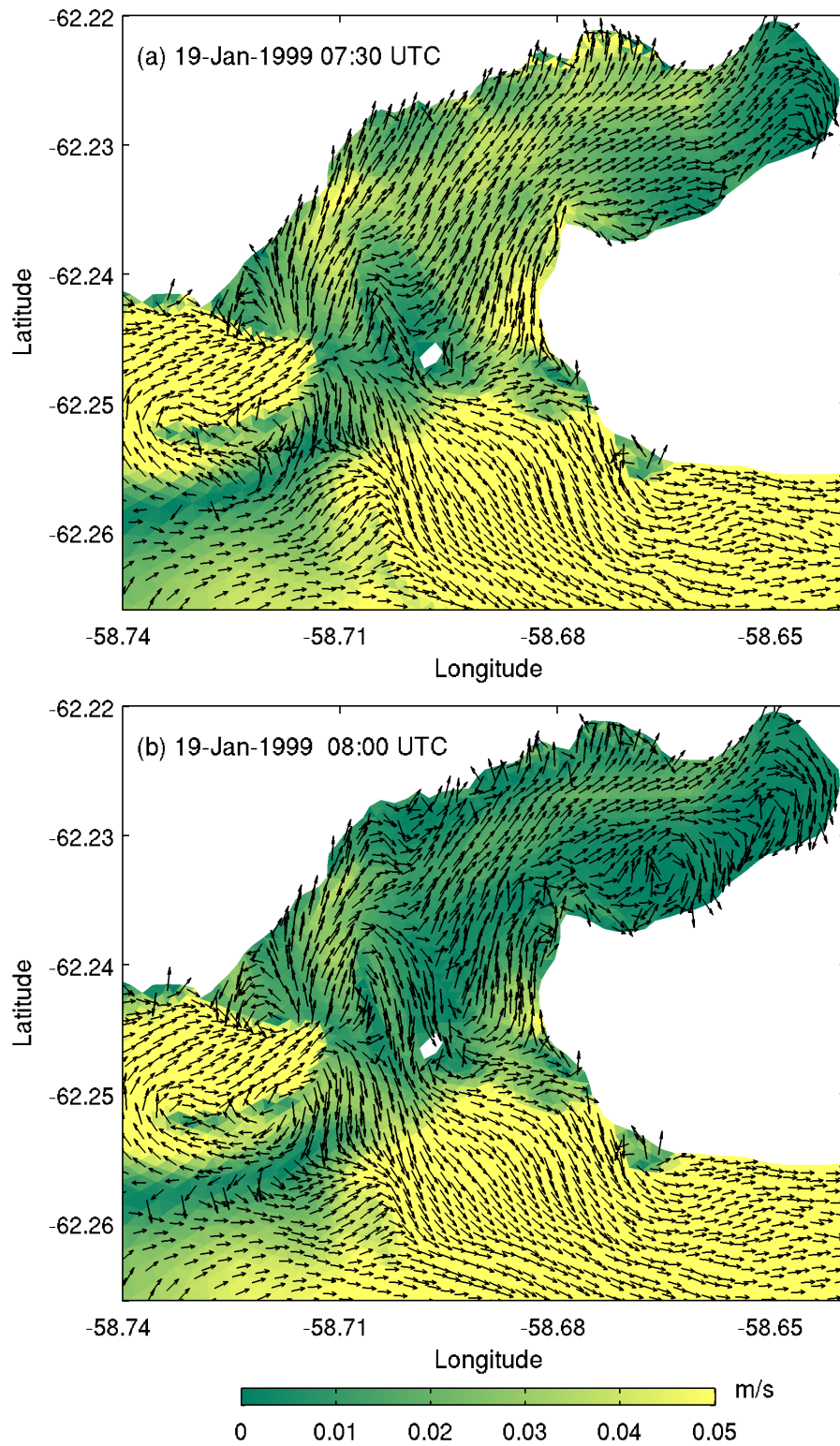
Figure 4.18: Near-surface tidal circulation patterns in Potter Cove during spring tide (flood condition) on 19-Jan-1999.
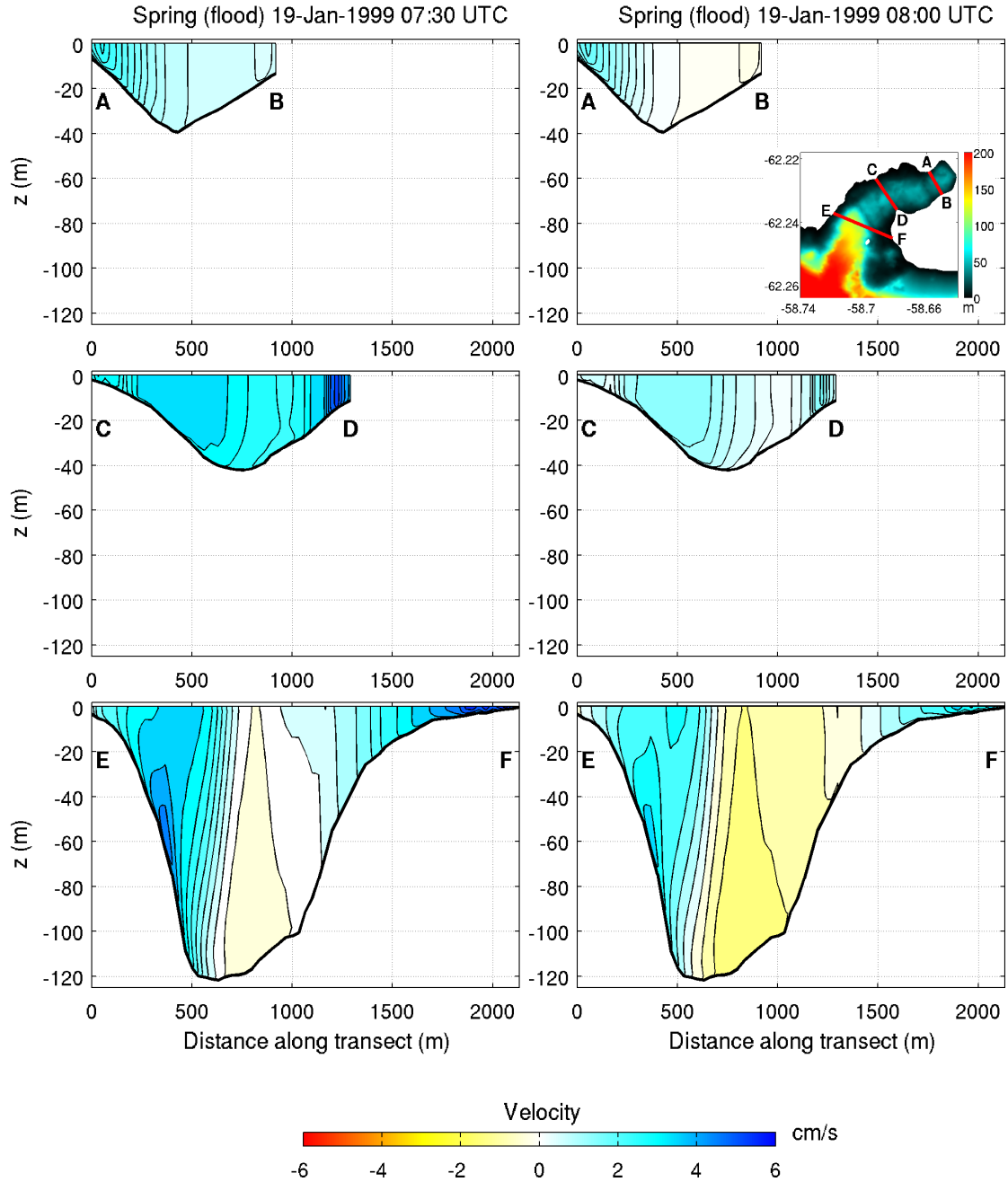
Figure 4.19: Tide-induced normal flows (in cm/s) through the transects (see inset with bathymetric depths), during spring tide (flood condition) on 19-Jan-1999 at 07:30 UTC and 08:00 UTC. Positive velocities indicate inflow and negative velocities indicate outflow.

dent on the wind intensity. The observed current velocities were reported to be relatively low with mean velocities up to 3.5 cm/s and maximum velocities up to 20 cm/s during their measurement period.

The wind-induced circulation pattern in Potter Cove depends on the constantly changing wind speed and direction. In the presence of winds, the current circulations in Potter Cove become complex. When wind is added into the morphologically complex cove system, this external physical forcing causes the flows to circulate in different directions at different depths. In order to correspond with the wind events reported in Chapter 3, the flow patterns corresponding to various wind conditions in Potter Cove will be discussed. The terms 'light', 'moderate' and 'strong' are used to describe the various wind conditions.

During the wind episodes, winds were blowing from the SW-NW quadrant, as indicated by the arrows in Figs. 4.20, 4.22, 4.24 and 4.26. The left, middle and right panels in these figures show the respective flow fields (near-surface, midwater and near-bottom) that are subject to various forcings, i.e. tide only (left panels), wind only (middle panels) and combined effects of tide and wind (right panels). Figs. 4.21, 4.23, 4.25 and 4.27 show the corresponding normal flows through the vertical transects A-B, C-D and E-F. From Figs. 4.20-4.27, the comparisons between the tidal-driven circulations (left panels) and wind-driven circulations (middle panels) show that wind plays a more significant role in the circulation patterns in Potter Cove. This is clearly evident when the combined tidal and wind driven velocities (right panels) agree with the wind-driven velocities. The wind component generally strengthens the surface flow. The velocities near the bottom (for wind and tide+wind cases) are relatively smaller. This could be attributable to the bottom friction and the weakening effect of wind at deeper depths.

Fig. 4.20 shows that the northwesterly light wind of 5.5 m/s drives surface water into the cove where surface outflow is hindered. The incoming waters travel along the northern and southern coasts and the inflow at the central region is confined to a thin surface layer as shown in Fig. 4.21 (see transects A-B and C-D). Inhibited by the surface inflow, the water leaves the cove from the bottom along the central region. The flow fields near the mouth of Potter Cove are influenced by the external waters where tidal-driven currents can be dominant, therefore the circulation pattern near the mouth depends on the intensity of the tides, winds, or combined effects of both. As the wind speed increases, the increased current velocities in Potter Cove slightly alter the flow patterns (Figs. 4.22-4.23). A cyclonic gyre can be found swirling at the inner cove (Fig. 4.22). The incoming waters generally move along the northern and southern coasts and the outflow exits the cove by the central region (see transects A-B and C-D in Fig. 4.23).

In general, the southwesterly winds in combination with the tides generate cyclonic circulation where the waters enter the cove through the northern sector and exit through the southern sector (Figs. 4.24-4.27). A cyclonic circulation in Potter Cove has been previously reported in the literatures (Schloss et al., 2002, 1997; Vodopivez et al., 2001). The circulation pattern seems to be following the meanders of the bathymetry. From Figs. 4.24 and 4.26, a gyre is notable in the inner
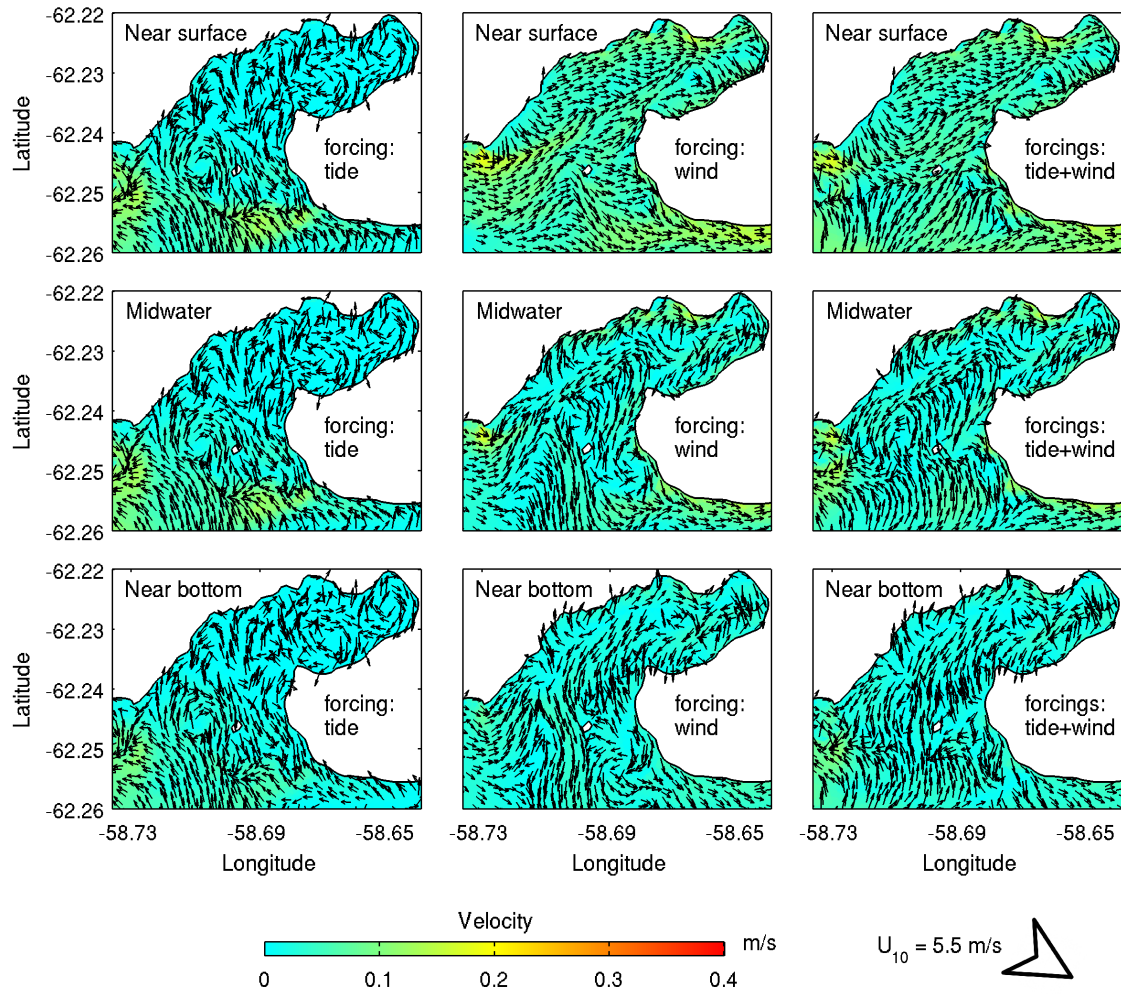
Figure 4.20: Near-surface, midwater and near-bottom circulation patterns with respect to different forcings in Potter Cove on 13-Jan-1999 (light wind condition). Wind speed $U_{10}$ and direction (arrow) are indicated in the lower right corner.
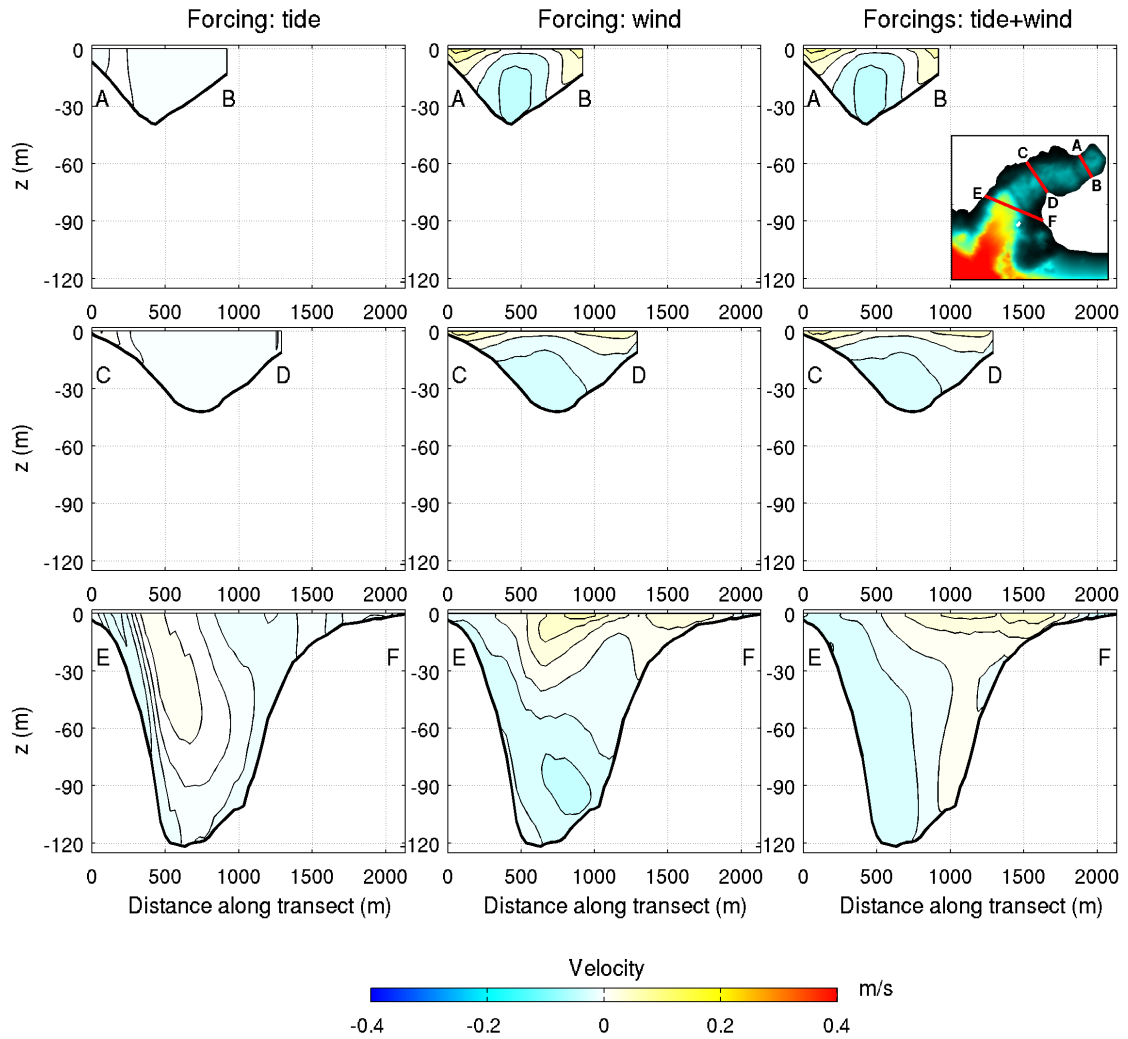
Figure 4.21: Normal flows (in m/s) through the transects (see inset) with respect to different forcings in Potter Cove on 13-Jan-1999 (light wind condition). Positive velocities indicate inflow and negative velocities indicate outflow.
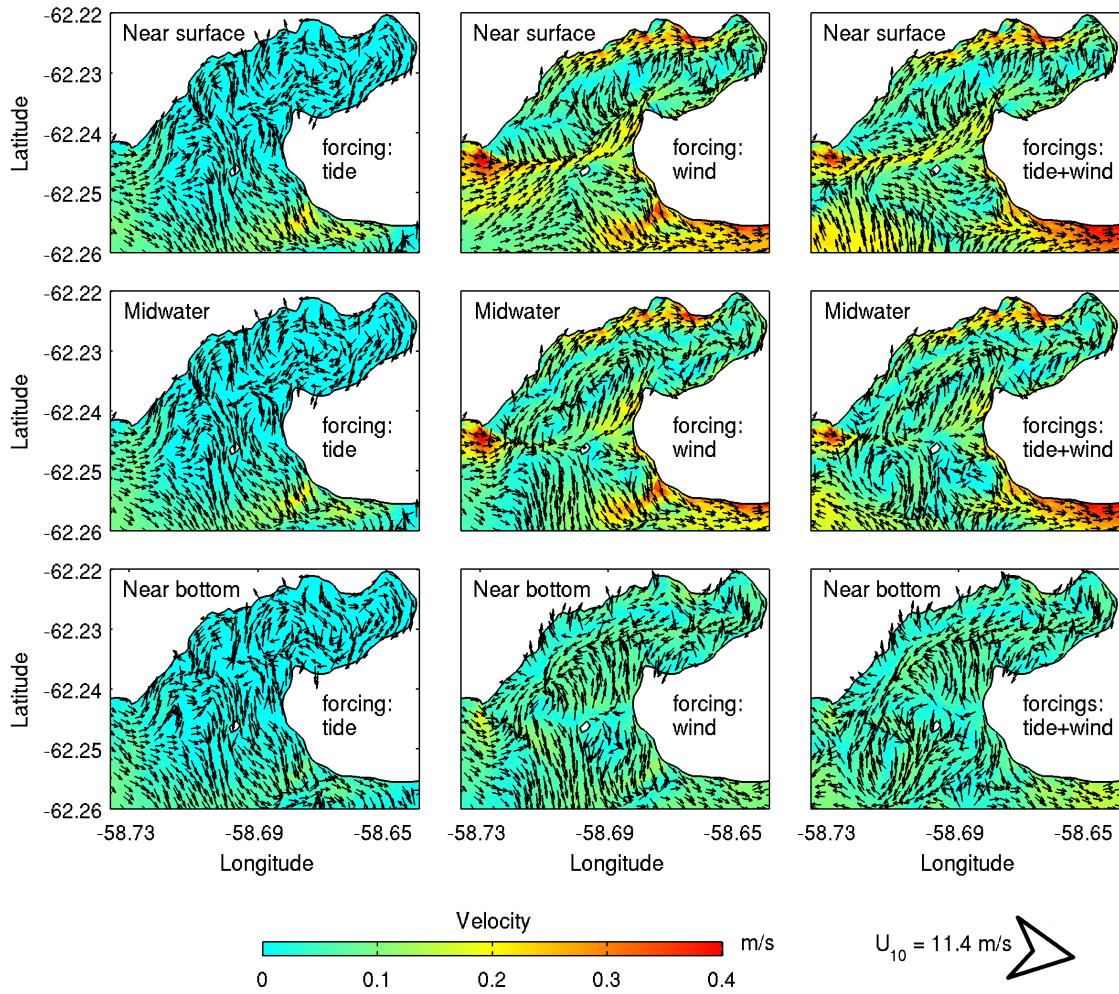
Figure 4.22: Near-surface, midwater and near-bottom circulation patterns with respect to different forcings in Potter Cove on 15-Jan-1999 (strong wind condition). Wind speed $U_{10}$ and direction (arrow) are indicated in the lower right corner.
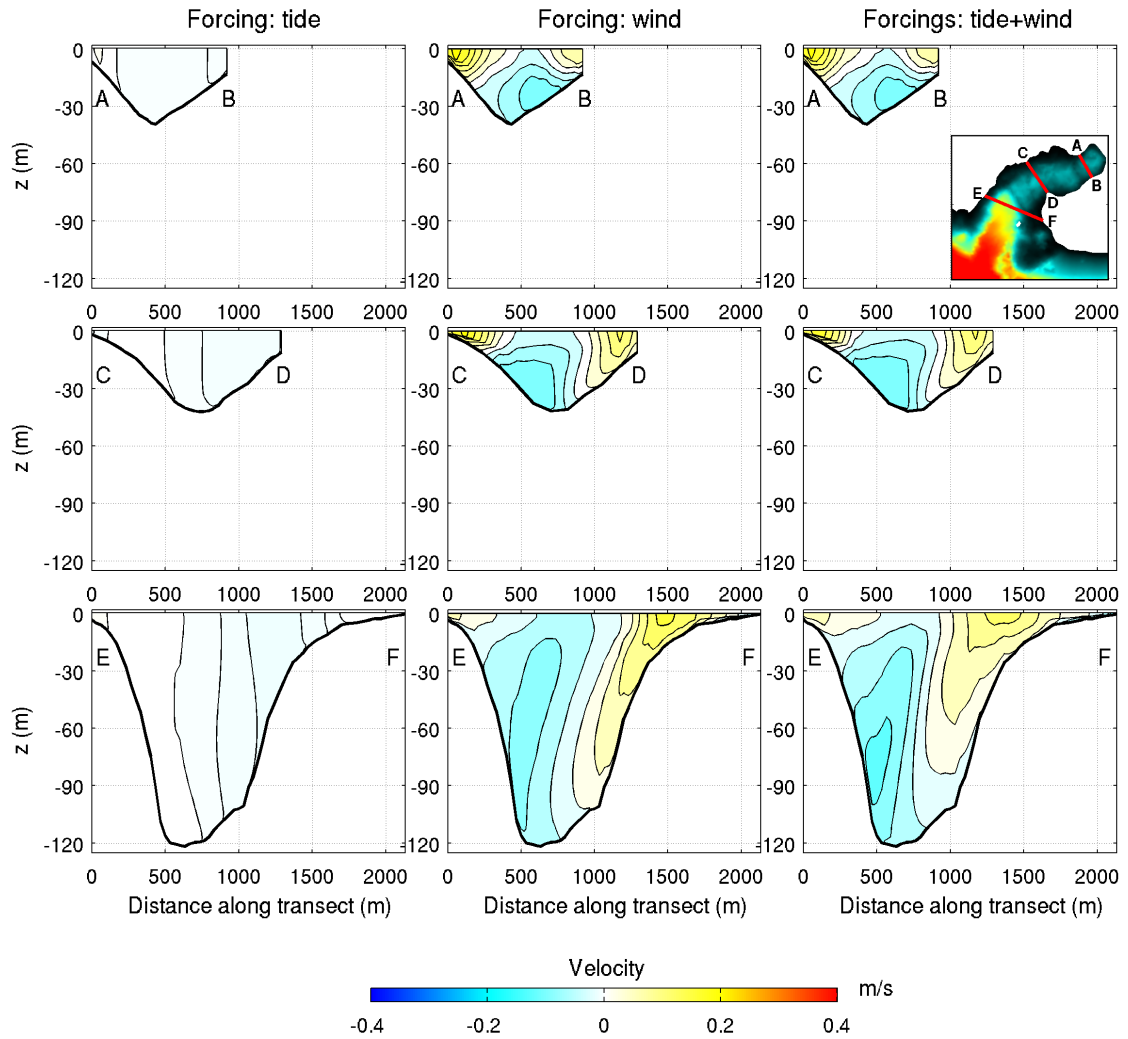
Figure 4.23: Normal flows (in m/s) through the transects (see inset) with respect to different forcings in Potter Cove on 15-Jan-1999 (strong wind condition). Positive velocities indicate inflow and negative velocities indicate outflow.
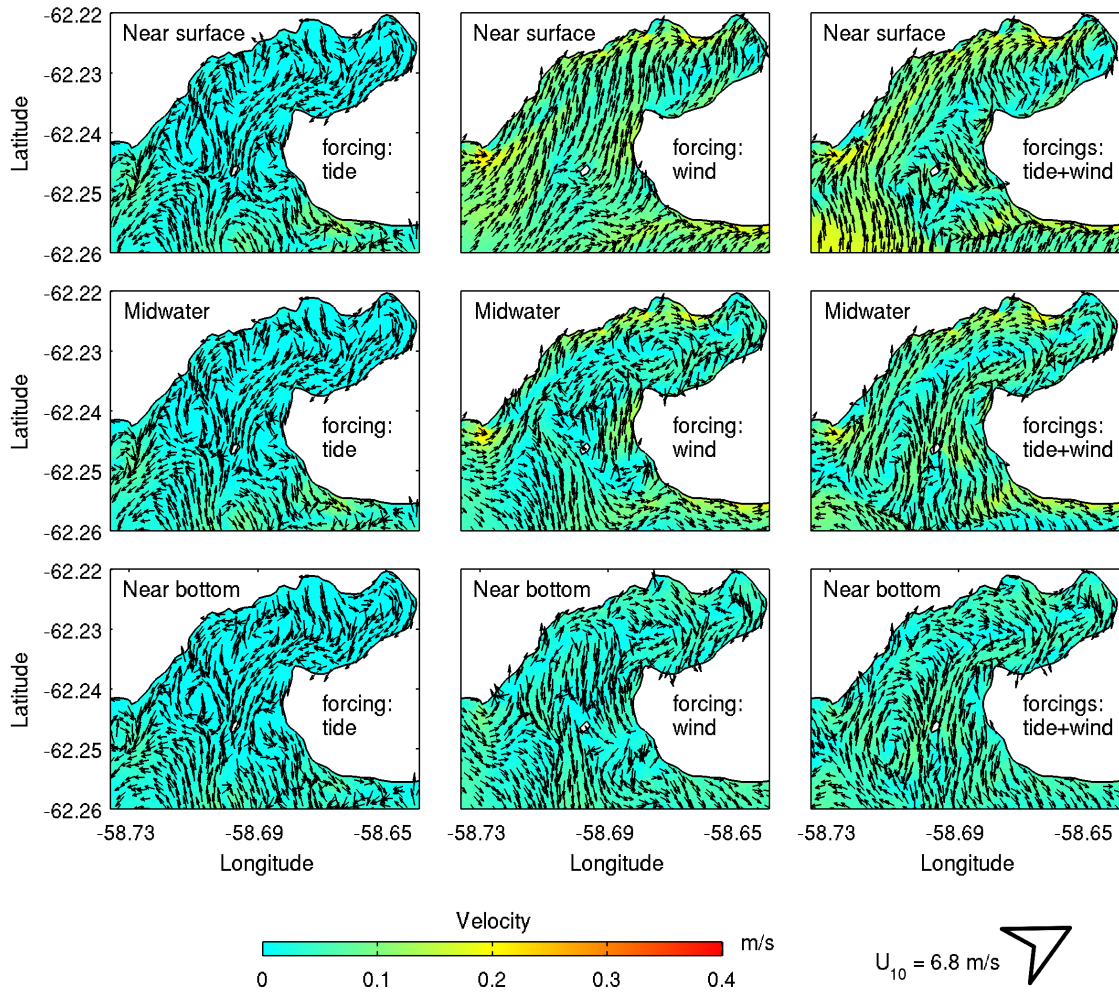
Figure 4.24: Near-surface, midwater and near-bottom circulation patterns with respect to different forcings in Potter Cove on 16-Jan-1999 (moderate wind condition). Wind speed $U_{10}$ and direction (arrow) are indicated in the lower right corner.
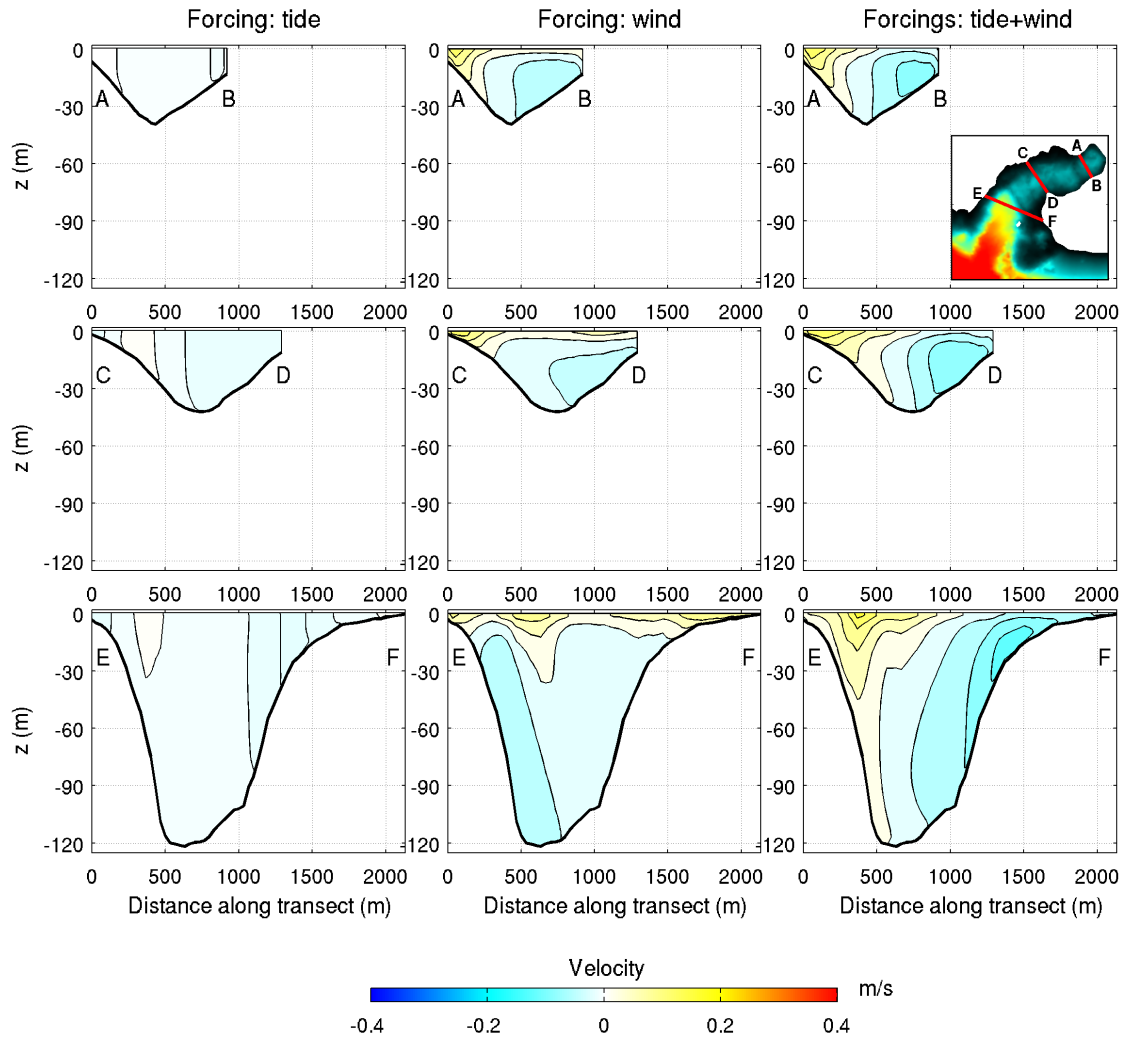
Figure 4.25: Normal flows (in m/s) through the transects (see inset) with respect to different forcings in Potter Cove on 16-Jan-1999 (moderate wind condition). Positive velocities indicate inflow and negative velocities indicate outflow.

Figure 4.26: Near-surface, midwater and near-bottom circulation patterns with respect to different forcings in Potter Cove on 19-Jan-1999 (strong wind condition). Wind speed $U_{10}$ and direction (arrow) are indicated in the lower right corner.

Figure 4.27: Normal flows (in m/s) through the transects (see inset) with respect to different forcings in Potter Cove on 19-Jan-1999 (strong wind condition). Positive velocities indicate inflow and negative velocities indicate outflow.
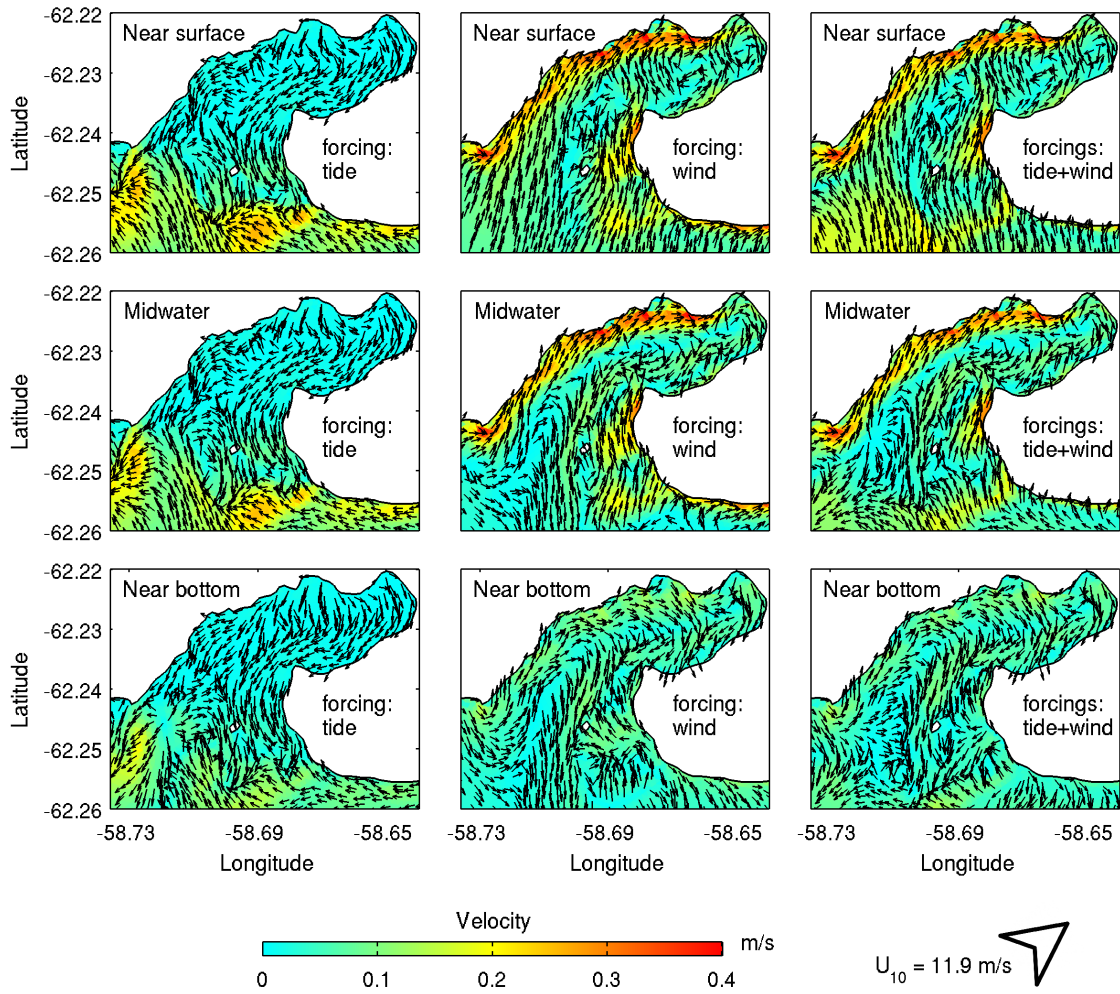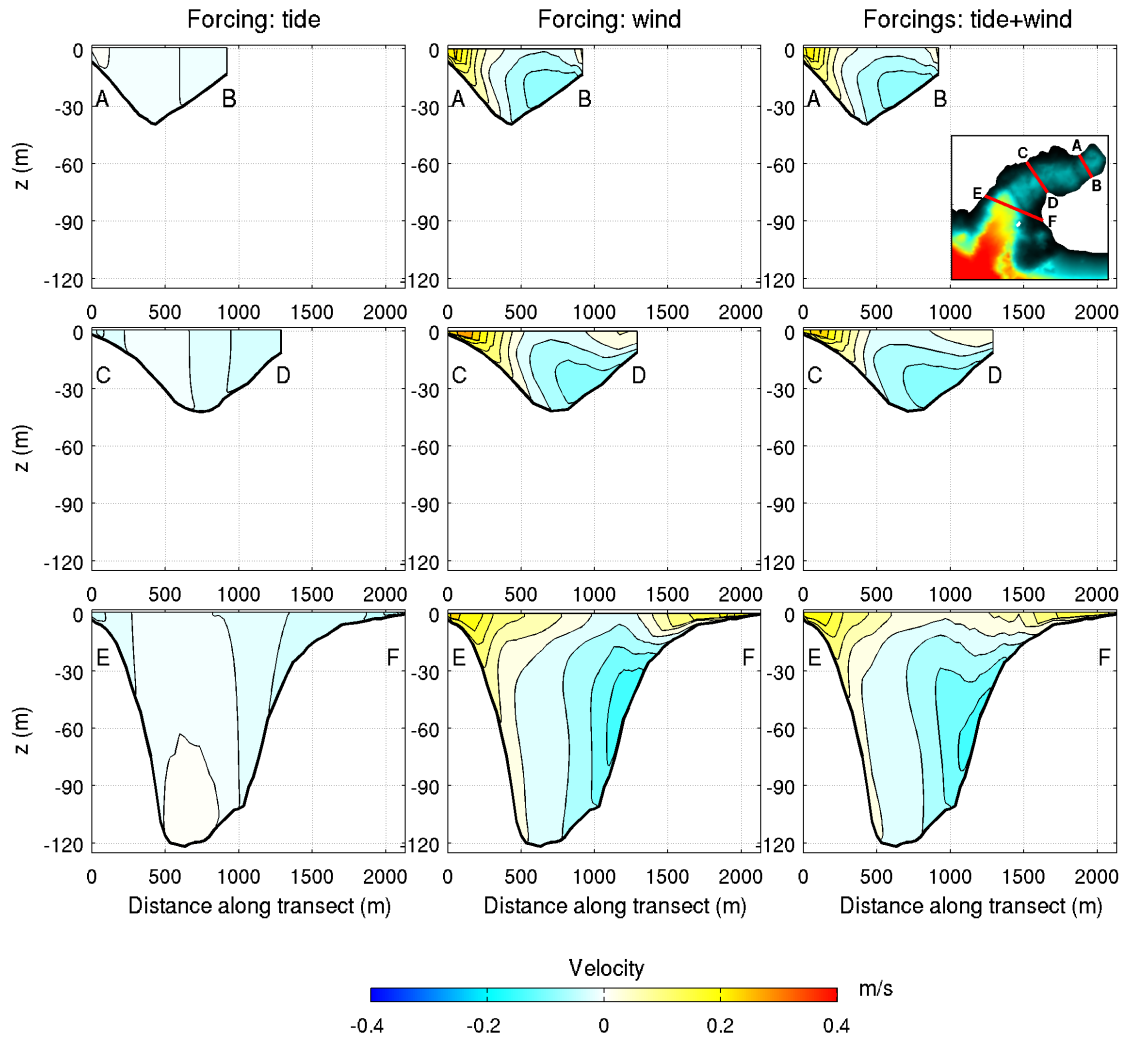
cove. As the wind speed increases from 6.8 m/s (moderate wind condition) to 11.9 m/s (strong wind condition), the water outflow extends slightly further to the north. This can be observed by comparing transects A-B and C-D at the right panels between Figs. 4.25 and 4.27.

In order to further examine and identify whether the current regimes outside of Potter Cove and within the cove are tide-dominated, wind-dominated or mixtures of both, time series of tidal signals, wind speeds, near-surface and near-bottom current speeds due to the tide, wind and the combined effects of tide and wind, as illustrated in Figs. 4.28-4.31, are plotted for different locations at MM ('Maxwell Mouth'), PM ('Potter Mouth'), Dallmann and IC ('Inner Cove'). The current speed signals contain both high and low frequencies. Therefore, a fast-fourier transform (FFT) low-pass filter with a cutoff frequency of 1 day$^{-1}$ is used to filter out all the signals smaller than 1 day and this yields the filtered signals as represented by the black dashed lines as shown in those figures. These filtered signals provide an additional support to better distinguish and identify the various signals in terms of periodicity.

In the vicinity of the mouth of Maxwell Bay at MM, it can be identified from Fig. 4.28 that the near-surface and near-bottom current patterns (by tide+wind) exhibit a similar periodicity in agreement with the tides and tidal-driven currents. Comparing (c) and (d), and (f) and (g), the tidal driven currents are much greater than the wind-driven currents. This analysis further demonstrates that the current regime at MM (outside of Potter Cove) is tide-dominated. At PM, the meeting point between the waters from Potter Cove and external waters, the near-surface flow patterns (by tide+wind), as shown in Fig. 4.29e, demonstrate mixtures of the tidal and wind components, suggesting a mixed influence of tide and wind in this area. At the bottom layer, the current speed (Fig. 4.29h) shows a similar trend as the wind-driven flow (Fig. 4.29g).

At Dallmann and IC in Potter Cove, while the fluctuation of the tidal signals are captured in the near-surface current patterns (by tide+wind), as illustrated in Figs. 4.30e and 4.31e, the current patterns exhibit similar trends and periodicities as the wind-driven currents, as shown in Figs. 4.30d and 4.31d, respectively. Similarly, the near-bottom current speeds (by tide+wind), as presented in Figs. 4.30h and 4.31h, agree with the trends and periodicities by the wind-induced currents (see Figs. 4.30g and 4.31g). The results indicate that the current circulation in Potter Cove is wind-dominated.

### 4.3.3   Tide-, wind- and wave-induced currents

As waves travel, they transport momentum. The transport of wave-induced momentum is equivalent to a radiation stress (Holthuijsen, 2007; Longuet-Higgins and Stewart, 1964). According to Svendsen (2006), radiation stress for a wave motion is defined as the mean momentum flux (or mean force) caused by the waves only. For a wave travelling in a direction $\theta_w$ relative to the positive $x$-direction, the radiation stress component $S_{xx}$ is given as follows:

$$S_{xx} = \left( n - \frac{1}{2} + n \cos^2 \theta_w \right) E \tag{4.6}$$

Figure 4.28: Tidal signals, wind speeds, near-surface and near-bottom current speeds with respect to different forcings at MM (near the opening of Maxwell Bay, see Fig. 2.3a) during 12-22 January 1999. Black dashed lines are signals filtered through FFT low-pass filter with a cutoff frequency of 1 day$^{-1}$.
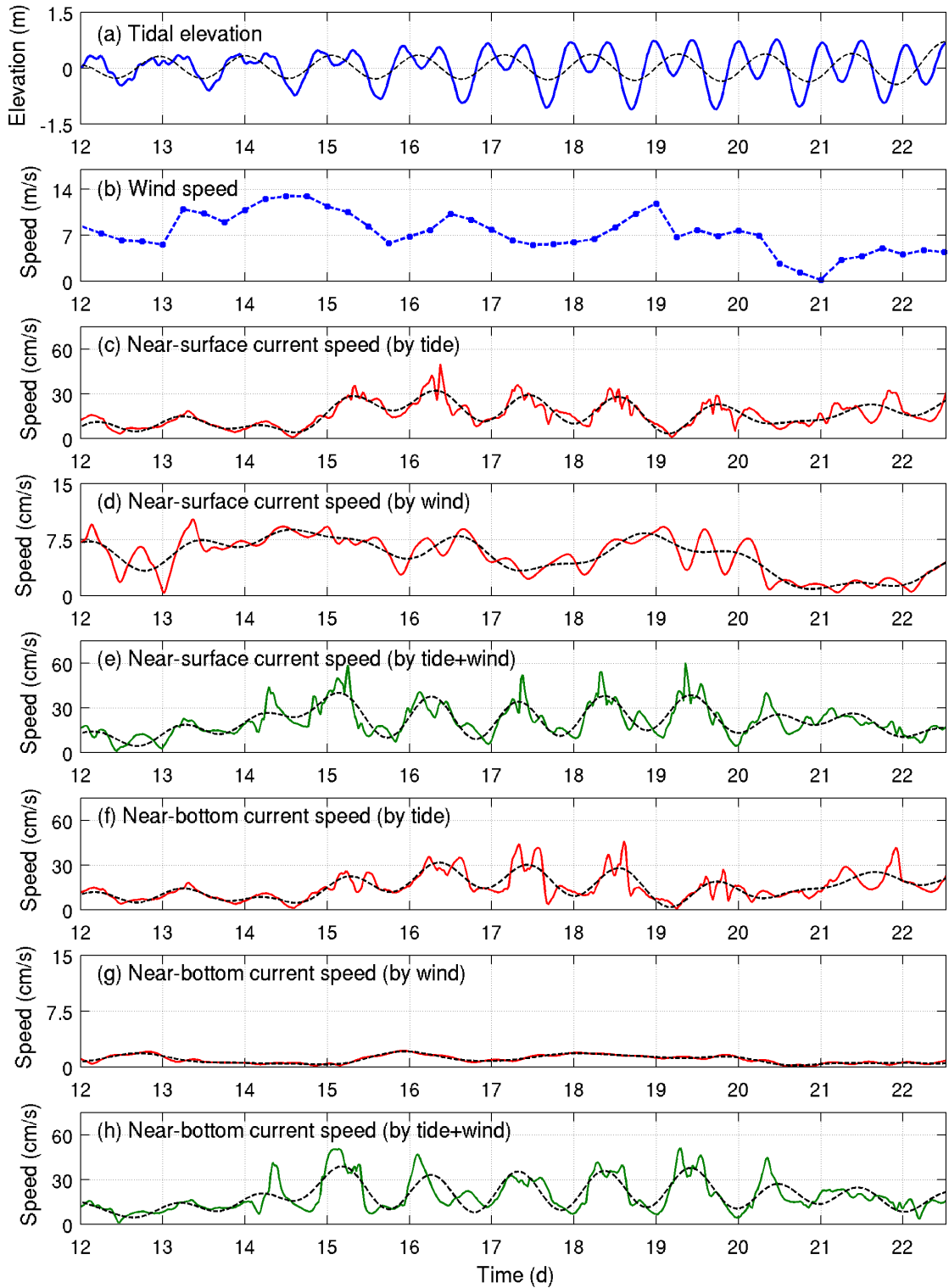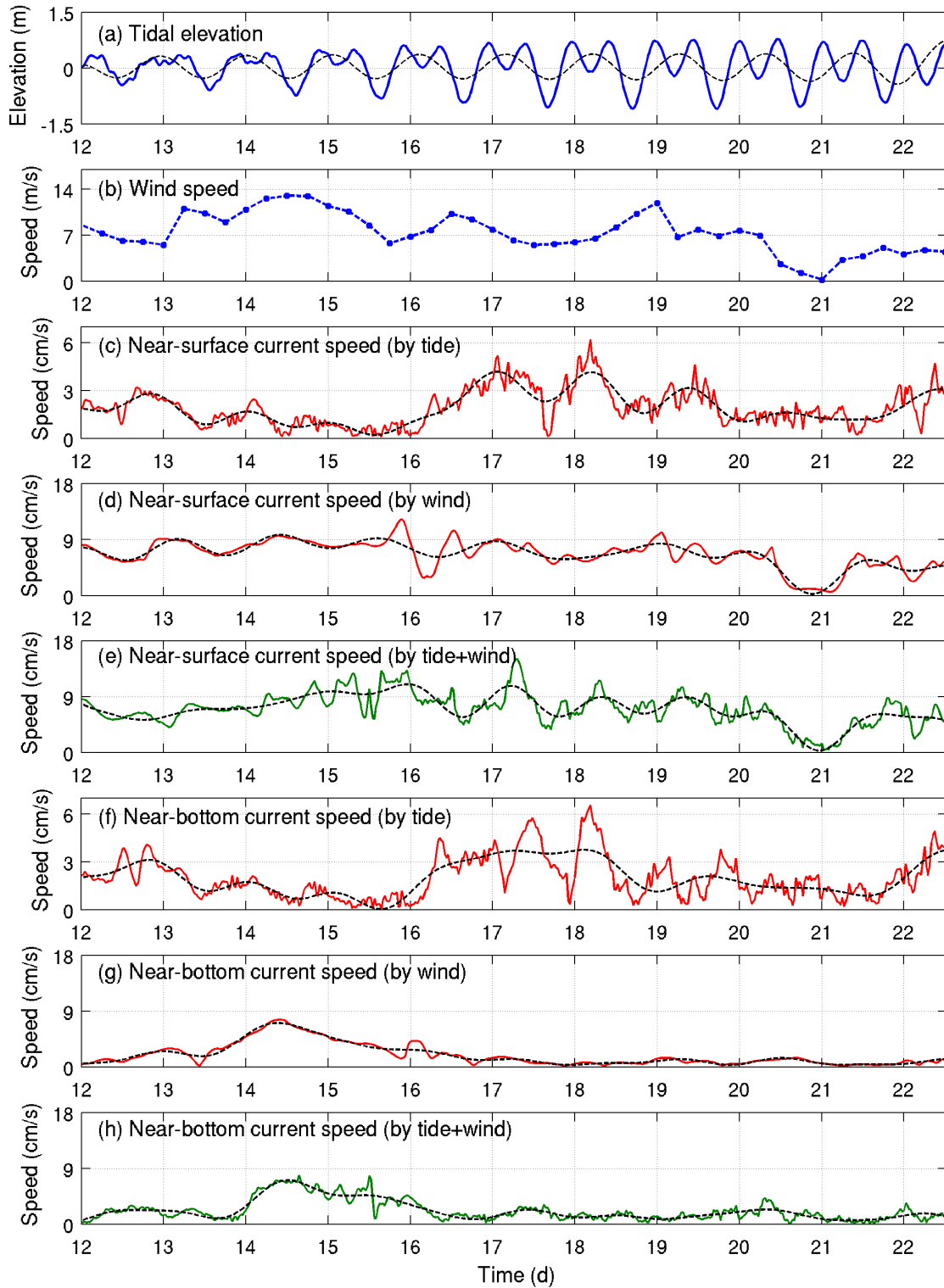
Figure 4.29: Tidal signals, wind speeds, near-surface and near-bottom current speeds with respect to different forcings at PM (near the opening of Potter Cove, see Fig. 2.3b) during 12-22 January 1999. Black dashed lines are signals filtered through FFT low-pass filter with a cutoff frequency of 1 day$^{-1}$.

Figure 4.30: Tidal signals, wind speeds, near-surface and near-bottom current speeds with respect to different forcings at Dallmann, Potter Cove (see Fig. 4.2b) during 12-22 January 1999. Black dashed lines are signals filtered through FFT low-pass filter with a cutoff frequency of 1 day$^{-1}$.

Figure 4.31: Tidal signals, wind speeds, near-surface and near-bottom current speeds with respect to different forcings at IC, Potter Cove (see Fig. 2.3b) during 12-22 January 1999. Black dashed lines are signals filtered through FFT low-pass filter with a cutoff frequency of 1 day$^{-1}$.
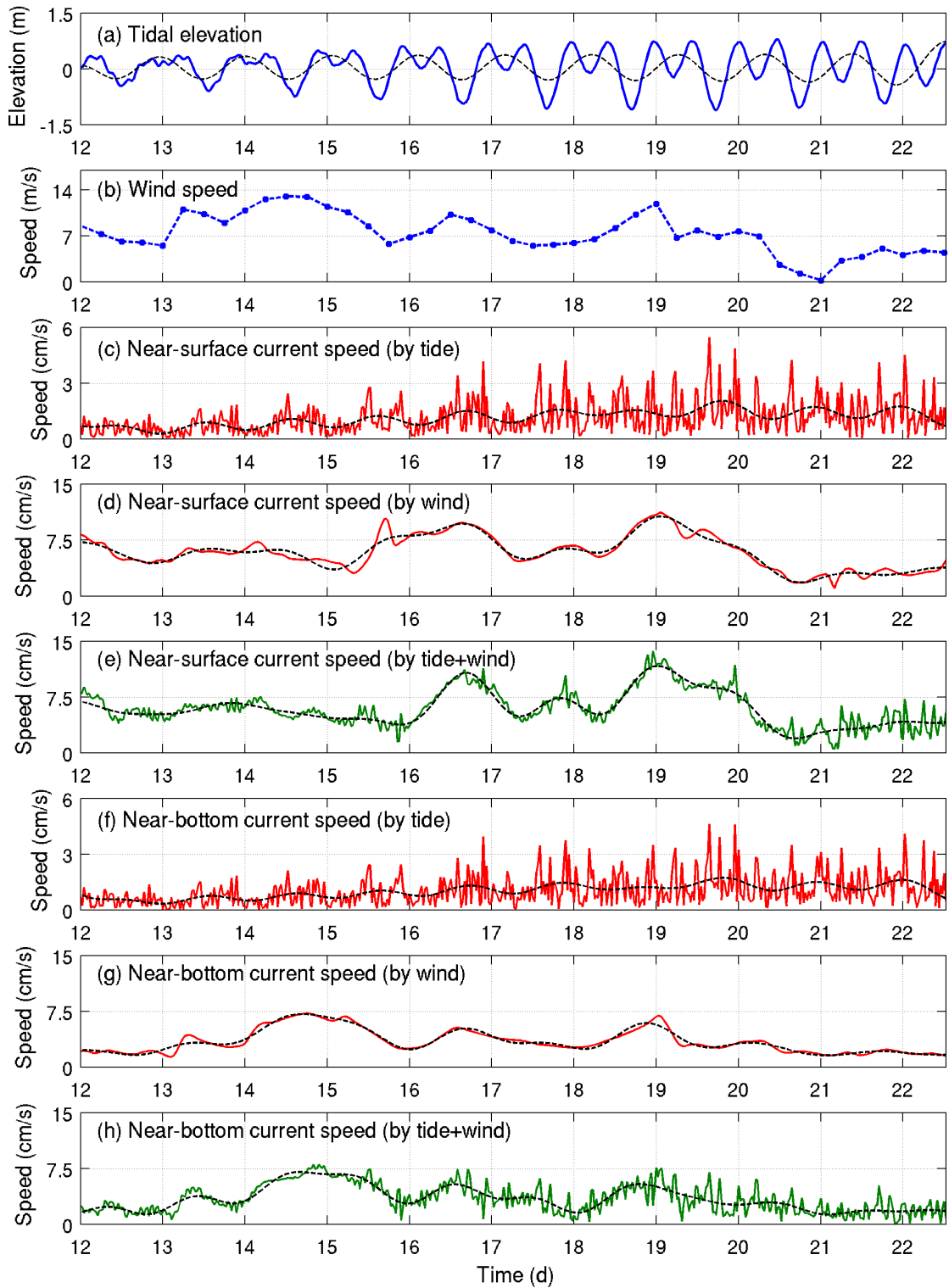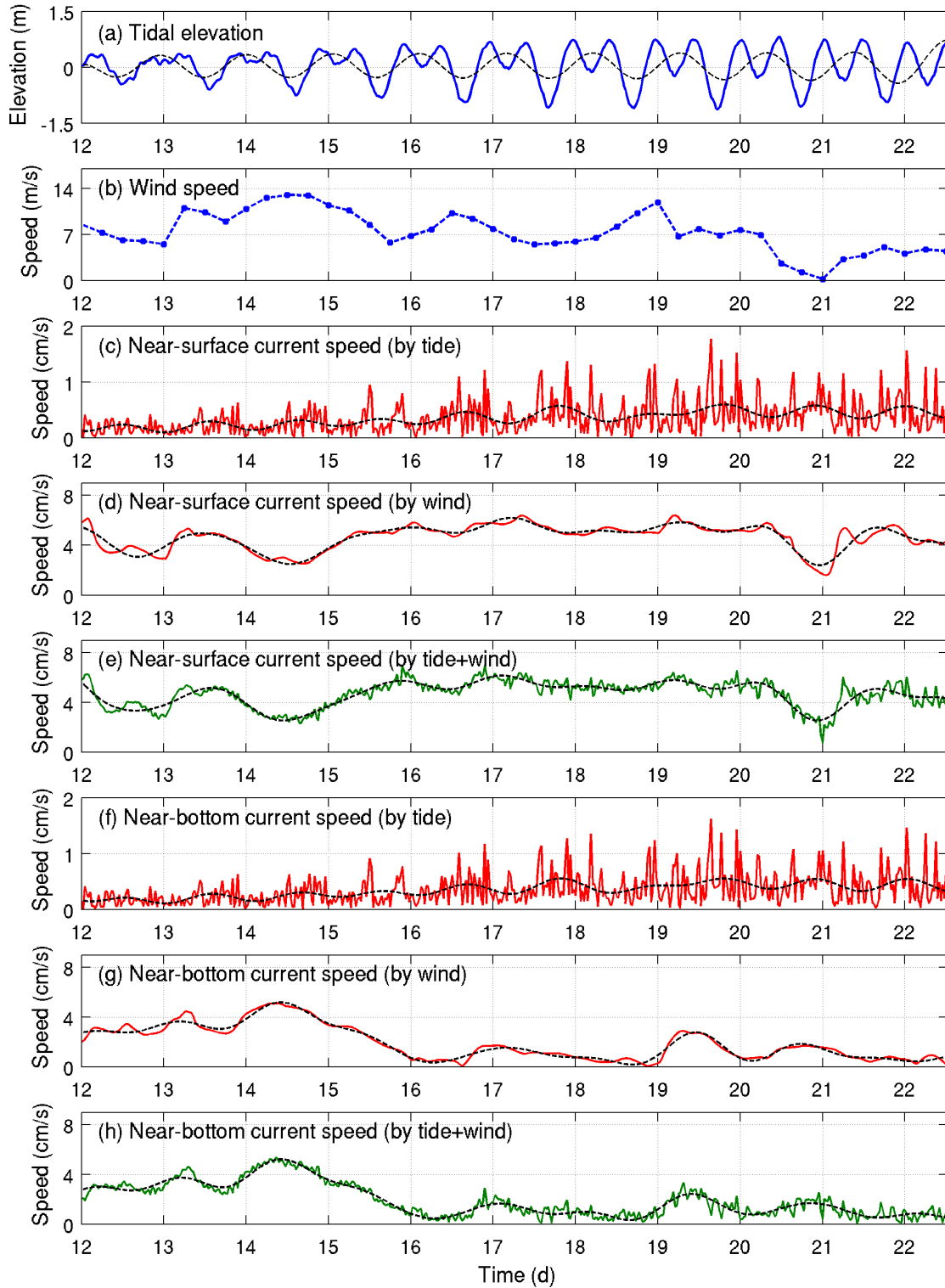
# 4. HYDRODYNAMIC MODELLING

The double $x$ in the subscript of $S_{xx}$ denotes that $x$-momentum is transported in the $x$-direction. $E$ is the wave energy and $n$ is the ratio of the group velocity $c_g$ over the phase speed $c$ (based on linear wave theory) and can be expressed by:

$$n = \frac{1}{2}\left(1 + \frac{2kh}{\sinh(2kh)}\right) \tag{4.7}$$

The other radiation stress components $S_{yy}$, $S_{xy}$, and $S_{yx}$ are:

$$S_{yy} = \left(n - \frac{1}{2} + n\sin^2\theta_w\right)E \tag{4.8}$$

$$S_{xy} = S_{yx} = n\cos\theta_w\sin\theta_w E \tag{4.9}$$

$S_{xx}$ and $S_{yy}$ are equivalent to normal stresses and $S_{xy}$ and $S_{yx}$ to shear stresses.

An increase in radiation stress is equivalent to exerting an opposite force on the water body (Holthuijsen, 2007). Therefore, the corresponding wave-induced radiation forces $F_x$ and $F_y$ per unit horizontal surface area in the $x$-direction and $y$-direction are:

$$F_x = -\frac{\partial S_{xx}}{\partial x} - \frac{\partial S_{xy}}{\partial y} \tag{4.10}$$

$$F_y = -\frac{\partial S_{yy}}{\partial y} - \frac{\partial S_{yx}}{\partial x} \tag{4.11}$$

The minus sign indicates that if the radiation stress decreases in the positive $x$-direction, the corresponding force is directed in the positive $x$-direction, and vice-versa. For detailed theoretical descriptions, see Holthuijsen (2007).

Potter Cove is a dynamically defined system that is susceptible to various wave conditions (see Chapter 3). Wave is another mechanism driving flow in and out of the cove. This will in turn affect the erosion and sedimentation characteristics in Potter Cove. Wave effects on the circulation are important in a nearshore environment where wave-driven flows are induced by various mechanisms of wave dissipation. Wave dissipation generates radiation stress gradients that introduce forces into the water column. In the nearshore zone, wave-induced radiation forces generally generate longshore currents which run parallel and close to the shore.

In FVCOM-SWAVE, three-dimensional radiation stresses (Mellor, 2003, 2005, 2008) are added into the momentum equations to include the wave-driven motions. The governing equations of momentum and continuity with the inclusion of the three-dimensional radiation stresses can be found in Wu et al. (2011). Kumar et al. (2011) performed a comprehensive assessment of the performance of the three-dimensional radiation stress formulation of Mellor (2008) to study nearshore circulation processes. Their results demonstrated that the method works well and captures the dynamics in the surf zone where wave breaking conditions dominate, but may create offshore advection of cross-shore velocity near the surface in the wave shoaling region.

In the present study, the FVCOM-SWAVE simulations were carried out using the central High-Performance Computing (HPC) facilities at the University of Oldenburg. The simulations are computationally very expensive. Apart from high memory utilization, FVCOM-SWAVE adopted for the hydrodynamic model domain with high resolution in certain areas (see Fig. 4.1) are not very useful for long-term simulations due to its long computational run-time. In this study, hydrodynamic and wave modules were run in parallel at the same time on multiprocessor super-computers for a limited simulation period to investigate various wind conditions (or sea states). Tide, wind and wave forcings were activated simultaneously. The time step of 150 s is used for the wave computation.

Fig. 4.32 shows the spatial distributions of $H_s$ in Potter Cove for different sea states under the effects of wave-current interaction. The corresponding circulation patterns are shown in Fig. 4.33. The results revealed that the currents within the cove are dominantly influenced by wind waves, with flows generally driven along the northern sector and towards the inner cove and exiting the cove through the southern sector. A gyre is evident at the inner cove. The wave-current interaction in shallow water regions is particularly prominent. The resulting wave-induced longshore currents are remarkable and dominant especially during strong wind conditions (see right panels in Fig. 4.33). This is distinctly noticeable along the northern coast as well as the western and southern perimeter of Potter Peninsula. Note the comparisons between the circulations with wave influence (see right panels in Fig. 4.33 for longshore currents) and without wave influence (Fig. 4.26). The combined action of tides, winds and waves produces currents as high as 0.4 m/s during rough sea state (19-Jan-1999, 00:00 UTC). Fig. 4.34 shows the normal flows through the transects A-B, C-D and E-F. Again, note the comparisons between the flows with wave influence (see right panels in Fig. 4.34 for longshore currents) and without wave influence (Fig. 4.27).



(a) Mild sea state　　　　(b) Moderate sea state　　　　(c) Rough sea state
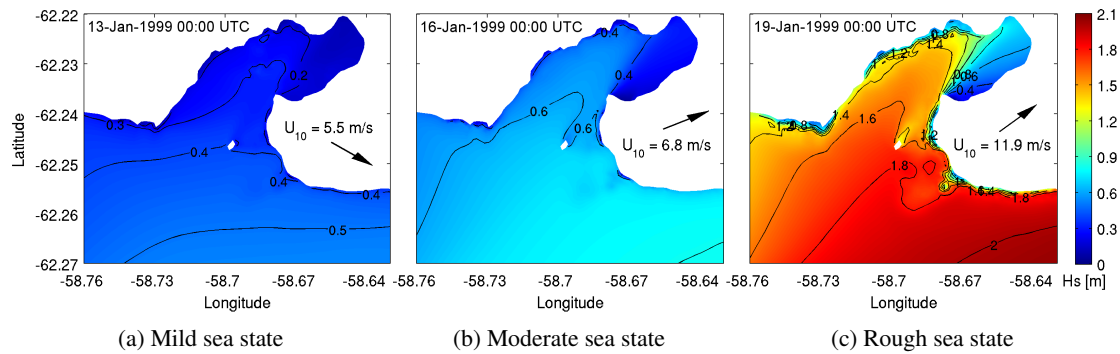
Figure 4.32: Significant wave height contours in Potter Cove for different sea states under the effects of wave-current interaction. The arrows mark the wind directions together with the wind speeds.

A careful examination of the flow fields along the southern coast (Fig. 4.33) indicates that the wave field generates an entering longshore current through a narrow littoral strip. Vodopivez et al. (2001) previously reported that a longshore current along a coastal strip of 10 to 15 m at

the southern coast of Potter Cove has led to a west-to-east sediment transport and caused the spreading of the material supplied by meltwater creeks.
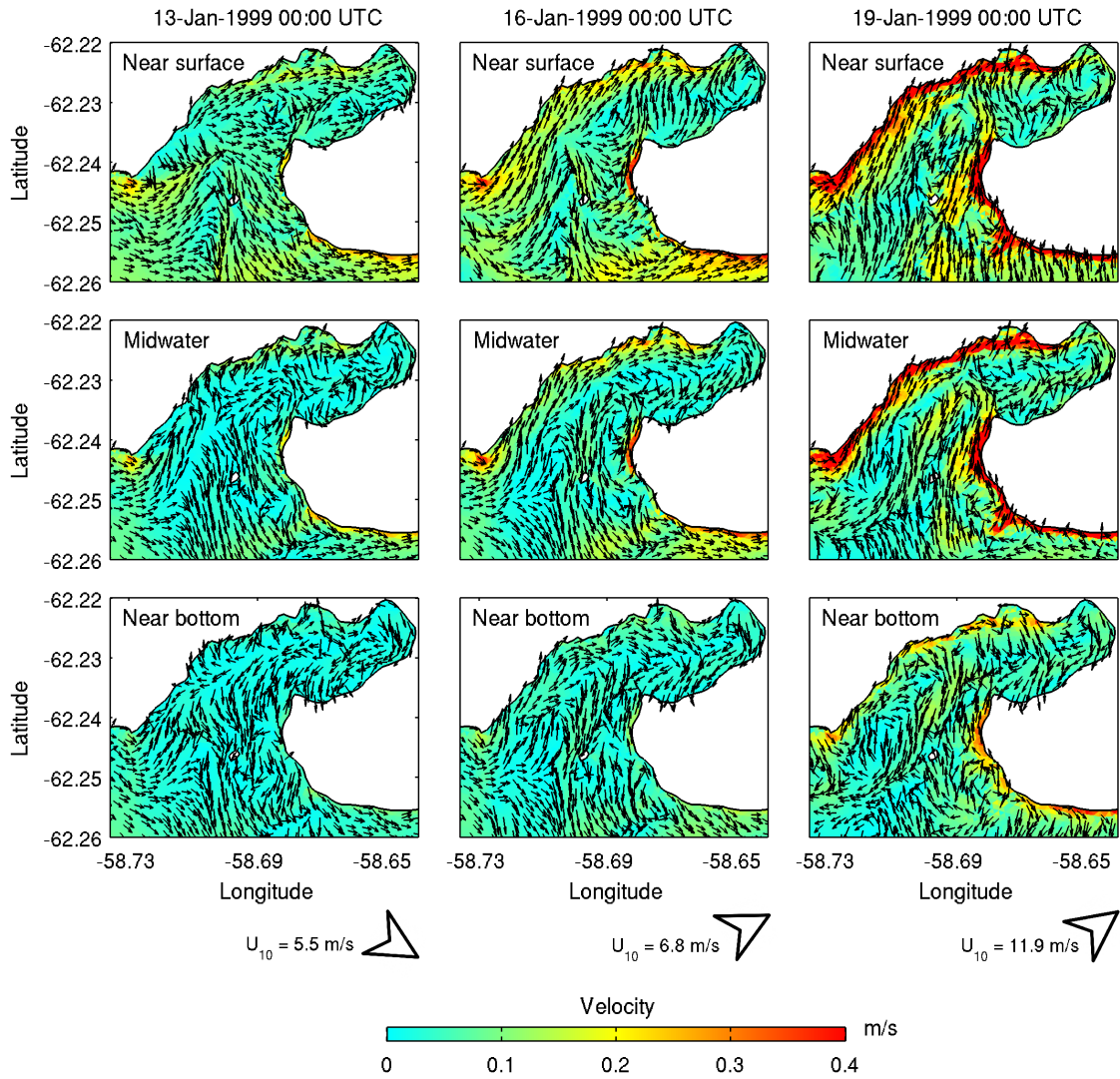


Figure 4.33: Near-surface, midwater and near-bottom circulation patterns (due to the combined action of tides, winds and waves) with respect to different wind conditions (sea states) in Potter Cove. Wind speeds $U_{10}$ and directions (arrows) are indicated at the bottom.
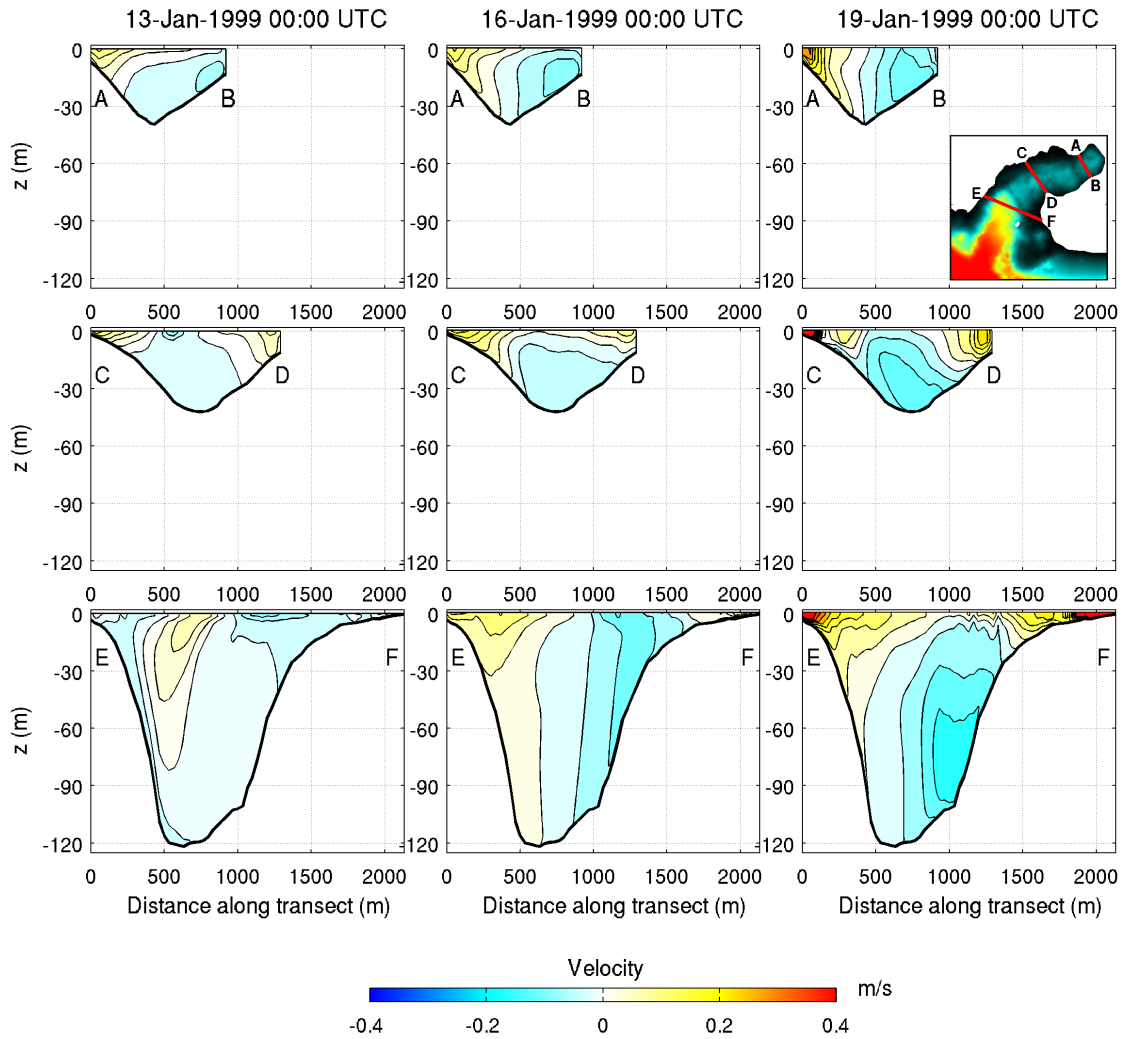
Figure 4.34: Normal flows (in m/s) due to the combined action of tides, winds and waves, through the transects (see inset) with respect to different wind conditions (sea states) in Potter Cove. Positive velocities indicate inflow and negative velocities indicate outflow.

# Chapter 5

# Bed erosion characteristics

## 5.1 Bed shear stress estimation and threshold of sediment motion

### 5.1.1 Total skin friction bed shear stress

Both currents and waves are important hydrodynamic forcing agents in sediment dynamics, especially in coastal regions. Therefore, the total skin friction bed shear stress $\tau$ is taken as the sum of the magnitudes of two skin friction bed shear stress components, i.e. (i) current-induced bed shear stress $\tau_{current}$, and (ii) wave-induced bed shear stress $\tau_{wave}$:

$$\tau = \tau_{current} + \tau_{wave} \tag{5.1}$$

This simple linear approach was also used in other sediment dynamic studies, e.g. in the East Frisian Wadden Sea by Stanev et al. (2006) and in the Black Sea by Stanev and Kandilarov (2012). It is noteworthy that only the skin friction (or grain-related) bed shear stress acts directly on the sediment grains and therefore only this parameter is used to calculate the threshold of sediment motion (Reeve et al., 2004; Soulsby, 1997).

#### 5.1.1.1 Current-induced bed shear stress

The skin friction bed shear stress component due to currents $\tau_{current}$ is a quantity that represents the current flow-induced frictional force acting on sediment grains on the seabed (Soulsby, 1997). $\tau_{current}$ is related to the current speed at the lowest water layer $U$ through a drag coefficient at the bottom $C_d$ by a quadratic friction law:

$$\tau_{current} = \rho C_d U^2 \tag{5.2}$$

$U$ values were extracted from the hydrodynamic model output. The drag coefficient $C_d$, where a

logarithmic velocity profile is assumed, can be calculated as follows:

$$C_d = \left[ \frac{\kappa}{1 + ln(z_0/\Delta h)} \right]^2 \tag{5.3}$$

where $\kappa = 0.40$ is the von Karman's constant, $z_0 = d_{50}/12$ is the bed roughness length. The seabed in Potter Cove consists of coarse- and fine-grained materials (Hass et al., 2013). Therefore the median grain diameter $d_{50}$ is set to 63 $\mu$m, which is the borderline between coarse and fine grained soils according to a soil classification (BS EN ISO 14688-1, 2002). $\Delta h$ is the thickness of the lowest water layer.

### 5.1.1.2 Wave-induced bed shear stress

Wind waves are an important forcing agent in bed sediment dynamics. They are a particularly strong erosive agent in stirring up seabed sediments in most coastal waters, depending on the wave energy and characteristics as well as the types of sediments on the seafloor. Oscillatory velocity induced by waves in shallow water acts on sediment grains and generates wave skin-friction bed shear stress $\tau_{wave}$, which can be computed from the wave orbital velocity near the seabed $U_w$ and the wave friction factor $f_w$ (Soulsby, 1997):

$$\tau_{wave} = \frac{1}{2}\rho f_w U_w^2 \tag{5.4}$$

where $\rho = 1027$ kg/m$^3$ is the density of the sea water.

The bottom orbital velocity $U_w$ can either be extracted directly from the wave model output (i.e. $U_{bot} = \sqrt{2}U_{rms}$ in SWAN and see Eq. 3.15 for $U_{rms}$), which is the case in the present study, or approximated by linear wave theory assuming a monochromatic wave with significant wave height $H_s$ and peak period $T_p$ in water of depth $h$:

$$U_w = \frac{\pi H_s}{T_p \sinh(kh)} \tag{5.5}$$

where the wave number $k = 2\pi/L$, and $L$ is the wavelength. The wave spectral properties ($H_s$, $T_p$ and $L$) were also computed by the wave model.

Depending on the types of flow (laminar, smooth turbulent or rough turbulent), the wave friction factor $f_w$ can be determined based on the formulations and procedures described in Soulsby (1997) and Whitehouse et al. (2000) as follows:

$$f_w = max\left\{ f_{wr}, f_{ws} \right\} \tag{5.6}$$

The rough bed friction factor $f_{wr}$ can be calculated from:

$$f_{wr} = 1.39 \left(\frac{A}{z_0}\right)^{-0.52} \tag{5.7}$$

where $A = U_w T / 2\pi$ is the semi-orbital excursion, $T$ is the wave period ($T_p$ is used).

The smooth bed friction factor $f_{ws}$ can be approximated by:

$$f_{ws} = B R_w^{-N} \tag{5.8}$$

Depending on the wave Reynolds number $R_w$ (Eq. 5.9), the coefficients $B$ and $N$ are given in Table 5.1.

$$R_w = \frac{U_w A}{\nu} \tag{5.9}$$

where $\nu = 1.787 \times 10^{-6}$ m$^2$/s is the kinematic viscosity. The flow is said to be rough turbulent when $f_{wr} > f_{ws}$.

Table 5.1: The coefficients $B$ and $N$ for the determination of $f_{ws}$ (Soulsby, 1997; Whitehouse et al., 2000)

| Wave Reynolds number $R_w$ | $B$ | $N$ |
|---|---|---|
| $R_w \leq 5 \times 10^5$ (laminar flow) | 2 | 0.5 |
| $R_w > 5 \times 10^5$ (smooth turbulent flow) | 0.0521 | 0.187 |

A similar approach was also used in the investigations of the wave impacts on bed shear stress, e.g. in the East Frisian Wadden Sea by Lettmann et al. (2009) and Stanev et al. (2006), and in the Black Sea by Stanev and Kandilarov (2012).

### 5.1.2 Critical bed shear stress

The threshold of motion of sediments at the seabed can be given in terms of a critical (or threshold) bed shear stress $\tau_{cr}$. The incipient motion of a sediment grain in response to currents and waves occurs when the force exerted by the total skin friction bed shear stress acting on the grain exceeds the submerged weight of the grain counteracting it (Soulsby, 1997). The threshold of movement appears if the Shields parameter reaches a critical value and this can be represented by the threshold Shields parameter $\theta_{cr}$:

$$\theta_{cr} = \frac{\tau_{cr}}{g(\rho_s - \rho)d_{50}} \tag{5.10}$$

where $\rho_s$ is the sediment grain density. The study by Monien et al. (2011) suggested that the geochemical composition of the sediments in Maxwell Bay is characterized by tholeiitic basaltic andesite bed material, mostly determined by the lithogenic background of Barton Peninsula and

adjacent areas. Thus, it is assumed that the bottom sediment of Potter Cove consists of similar bed material and therefore the sediment density is set to $\rho_s = 2650$ kg/m$^3$.

The erosional behaviour of non-cohesive sediments has been determined empirically and described in Soulsby (1997) as the dimensionless threshold Shields parameter $\theta_{cr}$, which is given as an algebraic expression as follows:

$$\theta_{cr} = \frac{0.30}{1 + 1.2D_*} + 0.055\left[1 - \exp(-0.020D_*)\right] \tag{5.11}$$

where the dimensionless grain size $D_*$ is defined as:

$$D_* = \left[\frac{g(s-1)}{\nu^2}\right]^{1/3} d_{50} \tag{5.12}$$

where $s = \rho_s/\rho$. Therefore, based on Eq. 5.10, the critical bed shear stress $\tau_{cr}$ is calculated to be 0.13 N/m$^2$. This indicates that the sediment grains begin to move when the skin friction bed shear stress is greater than $\tau_{cr}$.

## 5.2 Bed shear stresses

Model outputs such as current speeds (due to tides, winds and waves) at the lowest water layer $U$, wave orbital velocity near the seabed $U_w$ and wave parameters were extracted from the FVCOM-SWAVE and SWAN models operated at the Insitute for Chemistry and Biology of the Marine Environment (ICBM), Universität Oldenburg, Germany, for the calculation of the bed shear stresses.

### 5.2.1 Current-induced bed shear stress

Current-induced bed shear stresses $\tau_{current}$ for three different sea states are presented in Fig. 5.1. The upper limit of the colourmap for $\tau_{current}$ is specified to a maximum of 0.13 N/m$^2$, which corresponds to the critical bed shear stress value $\tau_{cr}$, to delineate the bed erosion prone areas. The scenario on 19-Jan-1999 is chosen to describe the bed shear stresses for the case of rough sea state. During mild and moderate wave conditions, the current-induced bed shear stresses are generally very low (Figs. 5.1a-5.1b). Under rough sea condition, $\tau_{current}$ becomes more significant, especially in the shallower water regions (Fig. 5.1c). Some areas along the northern coast as well as the western and southern coasts along the perimeter of Potter Peninsula in Fig. 5.1c are susceptible to relatively higher current-induced bed shear stresses that exceed the $\tau_{cr}$ value, indicative of potential bed sediment erosion.

### 5.2.2 Wave-induced bed shear stress

Wave-induced bed shear stresses $\tau_{wave}$ for the three different sea states are shown in Fig. 5.2. It has been previously reported that strong winds, which in turn generate waves, have been observed

(a) Mild sea state, 13-Jan-1999, 00:00:00 UTC

(b) Moderate sea state, 16-Jan-1999, 00:00:00 UTC

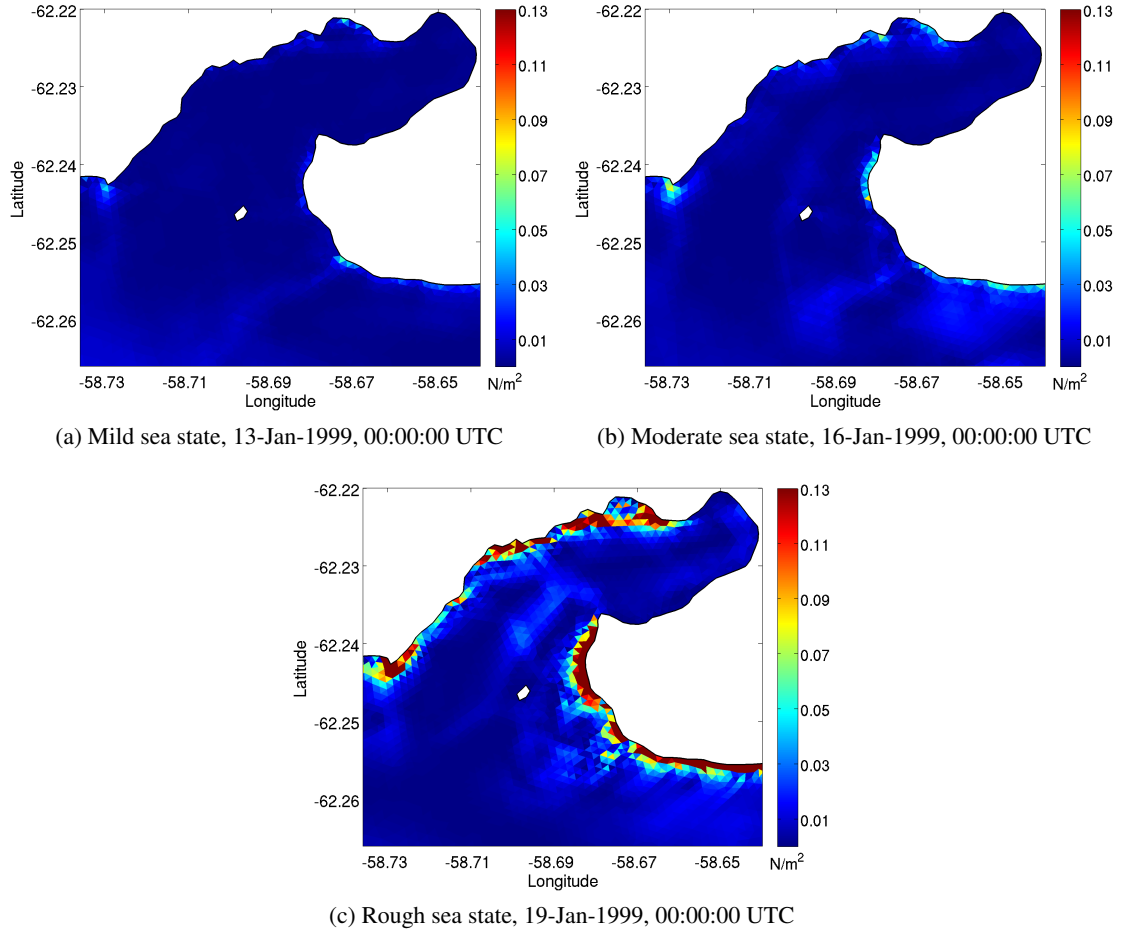(c) Rough sea state, 19-Jan-1999, 00:00:00 UTC

Figure 5.1: Current-induced bed shear stress. The upper limit of the colourmap for the bed shear stress is specified to a maximum of 0.13 N/m$^2$ (equal to $\tau_{cr}$) to delineate the bed erosion prone areas.

in Potter Cove (Klöser et al., 1994; Roese and Drabble, 1998; Schloss et al., 2012; Schloss and Ferreyra, 2002). It can be clearly seen from the figure that waves have an enormous impact on the bed shear stress in Potter Cove. The wave influence is discernible in shallower waters and the impact decreases quickly with increasing water depth. The spatial variability of $\tau_{wave}$ shows that the seabed regions with shallow water depths are prone to sediment erosion ($\tau_{wave} > 0.13$ N/m$^2$). Bed shear stress at the inner cove was estimated to be markedly low, which can be attributed to the relatively small $H_s$ in the region (see the right panels in Fig. 3.9). As the waves enter Potter Cove, a proportion of the wave energy is dissipated. In addition, the coastal waters along the southern coast of Potter Cove are partially sheltered by Mirounga Point. This explains the resulting low bed shear stress values in the area. By comparing the spatial distributions of the wave-induced bed shear stress (Fig. 5.2) with the current-induced bed shear stress (Fig. 5.1), the results show that waves play a more significant role in bed sediment erosion characteristics in Potter Cove.
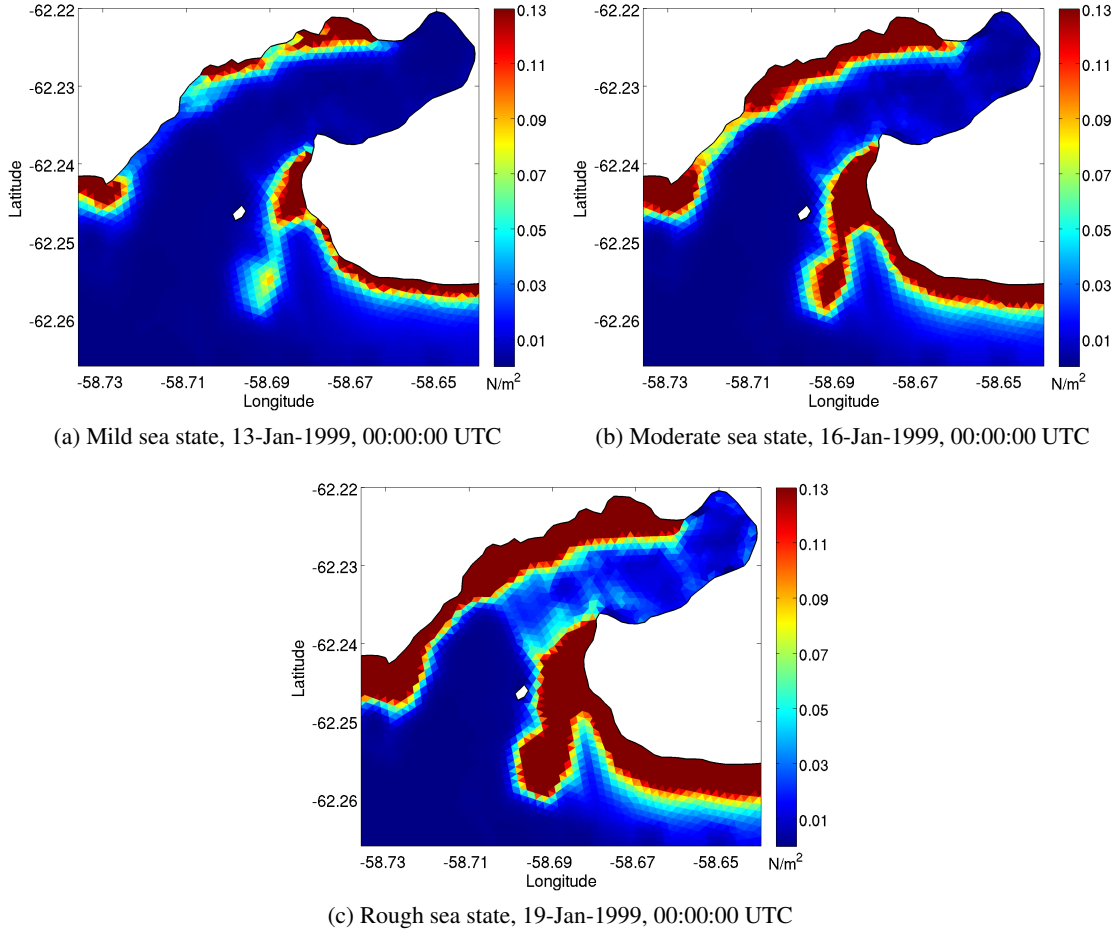
(a) Mild sea state, 13-Jan-1999, 00:00:00 UTC



(b) Moderate sea state, 16-Jan-1999, 00:00:00 UTC



(c) Rough sea state, 19-Jan-1999, 00:00:00 UTC

Figure 5.2: Wave-induced bed shear stress. The upper limit of the colourmap for the bed shear stress is specified to a maximum of 0.13 N/m$^2$ (equal to $\tau_{cr}$) to delineate the bed erosion prone areas.

### 5.2.3 Total skin friction bed shear stress

The total skin friction bed shear stress $\tau$, calculated from the summation of $\tau_{current}$ and $\tau_{wave}$, for the three different sea states is shown in Fig. 5.3. As a whole, Fig. 5.3 provides a general picture of the areas that are favourable for bed sediment erosion in Potter Cove during mild, moderate and rough sea conditions. During mild sea state, where $H_s$ is typically below 0.5 m, sediment erosion prone areas are limited to shallow areas, i.e. around Winship Point, at the northern coastal areas of Potter Cove, and the western and southern coastal areas along the perimeter of Potter Peninsula, as shown in Fig. 5.3a. As the sea state goes from mild over moderate to rough conditions, the areas favourable for sediment erosion are extended to deeper water depths (Figs. 5.3b and 5.3c). The distributions illustrate similarities between the total bed shear stress (also the wave-induced bed shear stress) and the total energy dissipation (Fig. 3.14a). This is particularly noticeable in areas where active energy dissipation occurs.

(a) Mild sea state, 13-Jan-1999, 00:00:00 UTC



(b) Moderate sea state, 16-Jan-1999, 00:00:00 UTC



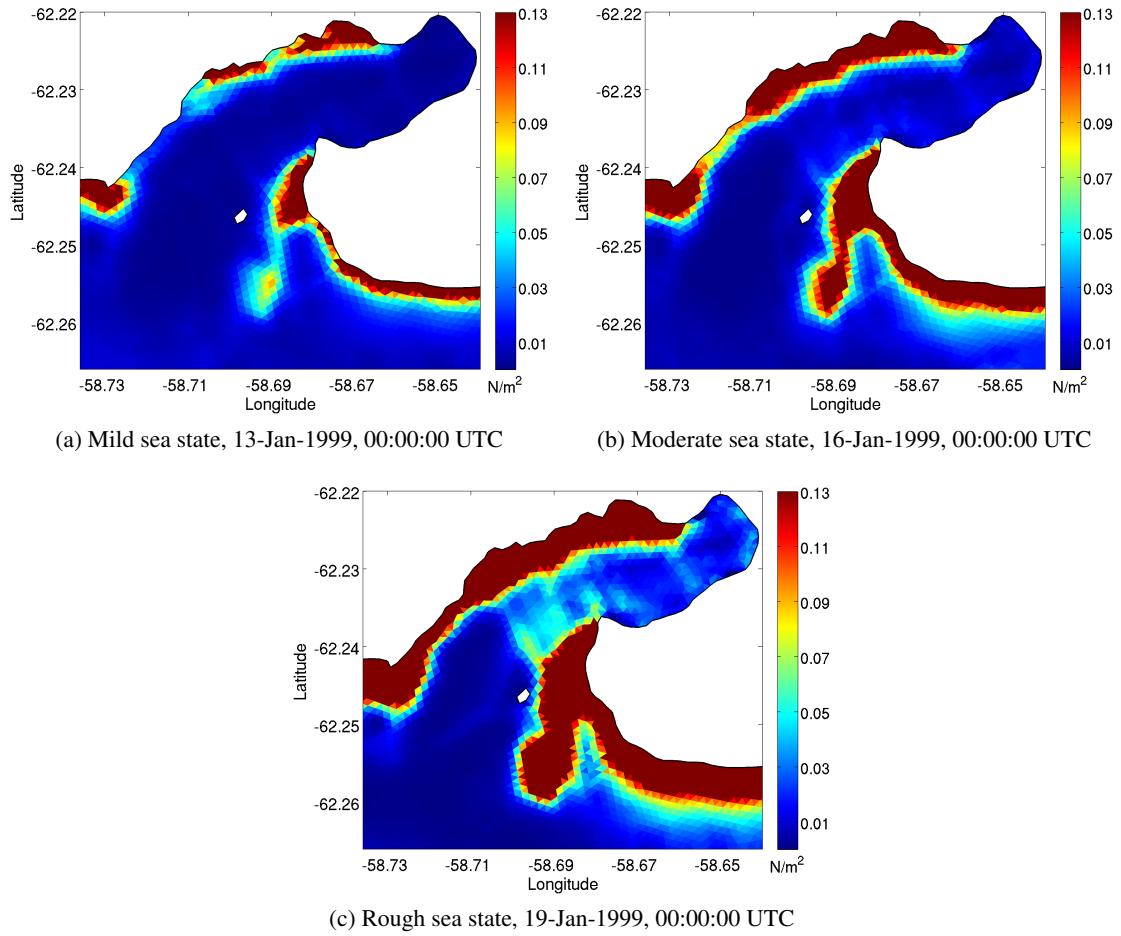(c) Rough sea state, 19-Jan-1999, 00:00:00 UTC

Figure 5.3: Total skin friction bed shear stress. The upper limit of the colourmap for the bed shear stress is specified to a maximum of 0.13 N/m$^2$ (equal to $\tau_{cr}$) to delineate the bed erosion prone areas.

The results can also be related to the seafloor habitat map (see Fig. 5.4, Wölfl, 2013, personal comm.) for Potter Cove, as revealed by Hass et al. (2013), where a stony habitat covers the northern coastal regions of the cove and the western area of Potter Peninsula. The stony habitat exhibits stones and boulder fields that are partly covered by macroalgae, interrupted by occasional sediment deposits. Other areas, which include the inner cove, the southern coastal area of Potter Cove along the northern perimeter of Potter Peninsula and the deeper water regions, are characterized by a soft-sedimentary habitat. The soft-sedimentary habitat consists mainly of silt and sandy silt with a scattered occurrence of different marine benthic organisms. Fig. 5.5 shows examples of typical seafloors of soft-sedimentary and stony habitats in Potter Cove, extracted from video recordings (Wölfl, 2013, personal comm.).

Stony or hard bottom indicates that the seafloor region is potentially subject to high bed sediment movement. When the seafloor is constantly subject to large bed shear stress that is greater
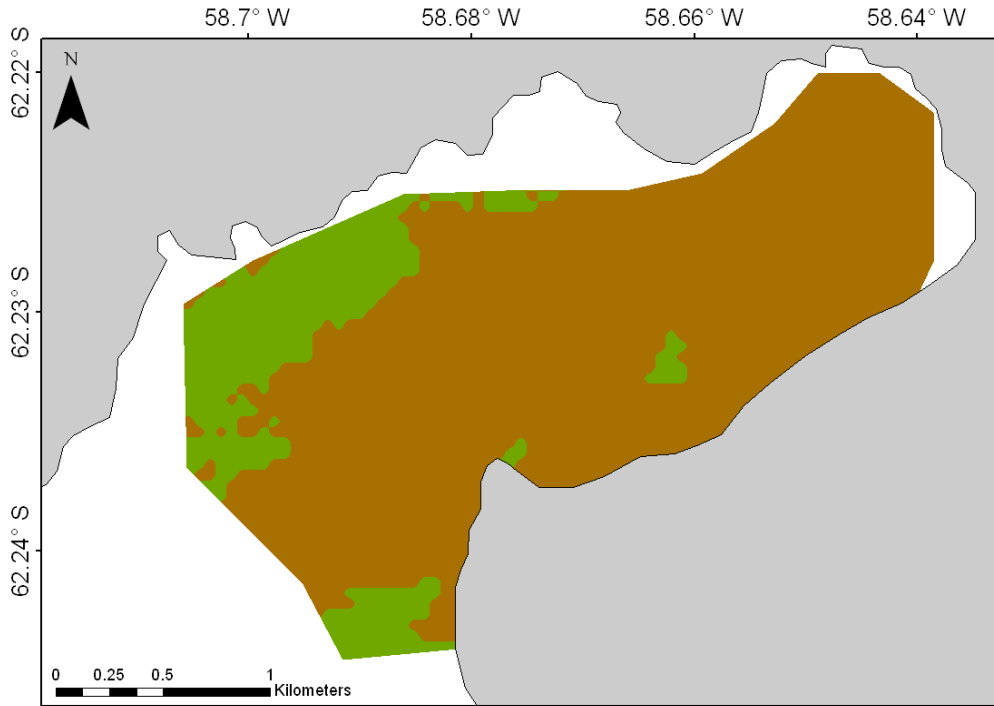
Figure 5.4: Distribution of the stony habitat type (green areas) and soft-sedimentary habitat type (brown areas) in Potter Cove. Image courtesy of Anne-Cathrin Wölfl, Alfred Wegener Institute Helmholtz Centre for Polar and Marine Research (AWI), Germany. Habitat map with detailed soft sediment distribution can be found in Hass et al. (2013).

than $\tau_{cr}$, the bed sediment grains move and are in suspension and subject to be transported away by advection, thus leaving the stones and boulders on the ground. On the contrary, the areas with relatively low bed shear stress can be supported by the presence of soft-sedimentary habitat, indicative of the decreasing influence of wave and current actions on the seabed impairing the bed sediment movement. The bed sediment grains have the tendency to remain static, thus bed sediment erosion is unlikely to take place.

In general, the results are also in line with the findings reported by Quartino and Boraso de Zaixso (2008) where the regions with hard bottom (with macroalgal vegetation) and soft bed sediment in Potter Cove, as illustrated in Fig. 1 of Quartino and Boraso de Zaixso (2008), can be associated with the areas with high and low bed shear stresses found in the present study as shown in Fig. 5.3.

Figure 5.5: Images showing the typical environments of (a) soft-sedimentary habitat and (b) stony habitat in Potter Cove. Images courtesy of Anne-Cathrin Wölfl, Alfred Wegener Institute Helmholtz Centre for Polar and Marine Research (AWI), Germany.

# Chapter 6

# Water transport time scales

Periodic flushing of the intertidal water volume between Potter Cove and the neighbouring waters, i.e. Maxwell Bay and Bransfield Strait, drives the water exchange mechanism. Water within the cove is 'old' while that entering from outside is 'new'. During flood tide, water enters the cove and this 'new water' from outside mixes with the existing water in the cove. Some fraction of water exits the cove during the ebb tide and some remains. During the subsequent flood tide, some 'old water' might return to the cove along with the 'new water'. These processes continue until the whole cove is completely flushed and replaced with the 'new water'.

Besides the tidal range and geomorphological geometry of the cove, the return flow is also a key influence in estimating the water renewal time scales. Sanford et al. (1992) have identified the return flow as an important factor in estimating tidal flushing, considering the fate of a plume of effluent water, which leaves the embayment mouth on ebb tide, mixes with waters outside the embayment, and partially returns to the embayment on flood tide. Apart from the periodic tidal action, wind-generated forces also constantly drive the circulation in the water and the presence of winds is capable of enhancing the flushing, thus adequately maintain the water quality.

There are three commonly used transport time scales (age, residence time and flushing time) to measure the retention of water. Since there are numerous names for the time scales in the literature and the time scales have not been consistently defined, Monsen et al. (2002) have defined and compared the three transport time scales in their paper on the use of these time scales. Transport processes involve various temporal and spatial scales. The water transport time scales of interest to the present study are residence and flushing time scales.

Residence time is defined as the time it takes for a water parcel starting at a specific location within a water body or an embayment to leave it through its outlet or boundaries (Monsen et al., 2002), or alternatively the time it will remain within the water system before exiting. Residence time is the complement to age, which is the time required for a water parcel to travel from a boundary to a specified location within a water body. The flushing time of an embayment is the time required for a well-mixed volume of the entire embayment to be replaced with 'new water'. Flushing time implies the general exchange characteristics or renewal of a water system. Thus,

flushing time is an integrative quantity for the entire embayment whereas residence time is a local time scale, spatially variable within the domain of interest.

## 6.1 Residence time

Residence times have been traditionally calculated based on empirical studies using tracers, box models and tidal prism models. In recent years, 1- and 2-dimensional models have gained much attention and are used in the calculation of the residence times (Abdelrhman, 2005; Cucco and Umgiesser, 2006; Cucco et al., 2009; Hartnett et al., 2003). In this study, the 3-dimensional FVCOM model that numerically represents the hydrodynamic physics is used for the estimation of the residence times to quantify the spatio-temporal behavior for Potter Cove, based on the flow-field information produced from the simulation.

Residence times have been computed following an Eulerian approach (e.g. Abdelrhman, 2002, 2005) by introducing conservative/passive tracers that were instantaneously released and evenly distributed at time $t = 0$ inside and throughout a specified domain of interest (Fig. 6.1), and noting how the concentration of the tracers decreases. Tracers with an initial concentration of 100 g/L were initialized within the domain of interest at 00:00:00 UTC 01-Jan-1999. The external waters were free of tracers. No further tracers were injected after $t = 0$. A 10-day simulation prior to tracer release has been carried out to spin up the hydrodynamic circulation. The cove was assumed to be completely and continuously mixed during the entire simulation.
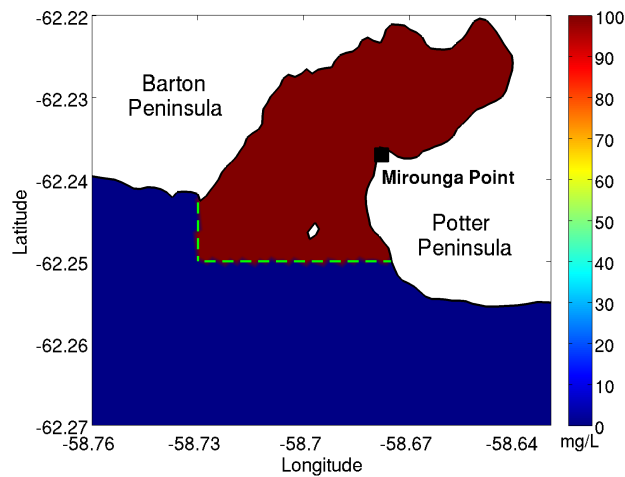


Figure 6.1: Domain of interest where passive tracers were introduced. The green dotted line marks the boundary of the domain.

Based on the concentration change at each individual node, the depth-averaged local residence time (LRT) is calculated as the time period for the concentration of a uniformly distributed tracer

to drop below a threshold value:

$$LRT = T(C(t) > C_{threshold})$$ (6.1)

Figs. 6.2a, 6.2c and 6.2e show an example of a time series of the depth-averaged concentration (represented by the blue asterisks) at a specific node within the domain of interest after the tracer was introduced at $t = 0$. The mean concentration fluctuates over time and the declining pattern continues more or less exponentially as the time increases. Two different methods, i.e. (1) the moving average method, and (2) the exponential fit, have been applied to estimate the LRTs.

Firstly, the moving average method is used to estimate the LRT with $C_{threshold} = 100e^{-1}$. For instance, in Figs. 6.2a and 6.2c, the LRTs were obtained based on the moving averages (represented by the red lines) with $m1$ and $m61$, respectively. $m$ is the number of data points to average over in the moving average. $m1$ indicates that each data point (2-hour interval) is plotted and taken into account while $m61$ takes a moving average of 61 data points (covering 5-day data). In this case, the LRT with the moving average $m1$ is the first time point when the actual concentration falls below $C_{threshold}$. Therefore, the return flow effect after this time point was not taken into consideration.

Secondly, the LRT is estimated from the exponential decay (e.g. Fig. 6.2e). After the end of the tracer injection, the concentration inside the cove is assumed to follow the exponential function:

$$C(t) = C_0 e^{-kt}$$ (6.2)

where $C_0$ is the initial concentration, $e$ is the Euler number and $k$ is the decay constant.

The local concentration that drops below the ratio of $1/e$ of its initial concentration is adopted as the cut off for LRT:

$$\frac{C(LRT)}{C_0} = e^{-kt} = e^{-1}$$ (6.3)

and

$$t = \frac{1}{k}$$ (6.4)

where $1/k$ represents the residence characteristics of the tracer in the system.

Therefore, $C_0 * e^{-1}$ is the threshold value for the LRT. The time quantity associated with the ratio $1/e$ is called the e-folding time and the theoretical definition is presented in Abdelrhman (2002). In this case, a decline of the local depth-averaged concentration to $e^{-1}$ (about 37%) of its initial concentration after a certain time indicates that about 63% of the local water has been exchanged with the 'new water' from outside the cove.

(a) Moving average $m1$



(b) LRT (moving average $m1$)



(c) Moving average $m61$



(d) LRT (moving average $m61$)



(e) Exponential fit
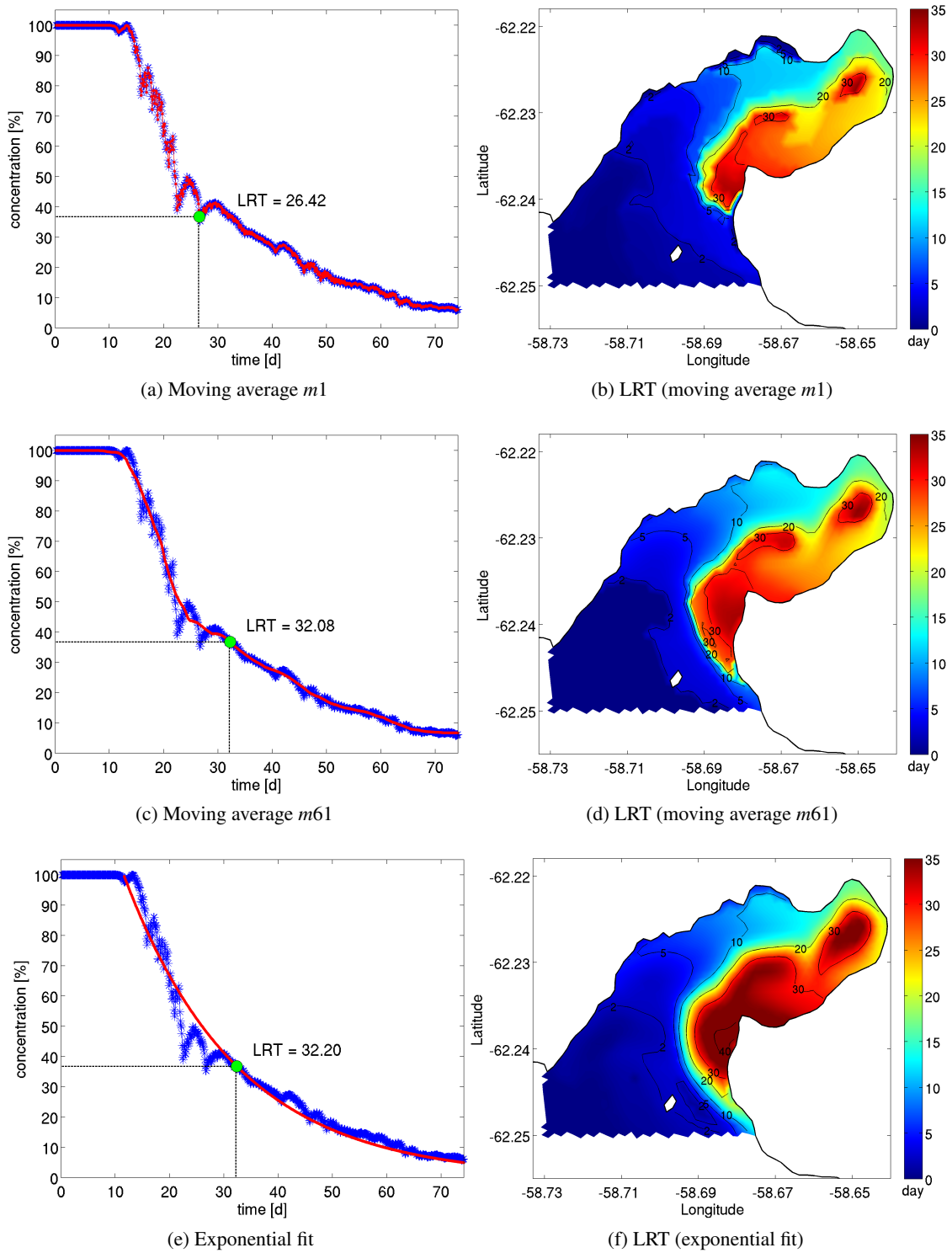


(f) LRT (exponential fit)

Figure 6.2: LRT estimation methods and their corresponding spatial distributions (tidal influence). The blue asterisks (*) represent the FVCOM modelled concentration. The red line shows the moving average and exponential fit.

### 6.1.1 Influence of tides

In this section, only tidal forcing was applied to estimate the LRTs induced by tidal circulation. There were no freshwater inputs from the glacial meltwaters. Figs. 6.2b, 6.2d and 6.2f exhibit the spatial distributions of the LRT over Potter Cove, with respect to the different estimation methods. The three methods yield LRT maps with nearly similar pattern.

As expected, the shortest LRTs ($< 2$ days) are found at the open boundary. The LRTs increase toward the interior of the cove, mainly along the upper half of the cove to the side of Barton Peninsula, to approximately 20 days. Geographipcal distance does have an influence on the LRT. Somehow, the distance from the boundary does not necessarily and directly correspond with the LRT. This is particulary obvious in the case of Potter Cove. As can be seen from the LRT maps in Fig. 6.2, the LRT values for the lower half of the cove to the Potter Peninsula side are in the range of 20 to 35 days or even larger. The regions with the longest LRTs (about 30 days or greater) are found around Mirounga Point (62.237° S, 58.678° W, i.e. northwest of Potter Peninsula) and the central part of the far inner cove. Note that Mirounga Point is only located approximately 1.5 km from the open boundary. The results are reasonable and supported by the general cyclonic circulation in Potter Cove as discussed in Chapter 4. Hence, shorter LRTs at the northern sector and longest LRTs cover the southern sector of the cove. Gyres generated around the central region of the inner cove and at the northeastern and western sides of Mirounga Point (see Section 4.3.1) may further lengthen the LRTs.

In order to further support the LRT results, Fig. 6.3 is produced to show the temporal and spatial distributions of tracer concentration at the surface layer. From the concentration distribution maps, it was observed that the 'new water' initially entered and flushed the upper half of the cove and subsequently replaced the highly concentrated waters near the Potter Peninsula side.

### 6.1.2 Influence of tides and realistic winds

As winds are the dominant driving force in water circulation in Potter Cove, a simulation with tidal and realistic NCEP wind forcings has been carried out to investigate the influence of combined tides and winds on the LRTs. Fig. 6.4 depicts the time evolution of the near-surface distributions of tracer concentration under the tide and realistic wind conditions. The 'new water' entered the mouth of Potter Cove and from 03-Jan-1999 12:00:00 UTC till 04-Jan-1999 18:00:00 UTC, wind speeds became very low (ranging between 1-2 m/s), hence tidal influences became more dominant. As a result, the 'new water' flushed the upper half of the cove, as can be seen in Fig. 6.4, on 5 January. After the low wind speed period, winds began to grow again and continued to influence the tracer distribution towards the inner cove. On 8-9 January, the tracer ($> 60$ g/L) has been observed to be concentrated within the inner cove, especially around the waters near the Potter Peninsula side.

The LRT distributions, influenced by (i) tides, and (ii) combined tides and winds, are presented (Fig. 6.5) for comparisons. The LRT distribution can be related to that of concentration. Due to
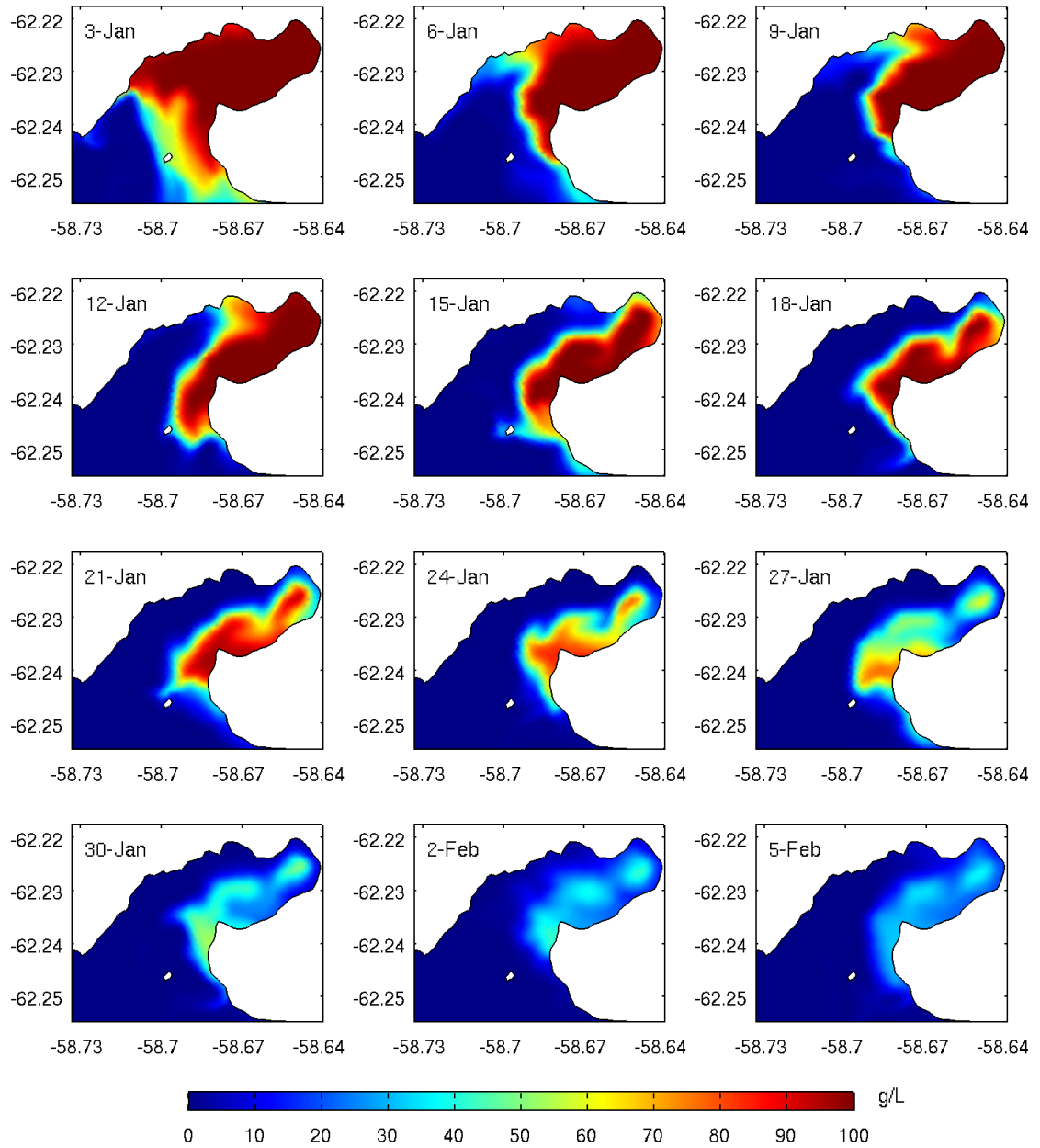
Figure 6.3: Temporal and spatial distributions of tracer concentration at the surface layer (only tidal forcing). Tracer release time: 01-Jan-1999 00:00:00 UTC.
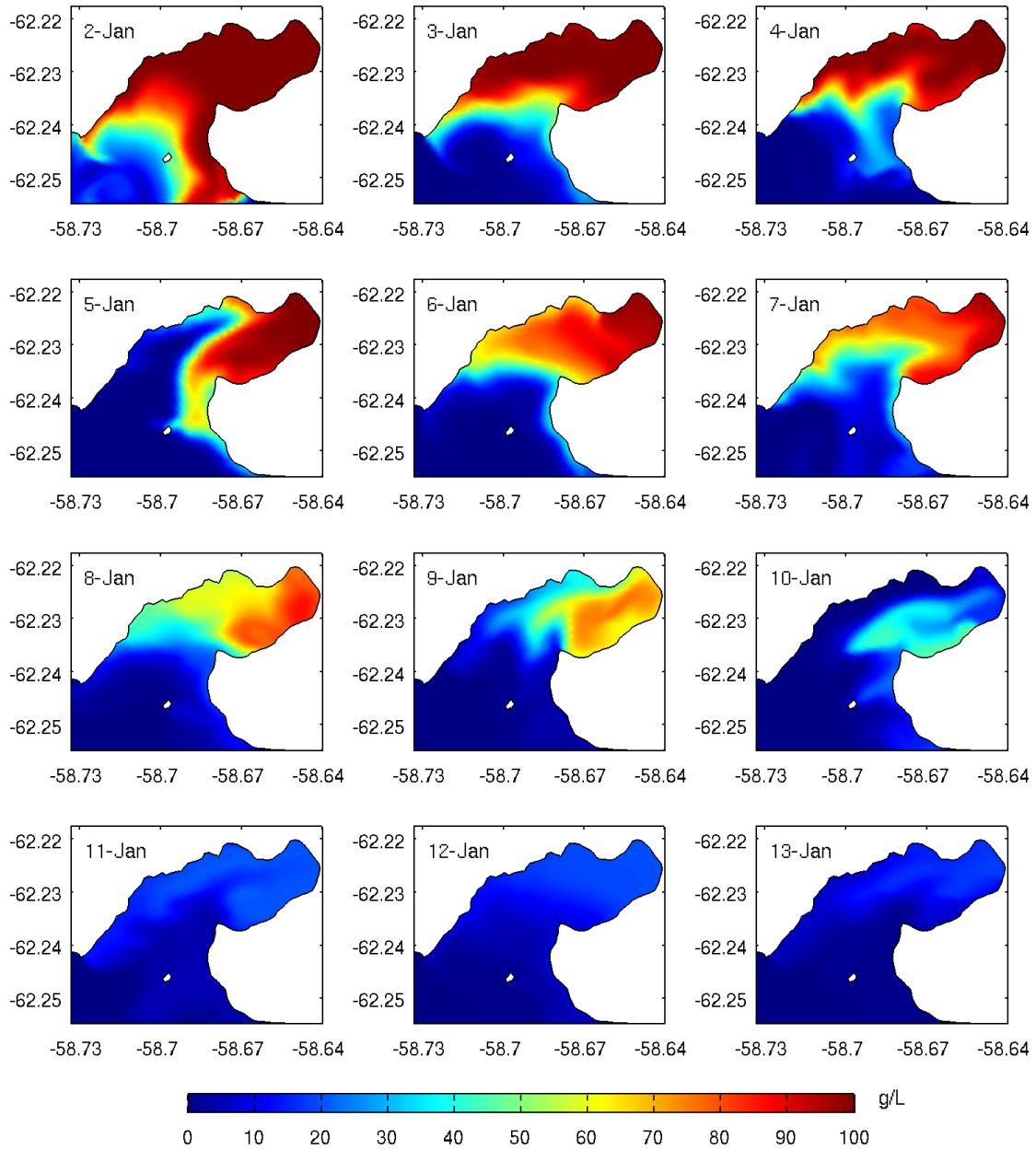
Figure 6.4: Temporal and spatial distributions of tracer concentration at the surface layer (combined tidal and realistic wind forcings). Tracer release time: 01-Jan-1999 00:00:00 UTC.

(a) LRT (tide t)



(b) LRT (tide+realistic wind tw)
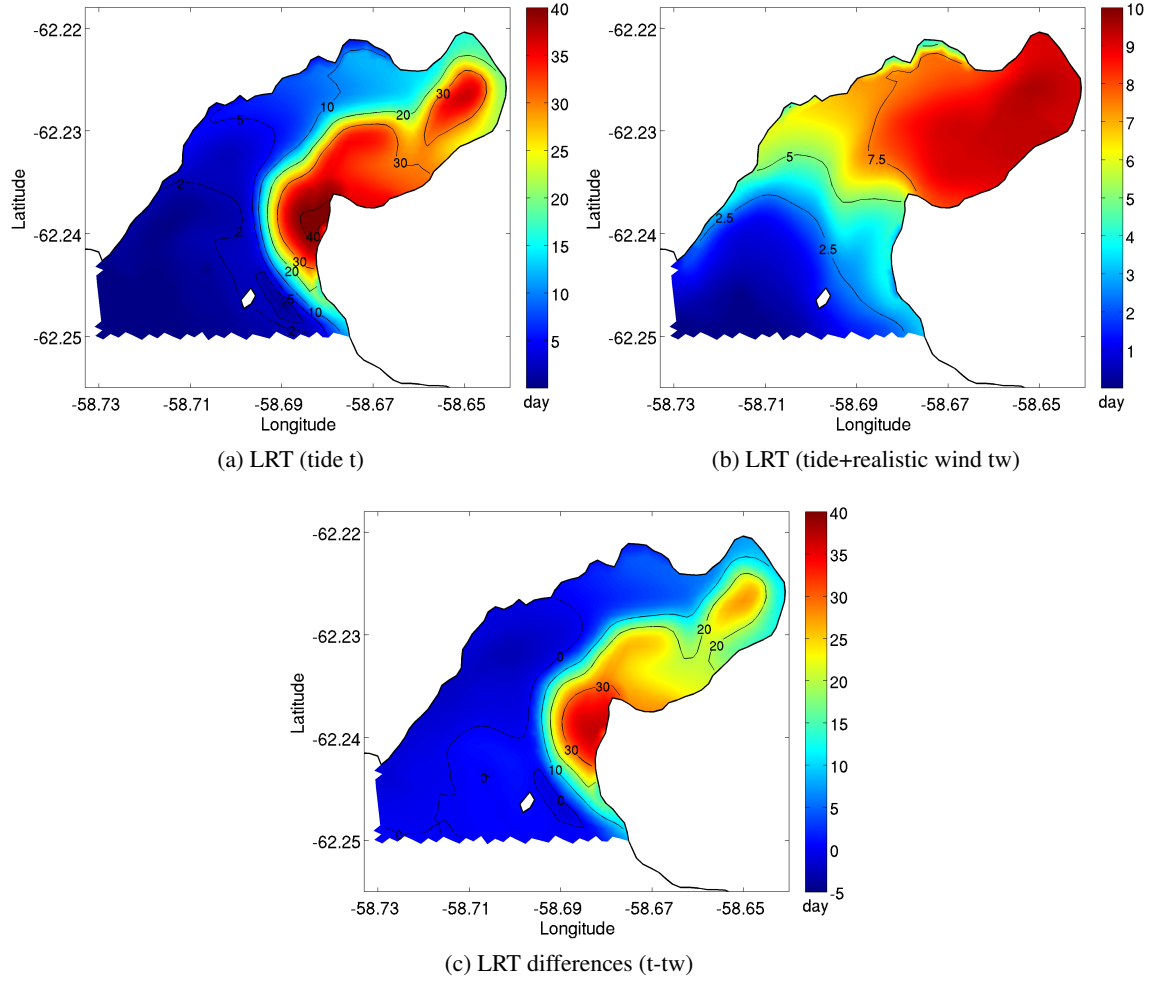


(c) LRT differences (t-tw)

Figure 6.5: LRT distributions with only tidal forcing (a), and combined tidal and wind forcings (b). Differences in LRT (c). LRTs were estimated based on the exponential fit method. Notice that (a) and (b) have different legends for the colour scale. Negative values in (c) indicate that the LRT is longer in the presence of winds.

the effect of combined tides and winds, it is found that the LRT values are rather evenly distributed within the cove and the LRTs become longer as the distance from the boundary increases (Fig. 6.5b). The LRTs grow gradually to a maximum of about 10 days in the inner cove and the maximum values generally cover a vast area within the inner cove near the Potter Peninsula side.

Comparing the LRTs under the two different forcing conditions (with and without the wind forcing), differences of the LRT, i.e. LRT(tide) - LRT(tide+wind), around Mirounga Point are particularly discernible (Fig. 6.5c). In the outer cove, the differences can be as high as 36.8 days at the southwestern side of Mirounga Point. The LRT values in this region decrease nearly tenfold in the presence of winds. Winds have also greatly influenced the LRTs in the central part of the far inner cove, with the LRTs being about 3-3.5 times shorter when compared to the LRTs under

tidal forcing. The differences vary between 20-25 days. The results have shown that winds have a significant influence on the temporal behaviour of water transport in Potter Cove.

### 6.1.3   Influence of tides and northwesterly winds

As the typical predominant wind direction at Potter Cove is from the NW-W quadrant and the most frequent wind intensities are between 8 and 12 m/s (Schloss and Ferreyra, 2002) with an average wind speed of about 10 m/s (Klöser et al., 1994; Schloss et al., 2002), two different scenarios, (i) tides and NW wind with 10 m/s (denoted as tide+NW10), and (ii) tide and W wind with 10 m/s (denoted as tide+W10), were used to force the model. These idealized numerical experiments were performed to compare the influence of tides and constant wind from two dominant directions on water transport time scales. The case with the first scenario (tide+NW10) will be presented in this section and the second scenario (tide+W10) will be reported in Section 6.1.4.

In order to obtain the e-folding time, the concentration decay on each node were fitted with an exponential function. Fig. 6.6a shows an example at a location where the exponential curve fits the concentration results very well. Under the influence of tide+NW10 wind, the LRT in the cove generally increases with the distance towards the inner cove with a maximum LRT of approximately 10 days at the far inner cove (Fig. 6.6b). The distributions of tracer concentration over time can be seen in Fig. 6.7. It shows how concentration alters during the course of less than two weeks.

### 6.1.4   Influence of tides and westerly winds

As for the scenario with tide+W10 wind, the exponential function also fits the concentration results very well (Fig. 6.6c). Under the tide+W10 wind condition, the spatial distribution and magnitude of LRTs change dramatically when compared to the first scenario with tide+NW10 wind (see Figs. 6.6b and 6.6d for comparison). The 'new water' is able to flush the upper half of the cove water in less than 2 days (Fig. 6.8). The LRT values are in the range between 2 to 2.8 days at the lower half of the cove. The results have apparently shown that the direction of predominant wind plays an important role in water transport in Potter Cove.

## 6.2   Flushing time

Two methods were used to calculate the flushing time scales. The first method is rather straightforward, i.e. by calculating the mean of all LRTs over the domain of interest. The second method is based on the concept of the remnant function proposed by Takeoka (1984).

(a) Exponential fit (tide+NW10 wind)

(b) LRT (tide+NW10 wind)

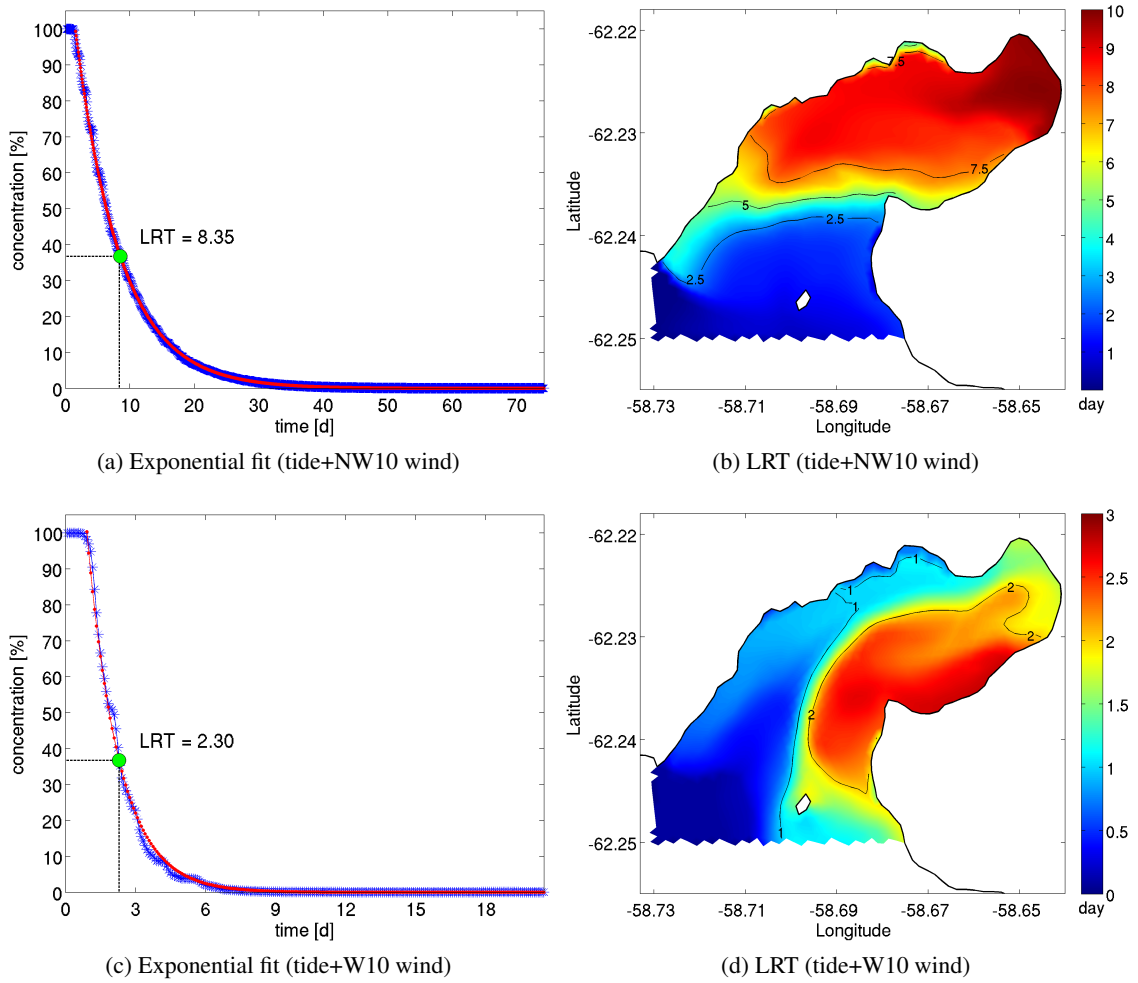(c) Exponential fit (tide+W10 wind)

(d) LRT (tide+W10 wind)

Figure 6.6: LRT estimation method and their corresponding spatial distributions. Scenario 1: tide+NW10 wind (upper) and scenario 2: tide+W10 wind (lower). The blue asterisks (*) represent the FVCOM modelled concentration. The red line shows the exponential fit. Notice that (b) and (d) have different legends for the colour scale.

### 6.2.1 Arithmetic mean of LRTs

Because flushing time is an overall (integrative) system measure, a simple arithmetic mean or an average of all LRTs over the cove can be calculated as the flushing time for Potter Cove. The results are summarized in Table 6.1 according to the moving average ($m$1, $m$61 and $m$91) and exponential fit methods for the forcing conditions: (i) tide only, and (ii) tide+realistic wind. For (iii) tide+NW10 wind, and (iv) tide+W10 wind conditions, because the exponential function fits the concentration results very well, only the exponential fit method was used to obtain the LRTs and the mean LRTs or flushing time for Potter Cove. $m$91 takes a moving average of 91 data points (covering 7.5-day data).

With only tidal forcing, the flushing times are in the range of 9.8 to 13.2 days. The flushing
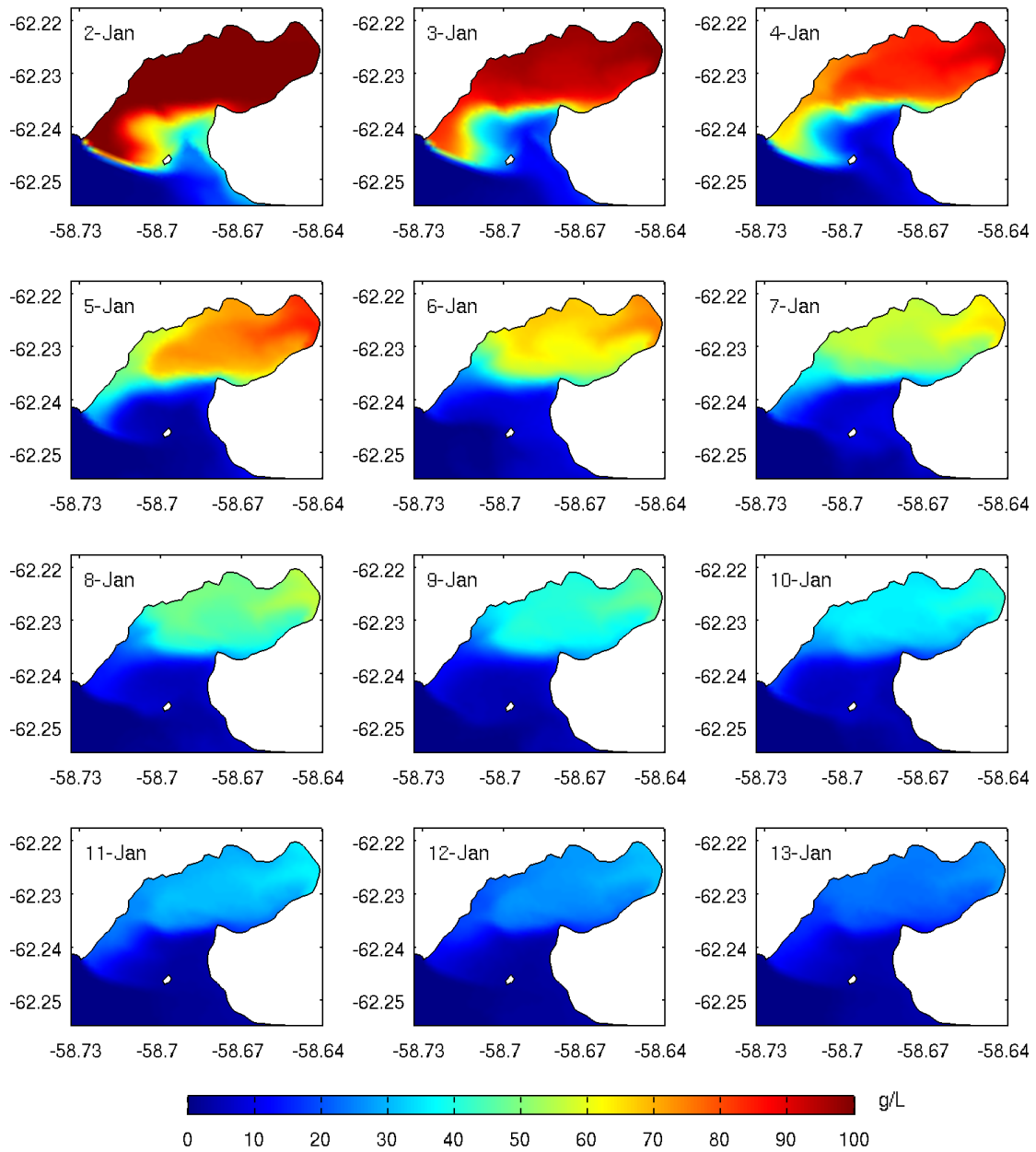
98

Figure 6.7: Temporal and spatial distributions of tracer concentration at the surface layer (combined tidal and NW10 wind forcings). Tracer release time: 01-Jan-1999 00:00:00 UTC.
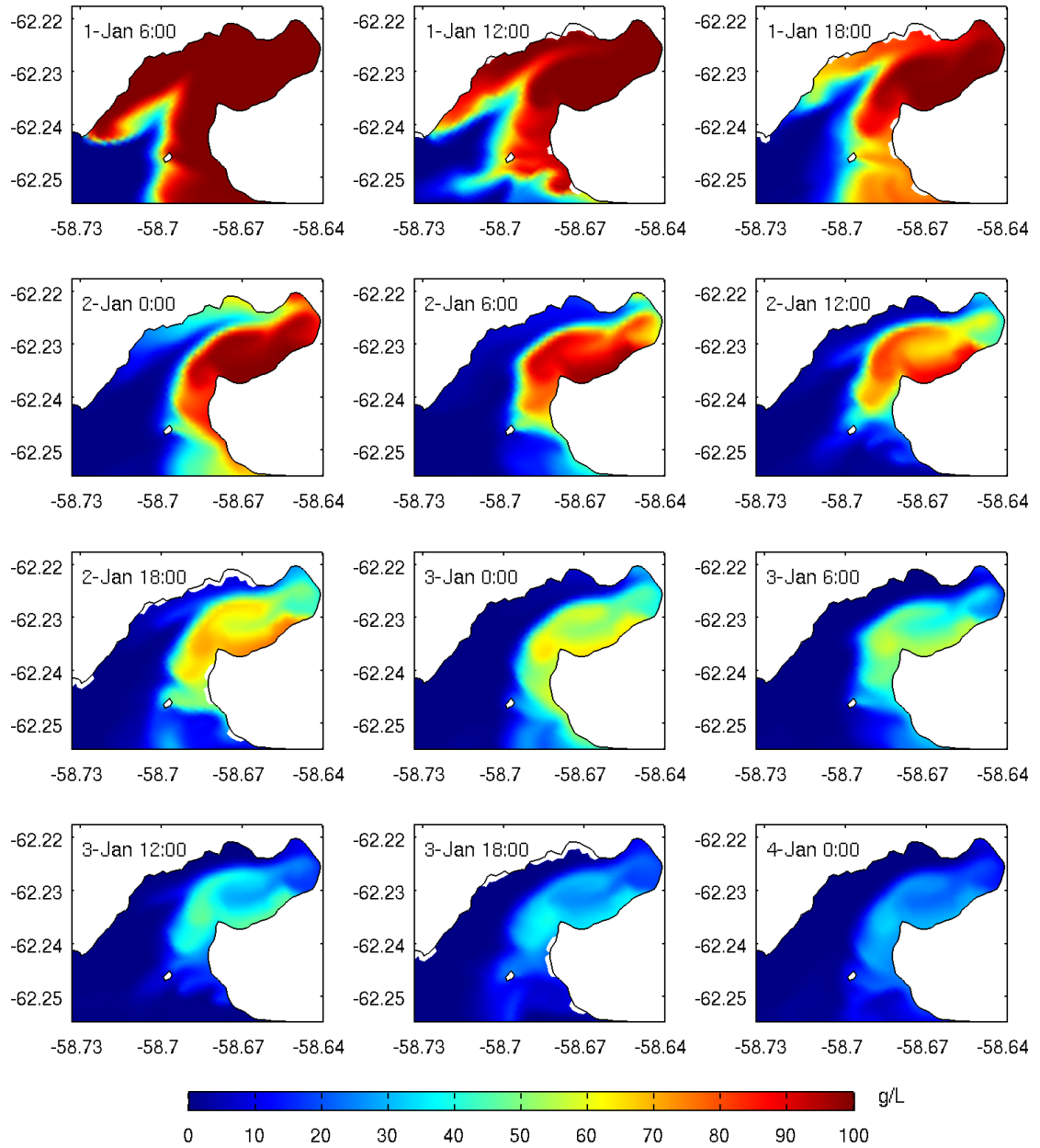
Figure 6.8: Temporal and spatial distributions of tracer concentration at the surface layer (combined tidal and W10 wind forcings). Tracer release time: 01-Jan-1999 00:00:00 UTC.

Table 6.1: Flushing times (in days) based on the arithmetic mean for different forcing scenarios

| Curve fitting method | Tide | Tide+realistic wind | Tide+NW10 | Tide+W10 |
|---|---|---|---|---|
| 1. Moving average $m1$ | 9.8 | 4.1 | | |
| 2. Moving average $m61$ | 11.5 | 5.2 | | |
| 3. Moving average $m91$ | 11.6 | 5.1 | | |
| 4. Exponential fit | 13.2 | 5.1 | 5.4 | 1.4 |

times decrease dramatically to 4.1-5.2 days if the combined tidal and realistic wind forcings are imposed. According to Schloss et al. (1997), a particle or a phytoplankton cell may stay in Potter Cove for about four days under mean summer conditions. This correlates with the calculated flushing times in this study. Under tide+NW10 and tide+W10 wind conditions, the flushing times are estimated to be 5.4 and 1.4 days, respectively.

### 6.2.2 Remnant function

In order to describe the water transport and exchange characteristics of Potter Cove, alternatively, the concept of remnant function after Takeoka (1984) is applied. The remnant function $r(t)$ is defined as the ratio of the total mass of tracer within the water system at a given time, $m(t)$, to the initial mass of the tracer, $m_0$:

$$r(t) = \frac{m(t)}{m_0} \tag{6.5}$$

The remnant function considers the temporal decline of the total mass in Potter Cove, therefore the flushing time or average residence time (ART) can be calculated as an integral of the remnant function:

$$ART = \int_0^\infty r(t)\, dt \tag{6.6}$$

In Fig. 6.9, the remnant function $r(t)$ is plotted against the time for various forcing conditions. By integrating the remnant function over time (green shaded area) using Simpson's rule, the ARTs are computed to be 8.5, 3.2, 4.0 and 1.0 days for various scenarios: (i) tide only, (ii) tide+realistic wind, (iii) tide+NW10 wind, and (iv) tide+W10 wind, respectively. The results are tabulated in Table 6.2.

(a) ART (tide)

(b) ART (tide+realistic wind)

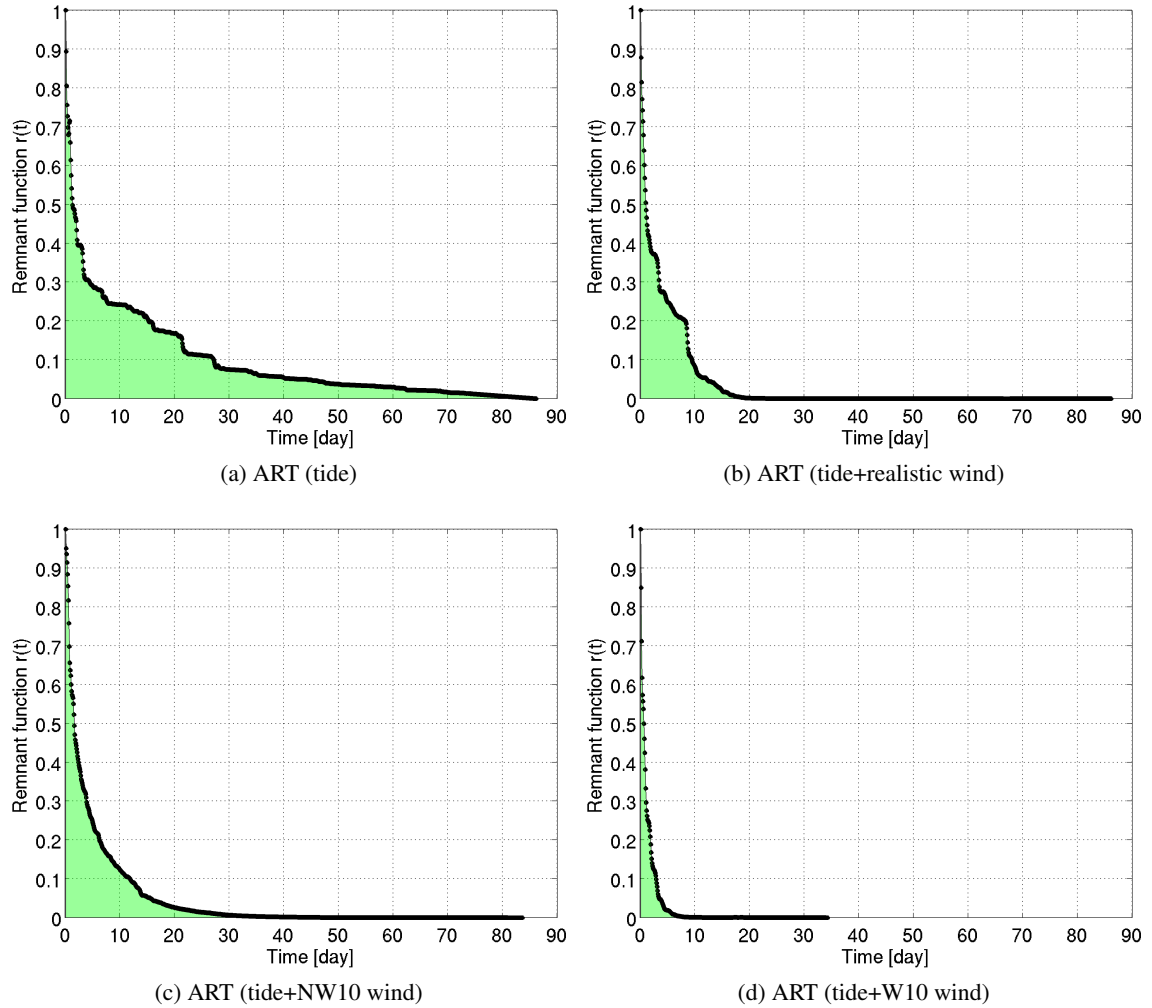(c) ART (tide+NW10 wind)

(d) ART (tide+W10 wind)

Figure 6.9: ART estimation using remnant function $r(t)$ for different forcing scenarios.

Table 6.2: ART based on the remnant function concept for different forcing scenarios

| Forcing scenario | ART (day) |
|---|---|
| Tide | 8.5 |
| Tide+realistic wind | 3.2 |
| Tide+NW10 wind | 4.0 |
| Tide+W10 wind | 1.0 |

102

# Chapter 7

# Summary

Potter Cove, which comprises of water depths of a few meters along the coast to hundreds of meters near the mouth, has been one of the most popular research locations on King George Island, South Shetland Islands, Antarctica. Growing interest among Antarctic scientists in wave conditions and current circulations in Potter Cove has led to the present numerical modelling study to provide insights into the wave dynamics and hydrodynamics in Potter Cove as well as their interactions with the surrounding environments. The SWAN and FVCOM models were successfully implemented to model the wave evolution and hydrodynamic circulations for an austral summer month. The wave generation and propagation schemes in SWAN generally provide fairly reasonable results in terms of significant wave height when compared to the NDBC observations. Wave fields from storms in the ocean are generally well reproduced by the SWAN model, with an occassional underprediction in significant wave heights, depending on the observation locations. Qualitative comparisons of SWAN computed $H_s$ time series and contours with WW3 results appear to be consistent. Further assessment of a smaller nested model for the South Shetland Islands region indicates a good agreement between the model and the GlobWave satellite altimeter data.

The results revealed that although the wave conditions in the open ocean such as Drake Passage may result in an increase of significant wave height in Bransfield Strait, they have no significant influence on the wave conditions in Potter Cove, which are rather dependent on the local wind conditions. The results also form a basis to provide a general overview on the geographical distributions of significant wave height for various wind conditions that range from light over moderate to strong wind conditions. In general, the significant wave heights at the inner cove were found to be about 40-50% smaller than the ones near the opening of Potter Cove. Analyses on the model results for the summer month indicate that the predominant incoming waves entering Potter Cove were typically coming from the S-SW quadrant with $H_s$ varying between 0.4-0.7 m and $T_p$ of about 3.5-4.5 s. The wave power in Potter Cove is generally low, with the modelled energetic peak of about 7 kW/m located at the deeper water areas near the opening of Potter Cove.

Most of the wave energy is dissipated through bottom friction and depth-induced wave breaking in shallow water areas around Winship Point, along the northern coastal water of Potter Cove,

and the western and southern coastal areas along the perimeter of Potter Peninsula. The contribution of dissipation due to whitecapping is largely found in deeper water near the opening and offshore of the cove. The SWAN wave modelling system covering the entire world ocean has been successfully used to simulate waves of oceanic scales. This allows simulations between a large scale model and nearshore computations through a nesting approach to be carried out entirely based on a single wave model. With an optimization on the whitecapping term, the SWAN model, which was originally developed for coastal applications, provides an extensive modelling package for wave simulations from deep ocean to the nearshore through comprehensive parameterizations.

The most dominant tidal constituent in the study area is $M_2$. In general, tides propagate from the Weddell Sea, enter the Bransfield Strait and move further southwestward. Tidal amplitudes of the semi-diurnal constituents, especially the $M_2$, are larger at the eastern side of the Northern Antarctic Peninsula in the Weddell Sea than in the Bransfield Strait and Bellingshausen Sea. The diurnal tidal amplitudes increase gradually from the King George Island to the Antarctic Peninsula. Through the tidal harmonic analysis and the construction of the cotidal and corange charts in this study, a more thorough understanding of the tidal dynamics in the Northern Antarctic Peninsula can be achieved. The tidal regime is mixed, predominantly semi-diurnal in Potter Cove with the calculated mean neap and spring tide ranges of about 0.40 m and 1.36 m, respectively.

Multiscale model simulations performed for the austral summer 1999 have revealed the relative importance of tides, winds and waves on the circulation patterns in the study area. Modelled tidal currents appear to be significant in the proximity of the opening of Maxwell Bay. In contrast, tides have minimal influence on the circulation in Potter Cove. The tide-induced currents in Potter Cove are generally low, with relatively stronger tidal current occurence during spring tide. Wind plays a more significant role in the circulation patterns in Potter Cove and the circulation patterns are highly dependent on the wind speed and direction. Wind generally strengthens the surface flow. The northwesterly winds drive surface water into the cove. The incoming waters generally travel along the northern and southern coasts and the outflow leaves the cove along the central region. The southwesterly winds generate a cyclonic circulation where the waters enter the cove through the northern sector and exit through the southern sector. Time series analyses further demonstrate that the current regime off Potter Cove is rather tide-dominated while the flow patterns due to the combined action of tides and winds in Potter Cove exhibit trends and periodicities that are congruent to the wind-induced currents, indicating wind-dominated circulation in Potter Cove.

The wave contribution to the flow in Potter Cove is prominent and a genereal cyclonic circulation can be observed with a gyre occurs at the inner cove under the combined action of tides, winds and waves. Under wave-current interaction, the wave-induced longshore currents are significant, especially during strong wind conditions where sea states are rough. This is evident along the northern coast as well as the western and southern perimeter of Potter Peninsula. An entering longshore current along a narrow littoral strip in the southern coast is also observed. In general,

the circulation in Potter Cove follows the meanders of the seafloor topography. The hydrodynamic simulations using FVCOM together with its wave module FVCOM-SWAVE for wave-current interaction have provided a basis to the understanding of a small-scale hydrodynamic circulation in Potter Cove. Future investigations should consider other forcings such as temperature, salinity and glacial meltwater inputs that might affect the circulation in Potter Cove. The spatial characteristics of the active energy dissipation follows the pattern of the seafloor topography.

The outputs of the hydrodynamic and wave modellings using FVCOM-SWAVE and SWAN allow the calculations of skin friction bed shear stresses by taking into account the effects of currents and waves as the forcing agents. The results suggest that the wave-induced bed shear stress is a potential major driving force for the bed sediment erosion and resuspension of fine-grained soil in Potter Cove, especially in shallow water regions. The spatial characteristics of the wave-induced bed shear stress follows the pattern of the seafloor topography. On the contrary, the bed shear stress due to currents was found to be less significant for the initiation of sediment motion in Potter Cove. The area around Winship Point, waters along the northern coast of Potter Cove, and the western and southern coast of Potter Peninsula are identified as bed erosion prone regions. The interpretation of the results of the bed shear stress (or bed erosion prone regions) is supported by a seafloor habitat map (Hass et al., 2013) and in line with the findings by Quartino and Boraso de Zaixso (2008). For future detailed investigations, a coupled wave, current and sediment-transport model should be used and full sediment fractions for Potter Cove should be taken into account whenever sediment data is available. The results of the present work on the bed shear stress serve as an initial estimate to address the potential bed erosion characteristics in Potter Cove.

The residence time following an Eulerian approach to quantify the spatio-temporal behaviour of water masses in Potter Cove was estimated. Under the tidal circulation, the external waters initially entered and flushed the upper half of the cove and subsequently replaced the highly concentrated waters near the Potter Peninsula side. The local residence time (LRT) values increase toward the interior of the cove, along the northern sector of the cove, to approximately 20 days. The LRTs for the southern sector of the cove are in the range of 20 to 35 days or even larger. Under the combined action of tides and realistic winds, the LRTs increase gradually to a maximum of about 10 days in the inner cove and the maximum values generally cover a vast area within the inner cove near the Potter Peninsula side. In general, the LRTs become longer as the distance from the boundary increases. A comparison on the influence of constant wind from two dominant directions together with the presence of tides indicates that the direction of predominant wind plays an important role in water transport in Potter Cove. With only tidal forcing, the flushing times are in the range of 9.8 to 13.2 days, based on the arithmetic mean of LRTs, and 8.5 days, based on the remnant function concept by Takeoka (1984). For the case under the combined action of tides and realistic winds, the flushing times are estimated to be in the range of 4.1 to 5.2 days (arithmetic mean of LRTs) and 3.2 days (remnant function concept).

# References

Abdelrhman MA (2002) Modeling how a hurricane barrier in New Bedford Harbor, Massachusetts, affects the hydrodynamics and residence times. Estuaries 25(2):177-196. 90, 91

Abdelrhman MA (2005) Simplified modeling of flushing and residence times in 42 embayments in New England, USA, with special attention to Greenwich Bay, Rhode Island. Est Coastal Shelf Sci 62:339-351. 90

Amante C, Eakins BW (2009) ETOPO1 1 arc-minute Global Relief Model: procedures, data sources and analysis. NOAA Technical Memorandum NESDIS NGDC-24, p 19. 15

Antarctic Place-names Committee, Foreign and Commonwealth Office (2009a) South Shetland Islands: Greenwich, Robert and Nelson Islands [map]. 9th ed. 1:100,000. APC Misc 65. London: Antarctic Place-names Committee, Foreign and Commonwealth Office. 14

Antarctic Place-names Committee, Foreign and Commonwealth Office (2009b) South Shetland Islands: King George Island [map]. 11th ed. 1:100,000. APC Misc 64. London: Antarctic Place-names Committee, Foreign and Commonwealth Office. 14

Antarctic Place-names Committee, Foreign and Commonwealth Office (2010) South Shetland Islands: King George Island, Fildes Peninsula [map]. 2nd ed. 1:25,000. APC Misc 85. London: Antarctic Place-names Committee, Foreign and Commonwealth Office. 14

Battjes JA, Janssen JPFM (1978) Energy loss and set-up due to breaking of random waves. Proc 16th Int Conf on Coastal Eng, ASCE:569-587. 9

Blumberg AF, Mellor GL (1987) A description of a three-dimensional coastal ocean circulation model. In: Heaps NS (ed) Three-dimensional coastal ocean models. American Geophysical Union, Washington, DC, p 1-16. 39

Booij N, Ris RC, Holthuijsen LH (1999) A third-generation wave model for coastal regions 1. Model description and validation. J Geophys Res 104(C4):7649-7666. 2, 8

Breivik Ø, Gusdal Y, Furevik BR, Aarnes OJ, Reistad M (2009) Nearshore wave forecasting and hindcasting by dynamical and statistical downscaling. J Marine Syst 78:S235-S243. 12

BS EN ISO 14688-1 (2002) Geotechnical investigation and testing. Identification and classification of soil. Identification and description. British Standards Institution, London, p 22. 81

Cavaleri L, Malanotte-Rizzoli P (1981) Wind wave prediction in shallow water: Theory and applications. J Geophys Res 86(C11):10961-10973. 9

Chang KI, Jun HK, Park GT, Eo YS (1990) Oceanographic conditions of Maxwell Bay, King George Island, Antarctica (austral summer 1989). Korean J of Polar Res 1:27-46. 48

Chen C, Beardsley RC, Cowles G (2006) An unstructured grid, finite-volume coastal ocean model: FVCOM user manual. School for Marine Science and Technology, University of Massachusetts-Dartmouth, New Bedford, p 315. 34, 38

Chen C, Huang H, Beardsley RC, Liu H, Xu Q, Cowles G (2007) A finite volume numerical approach for coastal ocean circulation studies: Comparisons with finite difference models. J Geophys Res 112:C03018. 34

Chen C, Liu H, Beardsley RC (2003) An unstructured grid, finite-volume, three-dimensional, primitive equations ocean model: Application to coastal ocean and estuaries. J Atmos Oceanic Technol 20:159-186. 34

Chen Y, Pan S, Wolf J, Du Y (2010) Downscaling effects on modelling waves, tides and storm surge. Coast Eng Proc 1(32):waves.33. 12

Cucco A, Umgiesser G (2006) Modeling the Venice Lagoon residence time. Ecol Model 193(1-2):34-51. 90

Cucco A, Umgiesser G, Ferrarin C, Perilli A, Canu DM, Solidoro C (2009) Eulerian and Lagrangian transport time scales of a tidal active coastal basin. Ecol Model 220(7):913-922. 90

D'Onofrio EE, Dragani WC, Speroni JO, Fiore MME (2003) Propagation and amplification of tide at the northeastern coast of the Antarctic Peninsula: An observational study. Polar Geosci 16:53-60. 41, 43

Dragani WC, Drabble MR, D'Onofrio EE, Mazio CA (2004) Propagation and amplification of tide at the Bransfield and Gerlache Straits, northwestern Antarctic Peninsula. Polar Geosci 17:156-170. 41, 48

Earle MD (1984) Development of algorithms for separation of sea and swell. National Data Buoy Center Tech Rep MEC-87-1, p 53. 26

Eraso A, Dominguez C (2007) Physicochemical characteristics of the subglacier discharge in Potter Cove, King George Island, Antarctica. In: Tyk A, Stefaniak K (eds): Karst and cryokarst, studies of the Faculty of Earth Sciences, University of Silesia 45:111-122. 7

## REFERENCES

Gaslikova L, Weisse R (2006) Estimating near-shore wave statistics from regional hindcasts using downscaling techniques. Ocean Dyn 56:26-35. 12

Geuzaine C, Remacle J-F (2009) Gmsh: A 3-D finite element mesh generator with built-in pre- and post-processing facilities. Int J Numer Meth Eng 79:1309-1331. 34

Griffith TW, Anderson JB (1989) Climatic control of sedimentation in bays and fjords of the Northern Antarctic Peninsula. Mar Geol 85:181-204. 7

Hartnett M, Gleeson F, Falconer R, Finegan M (2003) Flushing study assessment of a tidally active coastal embayment. Adv Environ Res 7(4):847-857. 90

Hass HC, Kuhn G, Wölfl A-C, Wittenberg N, Deregibus D, Quartino LM, Tosonotto G, Sahade R, Lindhorst S, Roberts SJ, Braun M, Monien P, Monien D, Lim CH, Strelin J, Fuentes V (2013) The coastal depositional environment in KGI fjord and bay systems. In: Abele D (ed) Impact of climate induced glacial melting on marine coastal systems in the Western Antarctic Peninsula region (IMCOAST). Alfred Wegener Institute for Polar and Marine Research (AWI), Bremerhaven, Germany. Unpublished report. 1, 81, 86, 87, 105

Hasselmann K, Barnett TP, Bouws E, Carlson H, Cartwright DE, Enke K, Ewing JA, Gienapp H, Hasselmann DE, Kruseman P, Meerburg A, Müller P, Olbers DJ, Richter K, Sell W, Walden H (1973) Measurements of wind-wave growth and swell decay during the Joint North Sea Wave Project (JONSWAP), Dtsch Hydrogr Z Suppl 12(A8), p 95. 9, 11

Hemer MA (2006) The magnitude and frequency of combined flow bed shear stress as a measure of exposure on the Australian continental shelf. Cont Shelf Res 26:1258-1280. 2

Holthuijsen LH (2007) Waves in oceanic and coastal waters. Cambridge University Press, Cambridge, p 387. 8, 9, 71, 76

Kahma KK, Calkoen CJ (1992) Reconciling discrepancies in the observed growth of wind-generated waves. J Phys Oceanogr 22:1389-1405. 16

Kalnay E, Kanamitsu M, Kistler R, Collins W, Deaven D, Gandin L, Iredell M, Saha S, White G, Woollen J, Zhu Y, Chelliah M, Ebisuzaki W, Higgins W, Janowiak J, Mo KC, Ropelewski C, Wang J, Leetmaa A, Reynolds R, Jenne R, Joseph D (1996) The NCEP/NCAR 40-year reanalysis project. Bull Amer Meteor Soc 77(3):437-471. 15, 38

Klöser H, Ferreyra G, Schloss I, Mercuri G, Laturnus F, Curtosi A (1994) Hydrography of Potter Cove, a small fjord-like inlet on King George Island (South Shetlands). Estuar Coast Shelf Sci 38:523-537. 3, 7, 55, 84, 97

Komen GJ, Hasselmann S, Hasselmann K (1984) On the existence of a fully developed wind-sea spectrum. J Phys Oceanogr 14:1271-1285. 9, 10, 11

Kumar N, Voulgaris G, Warner JC (2011) Implementation and modification of a three-dimensional radiation stress formulation for surf zone and rip-current applications. Coast Eng 58:1097-1117. 76

Large WG, Pond S (1981) Open ocean momentum flux measurements in moderate to strong wind. J Phys Oceanogr 11:324-336. 38

Lettmann KA, Wolff J-O, Badewien TH (2009) Modeling the impact of wind and waves on suspended particulate matter fluxes in the East Frisian Wadden Sea (southern North Sea). Ocean Dyn 59(2):239-262. 29, 82

Liu AK, Jackson FC, Walsh EJ (1989) A case study of wavecurrent interaction near an oceanic front. J Geophys Res 94(C11):16189-16200. 15

Longuet-Higgins MS, Stewart RW (1964) Radiation stresses in water waves; a physical discussion, with applications. Deep-Sea Res 11:529-562. 71

López O, García MA, Arcilla AS (1994) Tidal and residual currents in the Bransfield Strait, Antarctica. Annales Geophysicae 12(9):887-902. 48

Lyard F, Lefevre F, Letellier T, Francis O (2006) Modelling the global ocean tides: modern insights from FES2004. Ocean Dyn 56:394-415. 38

Mellor G (2013) Waves, circulation and vertical dependence. Ocean Dyn 63:447-457.

Mellor GL (2003) The three-dimensional current and surface wave equations. J Phys Oceanogr 33:1978-1989. 76

Mellor GL (2005) Some consequences of the three-dimensional currents and surface wave equations. J Phys Oceanogr 35:2291-2298. 76

Mellor GL (2008) The depth-dependent current and wave interaction equations: A revision. J Phys Oceanogr 38:2587-2596. 76

Mellor GL, Yamada T (1982) Development of a turbulence closure model for geophysical fluid problems. Rev Geophys Space Phys 20:851-875. 34

Monien P, Schnetger B, Brumsack H-J, Hass HC, Kuhn G (2011) A geochemical record of late Holocene palaeoenvironmental changes at King George Island (maritime Antarctica). Antarct Sci 23(3):255-267. 82

Monsen NE, Cloern JE, Lucas LV, Monismith SG (2002) A comment on the use of flushing time, residence time, and age as transport time scales. Limnol Oceanogr 47:1545-1553. 89

Mori N, Yasuda T, Mase H, Tom T, Oku Y (2010) Projection of extreme wave climate change under global warming. Hydrol Res Lett 4:15-19. 1

## REFERENCES

Ortiz-Royero JC, Mercado-Irizarry A (2008) An intercomparison of SWAN and WAVEWATCH III models with data from NDBC-NOAA buoys at oceanic scales. Coast Eng J 50:47-73. 2, 14

Pawlowicz R, Beardsley B, Lentz S (2002) Classical tidal harmonic analysis including error estimates in MATLAB using T_TIDE. Comput Geosci 28:929-937. 41

Pierson WJ, Moskowitz L (1964) A proposed spectral form for fully developed wind seas based on the similarity theory of S. A. Kitaigorodskii. J Geophys Res 69(24):5181-5190. 10, 26

Portilla J, Ocampo-Torres FJ, Monbaliu J (2009) Spectral partitioning and identification of wind sea and swell. J Atmos Oceanic Technol 26(1):107-122. 26

Pugh DT (1987) Tides, surges and mean sea-level: A handbook for engineers and scientists. John Wiley & Sons Ltd, Chichester, p 472. 41

Qi J, Chen C, Beardsley RC, Perrie W, Cowles GW, Lai Z (2009) An unstructured-grid finite-volume surface wave model (FVCOM-SWAVE): Implementation, validations and applications. Ocean Model 28:153-166. 36

Quartino ML, Boraso de Zaixso AL (2008) Summer macroalgal biomass in Potter Cove, South Shetland Islands, Antarctica: its production and flux to the ecosystem. Polar Biol 31(3):281-294. 87, 105

Reeve D, Chadwick A, Fleming C (2004) Coastal engineering: processes, theory and design practice. Spon Press, Oxon, p 461. 41, 80

Robertson R, Padman L, Gary DE (1998) Tides in the Weddell Sea. In: Jacobs SS, Weiss RF (eds), Ocean, Ice, and Atmosphere: Interactions at the Antarctic Continental Margin. Antarct Res Ser 75:341-369. 48

Roese M, Drabble M (1998) Wind-driven circulation in Potter Cove. In: Wiencke C, Ferreyra G, Arntz W, Rinaldi C (eds) The Potter Cove coastal ecosystem, Antarctica. Ber. Polarforsch 299:40-46. 3, 7, 55, 84

Rusu E (2011) Strategies in using numerical wave models in ocean/coastal applications. J Mar Sci Technol 19(1):58-75. 2, 18

Sanford LP, Boicourt WC, Rives SR (1992) Model for estimating tidal flushing of small embayments. J Waterw Port Coastal Ocean Eng 118:635-654. 89

Schloss IR, Abele D, Moreau S, Demers S, Bers A.V, González O, Ferreyra GA (2012) Response of phytoplankton dynamics to 19-year (1991-2009) climate trends in Potter Cove (Antarctica). J Marine Syst 92:53-66. 7, 84

Schloss IR, Ferreyra GA (2002) Primary production, light and vertical mixing in Potter Cove, a shallow bay in the maritime Antarctic. Polar Biol 25:41-48. 7, 84, 97

Schloss IR, Ferreyra GA, Ruiz-Pino D (2002) Phytoplankton biomass in Antarctic shelf zones: a conceptual model based on Potter Cove, King George Island. J Marine Syst 36:129-143. 7, 62, 97

Schloss IR, Klöser H, Ferreyra GA, Mercuri G, Pinola E (1997) Factors governing phytoplankton and particulate matter variation in Potter Cove, King George Island, Antarctica. In: Battaglia B, Valencia J, Walton DWH (eds) Antarctic communities. Cambridge University Press, Cambridge, UK:135-141. 3, 62, 101

Schöne T, Pohl M, Zakrajsek AF, Schenke HW (1998) Tide gauge measurements - A contribution for the long term monitoring of the sea level. In: Wiencke C, Ferreyra GA, Arntz W, Rinaldi C (eds), The Potter Cove coastal ecosystem, Antarctica. Ber Polarforsch:12-14. 41, 43

Smagorinsky J (1963) General circulation experiments with the primitive equations I. The basic experiment. Mon Weather Rev 91(3):99-164. 34

Soulsby R (1997) Dynamics of marine sands. Thomas Telford Publications, London, p 249. 80, 81, 82, 83

Stanev EV, Kandilarov R (2012) Sediment dynamics in the Black Sea: numerical modelling and remote sensing observations. Ocean Dyn 62:533-553. 80, 82

Stanev EV, Wolff J-O, Brink-Spalink G (2006) On the sensitivity of the sedimentary system in the East Frisian Wadden Sea to sea-level rise and wave-induced bed shear stress. Ocean Dyn 56:266-283. 80, 82

Stopa JE, Filipot J-F, Li N, Cheung KF, Chen Y-L, Vega L (2013) Wave energy resources along the Hawaiian Island chain. Renew Energ 55:305-321. 12

Svendsen IA (2006) Introduction to nearshore hydrodynamics. World Scientific, Singapore, p 722. 71

SWAN Team (2011a) SWAN Cycle III version 40.85 scientific and technical documentation. Delft University Technology, Faculty of Civil Engineering and Geosciences, Environmental Fluid Mechanics Section, P.O. Box 5048, 2600 GA Delft, The Netherlands, p 118. 9

SWAN Team (2011b) SWAN Cycle III version 40.85 user manual. Delft University Technology, Faculty of Civil Engineering and Geosciences, Environmental Fluid Mechanics Section, P.O. Box 5048, 2600 GA Delft, The Netherlands, p 121. 9, 19

Takeoka H (1984) Fundamental concepts of exchange and transport time scales in a coastal sea. Cont Shelf Res 3:311-326. 97, 101, 105

# REFERENCES

Tolman HL (1997) User manual and system documentation of WAVEWATCH-III version 1.15. NOAA/NWS/NCEP/OMB Technical Note 151, p 97. 2

Tolman HL (1999) User manual and system documentation of WAVEWATCH-III version 1.18. NOAA/NWS/NCEP/OMB Technical Note 166, p 110. 2

Tolman HL (2009) User manual and system documentation of WAVEWATCH III version 3.14. NOAA/NWS/NCEP/MMAB Technical Note 276, p 194. 2

Turner J, Colwell SR, Marshall GJ, Lachlan-Cope TA, Carleton AM, Jones PD, Lagun V, Reid PA, Iagovkina S (2005) Antarctic climate change during the last 50 years. Int J Climatol 25:279-294. 1

Varela L (1998) Hydrology of Matias and Potter Cove. In: Wiencke C, Ferreyra G, Arntz W, Rinaldi C (eds) The Potter Cove coastal ecosystem, Antarctica. Ber. Polarforsch 299:33-39. 7

Vodopivez C, Smichowski P, Marcovecchio J (2001) Trace metals monitoring as a tool for characterization of Antarctic ecosystems and environmental management. The Argentine programme at Jubany Station. In: Caroli S, Cescon P, Walton DWH (eds) Environmental contamination in Antarctica: A challenge to analytical chemistry. Elsevier Sciece, Oxford, UK:155-180. 62, 77

WAMDI Group (1988) The WAM model - a third generation ocean wave prediction model. J Phys Oceanogr 18:1775-1810. 2, 9, 10

Whitehouse R, Soulsby R, Roberts W, Mitchener H (2000) Dynamics of estuarine muds. Thomas Telford Publishing, London, p 210. 81, 82

Willmott CJ (1981) On the validation of models. Phys Geog 2:187-194. 17

Willmott CJ (1982) Some comments on the evaluation of model performance. Bull Amer Meteor Soc 63(11):1309-1313. 17

Wornom SF, Allard R, Hsu YL (2002) An MPI quasi time-accurate approach for nearshore wave prediction using the SWAN code. Part II: Applications to wave hindcasts. Coast Eng J 44:257-280. 17

Wu J (1982) Wind-stress coefficients over sea surface from breeze to hurricane. J Geophys Res 87(C12):9704-9706. 10

Wu L, Chen C, Guo P, Shi M, Qi J, Ge J (2011) A FVCOM-based unstructured grid wave, current, sediment transport model, I. Model description and validation. J Ocean Univ China 10:1-8. 36, 76

Yapo PO, Gupta HV, Sorooshian S (1996) Automatic calibration of conceptual rainfall-runoff models: sensitivity to calibration data. J Hydrol 181:23-48. 17

# Acknowledgements

# Curriculum vitae

## Personal Details

| | |
|---|---|
| Family name | Lim |
| Given name | Chai Heng |
| Date & place of birth | 28.09.1979, Malacca, Malaysia |
| Nationality | Malaysian |

## Contact Information

| | |
|---|---|
| Address | 10, Jalan Pandan Mawar 3, Taman Pandan Mawar |
| | Jalan Datuk Wira Poh Ah Tiam, 75250 Malacca |
| | Malaysia |
| E-mail | chaiheng753@yahoo.com |

## Academic Qualifications

| | |
|---|---|
| Sep 2006 | Master of Engineering (Coastal & Maritime) |
| University | Universiti Teknologi Malaysia (UTM) |
| Thesis title | System Performance of A Composite Stepped-Slope |
| | Floating Breakwater |
| | |
| Jul 2002 | Bachelor of Engineering (Civil-Environmental) |
| University | Universiti Teknologi Malaysia (UTM) |
| Thesis title | Field Investigations on the Effectiveness of Malacca |
| | River Rehabilitation |

## Professional Experiences

| | |
|---|---|
| May 2008 - Jul 2009 | Project Engineer & Manager, HR Wallingford Asia Pacific |
| Jul 2007 - Nov 2007 | Lecturer (part-time), College of Science & Technology, UTM |
| May 2007 - Mar 2008 | Coastal Engineer & Research Officer |
| | Coastal & Offshore Engineering Institute (COEI), UTM |
| Oct 2005 - Oct 2006 | Research Officer, COEI, UTM |
| Jan 2005 - Sep 2005 | Research Engineer, COEI, UTM |
| Jun 2002 - Oct 2003 | Research Engineer, COEI, UTM |
| Mar 2002 - May 2002 | Research Trainee, COEI, UTM |

# Publications and presentations

The following is a list of manuscripts, reports and presentations that are related to the present work of this thesis:

1. Lim CH, Lettmann K, Wolff J-O (2013) Numerical study on wave dynamics and wave-induced bed erosion characteristics in Potter Cove, Antarctica. Ocean Dyn 63(11-12):1151-1174, doi: 10.1007/s10236-013-0651-z.

2. Wölfl A-C, Lim CH, Hass HC, Lindhorst S, Tosonotto G, Lettmann K, Kuhn G, Wolff J-O, Abele D (2014) Distribution and characteristics of marine habitats in a subpolar bay based on hydroacoustics and bed shear stress estimations (Potter Cove, King George Island, Antarctica). Manuscript submitted for publication.

3. Monien P, Monien D, Asendorf S, Lettmann K, Lim CH, Schnetger B, Brumsack H-J (2013) Redox conditions and trace metal cycling in coastal sediments from the maritime Antarctic. Manuscript submitted for publication.

4. Brumsack H-J, Monien D, Monien P, Lim CH, Lettmann K, Wolff J-O, Schloss I, Busso AAS, Henkel S, Staubwasser M (2013) Geochemical characterization and fate of the dissolved and particulate load of glacial melt waters of the Potter Cove watershed, King George Island, (western Antarctic Peninsula). In: Abele D (ed) Impact of climate induced glacial melting on marine coastal systems in the Western Antarctic Peninsula region (IMCOAST). Alfred Wegener Institute for Polar and Marine Research (AWI), Bremerhaven, Germany. Unpublished report.

5. Hass HC, Kuhn G, Wölfl A-C, Wittenberg N, Deregibus D, Quartino LM, Tosonotto G, Sahade R, Lindhorst S, Roberts SJ, Braun M, Monien P, Monien D, Lim CH, Strelin J, Fuentes V (2013) The coastal depositional environment in KGI fjord and bay systems. In: Abele D (ed) Impact of climate induced glacial melting on marine coastal systems in the Western Antarctic Peninsula region (IMCOAST). Alfred Wegener Institute for Polar and Marine Research (AWI), Bremerhaven, Germany. Unpublished report.

6. Wölfl A-C, Lim CH, Hass HC, Lettmann K, Kuhn G, Wolff J-O (2013) Detection of factors that control the marine habitat distribution in a periglacial environment (Potter Cove, King George Island, Antarctica). 12th International Symposium on Marine Geological and Biological Habitat Mapping (GeoHab 2013), Rome, Italy,

6-10 May 2013 (oral presentation by Wölfl A-C).

7. Lim CH, Lettmann K, Wolff J-O (2012) Estimating the water mass exchange time scales and sediment erosion characteristics in Potter Cove. IMCOAST Workshop, Alfred-Wegener-Institute for Polar and Marine Research (AWI), Bremerhaven, Germany, 12-14 November 2012 (oral presentation).

8. Lim CH, Lettmann K, Wolff J-O (2012) Numerical modelling of wind waves in Potter Cove, Antarctica. ICBM Seminar, Universität Oldenburg, Germany, 23 July 2012 (oral presentation).

9. Lim CH, Lettmann K, Wolff J-O (2012) Hydrodynamics and bed shear stress in Potter Cove. ICBM Lecture, Universität Oldenburg, Germany, 20 July 2012 (oral presentation).

10. Lim CH, Lettmann K, Wolff J-O (2012) Modelling waves and currents in Potter Cove, Antarctica. 4th IMCOAST Workshop, Palacio San Martin, Buenos Aires, Argentina, 16-20 April 2012 (oral presentation).

11. Lim CH, Lettmann K, Wolff J-O (2011) Tidal dynamics and flow pattern over complex bottom topography in Potter Cove, Antarctica. 10th International Workshop on Multiscale (Un-)structured Mesh Numerical Modelling for Coastal, Shelf and Global Ocean Dynamics (IMUM 2011), Klimahaus, Bremerhaven, Germany, 22-25 August 2011 (poster presentation).

12. Lim CH, Lettmann K, Wolff J-O (2011) Modelling tidal dynamics and flow patterns over complex bottom topography in Potter Cove, Antarctica, using unstructured grid finite volume coastal ocean model. 3rd International Workshop on Modeling the Ocean (IWMO 2011), The First Institute of Oceanography (FIO), Qingdao, China, 6-9 June 2011 (poster presentation).

13. Lim CH, Lettmann K, Wolff J-O (2011) Multi-scale hydrodynamic modelling of Potter Cove, Maxwell Bay, Antarctica, using an unstructured grid finite volume coastal ocean model. 3rd IMCOAST esf-EUROPOLAR Workshop, Alfred-Wegener-Institute for Polar and Marine Research (AWI), Bremerhaven, Germany, 9-13 May 2011 (oral presentation).

# Selbständigkeitserklärung

Hiermit erkläre ich, dass eine Promotion zum Dr. rer. nat. angestrebt wird, dass ich die vorliegende Dissertation selbstständig verfasst und nur die angegebenen Hilfsmittel verwendet habe. Teile der Dissertation sind in einer wissenschaftlichen Fachzeitschrift veröffentlicht worden. Die Dissertation hat weder in Teilen noch in ihrer Gesamtheit einer anderen wissenschaftlichen Hochschule zur Begutachtung in einem Promotionsverfahren vorgelegen. Sie liegt auch zum jetzigen Zeitpunkt weder in Teilen noch in ihrer Gesamtheit einer anderen wissenschaftlichen Hochschule zur Begutachtung in einem Promotionsverfahren vor. Die Leitlinien guter wissenschaftlicher Praxis an der Carl von Ossietzky Universität Oldenburg wurden von mir befolgt. Im Zusammenhang mit dem Promotionsvorhaben sind keine kommerziellen Vermittlungs- oder Beratungsdienste (Promotionsberatung) in Anspruch genommen worden.

Oldenburg, 27.01.2014                                                           Chai Heng Lim